

MULTIPLICITY AND MEAN TRANSVERSE  
MOMENTUM OF PROTON-PROTON  
COLLISIONS AT  $\sqrt{s} = 900$  GeV, 2.76 AND  
7 TeV WITH ALICE AT THE LHC

**A S Palaha**

*Thesis submitted for the degree of  
Doctor of Philosophy*



ALICE Group,  
School of Physics and Astronomy,  
University of Birmingham.

*21<sup>st</sup> August, 2013*

UNIVERSITY OF  
BIRMINGHAM

**University of Birmingham Research Archive**

**e-theses repository**

This unpublished thesis/dissertation is copyright of the author and/or third parties. The intellectual property rights of the author or third parties in respect of this work are as defined by The Copyright Designs and Patents Act 1988 or as modified by any successor legislation.

Any use made of information contained in this thesis/dissertation must be in accordance with that legislation and must be properly acknowledged. Further distribution or reproduction in any format is prohibited without the permission of the copyright holder.

---

# ABSTRACT

The charged particle multiplicity is measured for inelastic and non-single-diffractive proton-proton collisions at collision energies of 900 GeV, 2760 GeV and 7000 GeV. The data analysed corresponds to an integrated luminosity of  $0.152 \pm 0.003 \text{ pb}^{-1}$ ,  $1.29 \pm 0.07 \text{ pb}^{-1}$  and  $2.02 \pm 0.12 \text{ pb}^{-1}$  for each respective collision energy. The average transverse momentum per event as a function of charged multiplicity, for tracks with transverse momentum above 150 MeV/c and 500 MeV/c, is measured for inelastic proton-proton collisions.

Two methods of deconvolution were studied, and an iterative method was used to correct the multiplicity distributions. The effect of pileup on multiplicity measurements was modelled using a toy Monte Carlo.

The results presented extend the previous measurements made by ALICE to more than ten times the average charged multiplicity, and are compared to results from other experiments at similar energies, and to the Monte Carlo generators Phojet and the Perugia-0 tune of Pythia. The pseudorapidity density is estimated from the multiplicity distributions, and found to agree with other experimental results.

The Phojet generator reproduces well the 900 GeV multiplicity distribution, but otherwise it and Pythia both underestimate the probability of higher multiplicities. The Pythia generator reproduces well the average transverse momentum distribution for tracks above 500 MeV/c, and overestimates the lower momentum distribution, while Phojet tends to underestimate the distribution for both momentum thresholds.

Evidence of the violation of KNO scaling is shown for non-single-diffractive events in a pseudorapidity interval of  $\pm 1$ , but not in  $\pm 0.5$ .

---

# AUTHOR'S CONTRIBUTION

The ALICE experiment is a massive collaborative effort from design and running to reconstruction of data and software development, and without the entire collaboration's combined effort, this work would not have been possible. The work presented in this thesis is entirely written by me.

As part of my duties towards the running of the ALICE detector, I was responsible for the Central Trigger Processor (CTP) during shifts in the control room of the experiment, and on-call shifts for which I would provide assistance to the shift leader over the phone or internet. I also contributed to the development of software necessary for CTP monitoring.

I contributed to the development of the track selection algorithm used in the multiplicity analysis of this thesis, and its implementation into the analysis software framework used by all members of the ALICE collaboration.

I was responsible for maintaining the template analysis code for a physics working group, ensuring its availability to the group and consistency with analysis decisions common to the whole working group. This led to my creating a tutorial analysis template for people new to the ALICE analysis software framework, and is contained in the software code. I studied the effect of pileup in proton-proton collisions, and created a simulation that considered the tracking performance and pileup detection of the ALICE detector to predict the contribution of pileup to the data sample. My analysis measures the charged particle multiplicity and the mean transverse momentum per event as a function of charged particle multiplicity. The main body of work for the multiplicity measurement was the study and development of two deconvolution methods for extracting the true distribution from measured data, and developing the error propagation and consistency checks to ensure successful

---

deconvolution. For both the mean momentum and multiplicity analyses, I developed my own analysis framework to produce the measured distributions, efficiencies and corrections used in creating the corrected results. The analysis framework of the collaboration was used by me to run my analysis over the reconstructed data using distributed computing. I created a toy Monte Carlo to estimate the covariance matrices used in the deconvolution methods to test for convergence to a solution.

---

*To my mother Kuldeep, my sister Gurpreet, and in memory of my father Amarjit*

---

# ACKNOWLEDGEMENTS

I thank my supervisors David Evans and Lee Barnby, who guided me and worked with me throughout my PhD. They were invaluable to me as sources of encouragement and advice, along with the rest of the Birmingham group; Orlando Villalobos-Baillie, Roman Lietava, Peter Jones, Cristina Lazzeroni, Anju Bhasin, Gron Tudor Jones, Frank Votruba, Marek Bombara, Daniel Tapia Takaki, Anton Jusko and Marian Krivda. The evenings we spent at the ALICE flat were particularly fun!

I am grateful to David Evans, Paul Newman and Peter Watkins for offering me the PhD position, and to the STFC and the University of Birmingham for funding me, and the UK Liaison Office for helping me move to and from my stay at CERN. I would also like to thank the Birmingham Particle and Nuclear Physics groups for being a friendly and welcoming environment to work.

I offer particular gratitude to Plamen Petrov, with whom I shared the whole PhD experience, and had many fantastic discussions with. It would not have been the same without you, buddy.

I'm glad I got to share an office with Patrick Scott, Sparsh Navin, Zoe Matthews, Ravjeet Kour, Angela Romano, Graham Lee, Luke Hanratty and Didier Alexandre; I really enjoyed our times together. To the people I met at CERN, I thank Lucy Renshall-Randles for helping me settle at CERN, Deepa Thomas for our interesting conversations, and everyone I worked with on shift at the control room and in the working groups. And to Mark Stockton, Jody Palmer, and the rest of the skiing LTA students, our times shredding the slopes was brilliant!

To my friends closer to home who helped me relax, I thank Chandni Ladva, Rich Powis, Phil "Wrexy" Brown, Lyn Rycroft and Hardeep Bansil, and all my friends from Leamington, you guys are awesome.

---

Finally, I wish to thank my family, my mum Kuldeep who looked after me, my sister Gurpreet who encouraged and inspired me, and my dad Amarjit who believed in me all my life.

---

# CONTENTS

<b>1</b>	<b>Theory</b>	<b>1</b>
1.1	Introduction . . . . .	1
1.1.1	Standard Model . . . . .	2
1.2	Quantum ChromoDynamics . . . . .	5
1.2.1	The Quark Model . . . . .	5
1.2.2	Colour and SU(3) symmetry . . . . .	6
1.2.3	Confinement . . . . .	7
1.2.4	Asymptotic Freedom . . . . .	8
1.3	Quark-Gluon-Plasma . . . . .	10
1.3.1	De-confinement . . . . .	10
1.3.2	Properties . . . . .	11
1.4	Kinematic Variables . . . . .	16
1.5	Proton-Proton Collisions . . . . .	19
1.5.1	Event Classification . . . . .	19
1.5.2	Pomeron exchange . . . . .	21

---

1.5.3	Simulating Proton-Proton Collisions . . . . .	23
1.6	Koba-Nielsen-Oleson scaling . . . . .	25
1.7	Negative Binomial Distribution . . . . .	27
1.7.1	Interpretation of Multiplicity Distributions . . . . .	29
1.8	Previous Experimental Results . . . . .	33
1.8.1	Charged Particle Multiplicity . . . . .	33
1.8.2	Mean Transverse Momentum . . . . .	41
1.9	Summary . . . . .	47
<b>2</b>	<b>The ALICE experiment at the LHC</b>	<b>48</b>
2.1	The LHC . . . . .	48
2.2	The ALICE detector . . . . .	51
2.2.1	Inner Tracking System . . . . .	55
2.2.2	Time Projection Chamber (TPC) . . . . .	58
2.2.3	Transition Radiation Detector (TRD) . . . . .	61
2.2.4	Time of Flight (TOF) Detector . . . . .	62
2.2.5	Electromagnetic Calorimeter (EMCal) . . . . .	63
2.2.6	High Momentum Particle Identification Detector (HMPID) . . . . .	64
2.2.7	Photon Spectrometer (PHOS) . . . . .	64
2.2.8	Muon Spectrometer . . . . .	65
2.2.9	Zero Degree Calorimeters (ZDC) . . . . .	66
2.2.10	Photon Multiplicity Detector (PMD) . . . . .	66
2.2.11	Forward Multiplicity Detector (FMD) . . . . .	67
2.2.12	V0 . . . . .	67
2.2.13	T0 . . . . .	68

---

2.2.14	ALICE COsmic Ray DEtector (ACORDE) . . . . .	68
2.3	Central Trigger Processor (CTP) . . . . .	69
2.4	Data AQuisition (DAQ) . . . . .	72
2.5	High Level Trigger (HLT) . . . . .	73
2.6	Detector Summary . . . . .	73
<b>3</b>	<b>Multiplicity and Mean <math>p_T</math></b> . . . . .	<b>75</b>
3.1	Event Selection . . . . .	76
3.1.1	Trigger Selection . . . . .	76
3.1.2	Vertex Selection . . . . .	78
3.2	Primary Track Selection . . . . .	84
3.3	Pileup . . . . .	88
3.3.1	Average Number of Interactions, $\mu$ . . . . .	90
3.3.2	Pileup Simulation . . . . .	91
3.3.3	Discoverable Pileup . . . . .	94
3.4	Multiplicity Counting . . . . .	97
3.5	Unfolding the Multiplicity Distribution . . . . .	101
3.5.1	Naive Solution . . . . .	102
3.5.2	Single Value Decomposition Unfolding . . . . .	106
3.5.3	Unfolding Based on Bayes Theorem . . . . .	113
3.6	Mean $p_T$ as a Function of Multiplicity . . . . .	125
3.7	Systematic Uncertainties . . . . .	137
3.7.1	Charged Particle Multiplicity . . . . .	137
3.7.2	Mean $p_T$ as a function of Charged Particle Multiplicity . . . . .	140
3.7.3	Summary . . . . .	141

<b>4</b>	<b>Results</b>	<b>143</b>
4.1	Charged Particle Multiplicity . . . . .	144
4.2	Pseudorapidity Density Approximation . . . . .	154
4.3	KNO scaling . . . . .	157
4.4	Mean $p_T$ as a function of Charged Multiplicity . . . . .	160
4.5	Summary . . . . .	165
<b>5</b>	<b>Conclusion</b>	<b>166</b>

---

# LIST OF FIGURES

1.1	Simplest QED and QCD couplings . . . . .	7
1.2	Virtual particle loops in QED and QCD . . . . .	9
1.3	Phase Diagram of Nuclear Matter . . . . .	12
1.4	Rapidity Distribution of Diffractive Processes . . . . .	20
1.5	Chew-Frautschi plot . . . . .	22
1.6	Examples of Negative Binomial Distributions . . . . .	28
1.7	KNO scaling at ISR energies . . . . .	34
1.8	UA5 Multiplicity distribution of NSD pp collisions at $\sqrt{s} = 200, 546$ and 900 GeV . . . . .	35
1.9	UA5 NSD Multiplicity at $\sqrt{s} = 900$ GeV with fit to sum of 2 NBDs .	36
1.10	Violation of KNO scaling with increasing collision energy . . . . .	37
1.11	CDF Multiplicity in KNO variables for soft and hard events at $\sqrt{s} =$ 600, 1800 GeV . . . . .	38
1.12	ALICE and CMS published multiplicity distributions . . . . .	39
1.13	CMS Multiplicity in KNO variables for $ \eta  < 0.5$ and $ \eta  < 2.4$ . . . .	40

1.14	Pseudorapidity density for proton-proton collisions as a function of collision energy . . . . .	41
1.15	ALICE published mean $p_T$ versus $N_{CH}$ at $\sqrt{s} = 900$ GeV with comparisons . . . . .	42
1.16	CDF mean $p_T$ versus $N_{CH}$ at $\sqrt{s} = 630$ and 1800 GeV, for minimum bias, soft and hard events. . . . .	44
1.17	ALICE mean $p_T$ versus $N_{CH}$ for soft and hard events at $\sqrt{s} = 900$ and 7000 GeV . . . . .	45
1.18	Mean $p_T$ versus collision energy from various experiments . . . . .	46
2.1	Schematic layout of the LHC . . . . .	49
2.2	The LHC hadron injector complex . . . . .	50
2.3	The ALICE detector . . . . .	53
2.4	The Pseudorapidity coverage of the ALICE detectors . . . . .	54
2.5	Schematic layout of the six layers of the ITS . . . . .	55
2.6	Diagram of the TPC field cage . . . . .	59
2.7	Track finding efficiency for just the TPC, and the TPC and ITS combined . . . . .	61
2.8	Monitoring tool for CTP trigger rates . . . . .	72
3.1	Acceptance of global tracks . . . . .	81
3.2	Acceptance of SPD tracklets . . . . .	82
3.3	Combined triggering and vertexing efficiencies for $ \eta  < 1.0$ inelastic and NSD events . . . . .	84
3.4	Perpendicular distance of closest approach of tracks with SPD hits to vertex . . . . .	86
3.5	Perpendicular distance of closest approach of tracks without SPD hits to vertex . . . . .	87
3.6	Perpendicular distance of closest approach of tracks with and without SPD hits . . . . .	88

---

3.7	Secondary contamination of accepted tracks as a function of $p_T$ . . . . .	89
3.8	$z$ -dca to primary vertex of primary and secondary tracks . . . . .	92
3.9	Relative abundance of multiple-interaction multiplicity distributions for a given interaction probability . . . . .	93
3.10	Fraction of pileup events with vertex separation in $z$ less than $\Delta z$ as a function of $\Delta z$ . . . . .	95
3.11	Fraction of pileup per multiplicity bin, from pileup simulation of 7 TeV data, before and after removal of tagged pileup events. . . . .	96
3.12	Effect of pileup removal on multiplicity distributions . . . . .	97
3.13	Correlation of Multiplicity Counting Methods with True Multiplicity	101
3.14	The spread of measured multiplicities for a true multiplicity of 20 . . .	102
3.15	Response Matrices with Physical and Flat Multiplicity Distributions .	103
3.16	Unfolding using the inverse of the response matrix . . . . .	104
3.17	Removal of isolated multiplicity bins . . . . .	106
3.18	Distribution of the SVD rotated measured vector, to choose regular- isation parameter . . . . .	110
3.19	SVD unfolding with Minimum Bias response . . . . .	111
3.20	SVD unfolding with Flat Multiplicity response . . . . .	112
3.21	Two steps of Bayesian Iterative Unfolding . . . . .	116
3.22	Many steps of Bayesian Iterative Unfolding . . . . .	117
3.23	Alternative stopping criteria for iterative unfolding . . . . .	122
3.24	Model Dependence of Bayesian Unfolding with Minimum Bias Response	124
3.25	Model Dependence of Bayesian Unfolding with Flat Multiplicity Re- sponse . . . . .	126
3.26	ITSTPC track transverse momentum resolution . . . . .	128
3.27	ITS complimentary track transverse momentum resolution . . . . .	129

3.28	ITSTPC tracking efficiency as a function of $p_T$ . . . . .	131
3.29	Mean $p_T$ versus multiplicity using 900 GeV Pythia data . . . . .	133
3.30	Mean $p_T$ versus multiplicity using 2760 GeV Phojet data . . . . .	134
3.31	Mean $p_T$ versus multiplicity using 7000 GeV Pythia data . . . . .	135
3.32	ITSTPC and ITS complimentary tracking efficiency as a function of $p_T$	137
4.1	Example of unfolded multiplicity distribution of inelastic events with $\sqrt{s} = 7000$ GeV . . . . .	145
4.2	Multiplicity of NSD events within $ \eta  < 0.5$ . . . . .	146
4.3	Multiplicity of NSD events within $ \eta  < 1.0$ . . . . .	147
4.4	Multiplicity of inelastic events within $ \eta  < 0.5$ . . . . .	148
4.5	Multiplicity of inelastic events within $ \eta  < 1.0$ . . . . .	149
4.6	Comparison of NSD multiplicity distribution in $ \eta  < 0.5$ at $\sqrt{s} =$ 900 GeV to other experimental results and generators . . . . .	150
4.7	Comparison of NSD multiplicity distribution in $ \eta  < 1.0$ at $\sqrt{s} =$ 2760 GeV to other experimental results and generators . . . . .	151
4.8	Comparison of inelastic multiplicity distribution in $ \eta  < 1.0$ at $\sqrt{s} =$ 7000 GeV to other experimental results and generators . . . . .	152
4.9	Comparison of NSD multiplicity distribution in $ \eta  < 1.0$ at $\sqrt{s} =$ 7000 GeV to other experimental results and generators . . . . .	153
4.10	Multiplicity of inelastic events in $ \eta  < 0.5$ for tracks above a $p_T$ threshold, compared to generators . . . . .	154
4.11	Multiplicity of inelastic events in $ \eta  < 1.0$ for tracks above a $p_T$ threshold, compared to generators . . . . .	155
4.12	Multiplicity distributions of NSD events plotted in KNO variables . .	157
4.13	$C_q$ moments of NSD multiplicity distributions as a function of collision energy . . . . .	158
4.14	Mean $p_T$ as a function of multiplicity measured at $\sqrt{s} = 900, 2760$ and 7000 GeV . . . . .	161

4.15	Mean $p_T$ as a function of multiplicity at $\sqrt{s} = 900$ GeV compared to previous experimental results and generators . . . . .	163
4.16	Mean $p_T$ as a function of multiplicity at $\sqrt{s} = 2760$ GeV compared to generators . . . . .	163
4.17	Mean $p_T$ as a function of multiplicity at $\sqrt{s} = 7000$ GeV compared to generators . . . . .	164

---

# LIST OF TABLES

1.1	Standard Model fermions . . . . .	3
3.1	Trigger efficiencies in percent for the MBOR and MBAND triggers in selecting events with given processes . . . . .	79
3.2	Diffractive fractions and inelastic cross sections . . . . .	80
3.3	Vertex selection according to pseudorapidity interval . . . . .	83
3.4	Track quality criteria . . . . .	99
3.5	Summary of systematic uncertainties . . . . .	142
4.1	Pseudorapidity density of charged particles in $ \eta  < 0.5$ . . . . .	156
4.2	$C_q$ moments of measured NSD multiplicity distributions for $ \eta  < 0.5$	159
4.3	$C_q$ moments of measured NSD multiplicity distributions for $ \eta  < 1.0$	159

---

---

# CHAPTER 1

---

## THEORY

### 1.1 Introduction

This chapter provides an introduction to the theory of interactions between subatomic particles, focusing on strongly interacting matter and the implications for it at high energy densities probed by nucleus-nucleus collisions, where strongly bound matter becomes deconfined. The framework of describing particle collisions is briefly outlined, defining useful variables used throughout this work. The importance of studying proton-proton collisions, in reference to heavy-ion collisions and on its own

merits, particularly with the low-momentum capabilities of ALICE, are considered, focusing on the measurements of charged particle multiplicity and average transverse momentum as a function of multiplicity. The modelling of proton-proton collisions is outlined, looking at the theory of parton-parton interactions and the description of diffraction. The charged particle multiplicity of proton-proton collisions is discussed, and an introduction to models describing and interpreting the observed results are given. Finally, results from previous collider experiments of multiplicity and average transverse momentum are given.

### 1.1.1 Standard Model

The constituents of matter and the carriers of the forces, through which matter interacts, are fundamental particles. The interactions of the strong, weak and electromagnetic forces, and the constituents of matter are described by the gauge theories of the Standard Model (SM) [1].

#### **Fermions**

Fermions are particles with intrinsic spin (angular momentum) of half-integer values, so they obey the Pauli-Exclusion Principle, and each particle has an anti-particle with opposite charge but the same mass.

Leptons are a sub-group of this particle type, an example from ordinary matter is

the negatively charged electron. Heavier “flavours” of the electron also exist, the muon,  $\mu$  and tau-lepton,  $\tau$  in order of increasing mass. Each type of electron has an associated neutrino, an electrically neutral particle of almost zero mass.

Quarks make up the other sub-group of fermions. They come in six flavours, have fractional electric charge, and carry “colour” charge which defines their coupling to the strong force. They each have baryon number  $\frac{1}{3}$  (anti-quarks have baryon number  $-\frac{1}{3}$ ) and combine in threes to form baryons, or quark and anti-quark pairs to form mesons; both combinations have zero net colour charge.

The fermions may be grouped into three generations, as shown in Table 1.1. The first generation particles are the most stable and make up most of the observed matter in the Universe. The higher, and heavier, generations are unstable and decay to lower generation particles via weak interactions.

*Table 1.1: Standard Model fermions*

Generation	I	II	III
Quarks	up	charm	top
	down	strange	bottom
Leptons	$e$	$\mu$	$\tau$
	$\nu_e$	$\nu_\mu$	$\nu_\tau$

## Bosons

The interactions between all these particles are mediated by bosons, having integer values of spin. Electromagnetism is mediated by the electrically neutral photon, described by the theory of Quantum Electro-Dynamics (QED). The Strong force is mediated by massless gluons. Unlike the photon which has no electric charge, gluons themselves have a colour charge, and can self-interact. The theory of colour interactions is called Quantum Chromo-Dynamics (QCD), and is discussed in more detail in the next section.

The Weak force has three bosons, two electrically charged ( $W^\pm$ ) and one neutral ( $Z^0$ ), which allow fermions to change flavour and, contrary to the theory of gauge bosons, also have mass (thus limiting the range of the Weak force) [2]. This discrepancy is alleviated with the inclusion of the Higgs boson [3, 4, 5], allowing particles to acquire mass by coupling to a Higgs field, crucially giving  $W^\pm$  and  $Z^0$  mass but leaving the  $\gamma$  massless, as seen experimentally. The acquisition of their particular masses by the weak bosons is an example of spontaneous symmetry breaking, allowing the weak and electromagnetic bosons to exist as distinct particles with their observed masses (or lack thereof) while at higher energies they combine to form the bosons of the Electro-Weak force. Evidence of the Higgs boson is reported in [6, 7].

## 1.2 Quantum ChromoDynamics

### 1.2.1 The Quark Model

Quarks are the partons, which form hadrons, proposed by Gell-Mann [8] and Zweig [9] around 1964 to account for the properties of the many new hadrons observed at that time. Many of the new particles, such as the kaon, exhibited longer decay times than other mesons; they were produced via the strong force but were seen to decay weakly. These ‘strange’ new particles were assigned a strangeness quantum number conserved by strong interactions, but not by weak. Strangeness, along with electric charge and isospin value  $I_3$ <sup>1</sup>, were used to catalogue baryons and mesons of similar mass into patterns called ‘multiplets’. It was first applied to the lightest mesons and baryons to make octets, and so was called the ‘Eightfold Way’ [1], extended to groups of larger mass baryons to make other patterns, such as the baryon decuplet.

This approach led to the prediction of new states, yet to be discovered at the time, including the triply strange  $\Omega^-$  baryon, leading to the quark model of hadrons. The baryons were known to be fermions, being made of three spin-half partons, thus requiring an overall anti-symmetric wave-function in order to obey Pauli’s Exclusion Principle. This was seen to be violated by certain combinations of 3 identical

---

<sup>1</sup>Isospin is a quantum number motivated by the symmetry seen between the proton and neutron in relation to their difference in mass and their strong interactions. They both have isospin value  $\frac{1}{2}$ , the proton with an isospin projection  $I_3$  of  $+\frac{1}{2}$  and neutron of  $-\frac{1}{2}$ . The value  $I_3$  is now understood as the up and down quark content of a partonic state.

quarks, a problem that is removed with the introduction of the colour charge to the quarks [10].

### 1.2.2 Colour and SU(3) symmetry

Colour charge is a property held by strongly interacting particles, initially proposed to explain the existence of baryons with valence quarks in seemingly identical quantum states. Unlike the electric charge of QED which has one value and one anti-value (it can be positive or negative), a quark's colour charge has a value of either red, green or blue, with the anti-quarks carrying colour charge of anti-colour. The requirement of the quarks to be in different quantum states showed that all observed baryons are colourless, they contain equal amounts of all three values of colour charge. This is known as a colour 'singlet' state, and is the colour state of mesons as well, where the quark has the opposite colour of the anti-quark.

Colour generates an exact SU(3) symmetry [2], and is completely conserved in strong interactions. As baryons are colourless, they must be in a colour singlet state which is an anti-symmetric state, requiring the other contributions to its wave-function to be completely symmetric (fermions must have an anti-symmetric wave-function). This is confirmed in the multiplets of observed baryons.

The mediator of the strong force is the gluon, a colour-charged massless boson which can take one of eight colour states, but not the singlet colour state. Thus the gluon

acts on quarks with colour charge, not a colourless hadron as a whole. The strong interaction between hadrons can be understood as an exchange of colourless mesons over a short range (less than a hadron's radius).

The gluon mediated interaction of quarks is the QCD equivalent to the QED coupling of two fermions and a photon, as shown in Figure 1.1. Gluons can couple also to other gluons, allowing more complex QCD processes to occur.

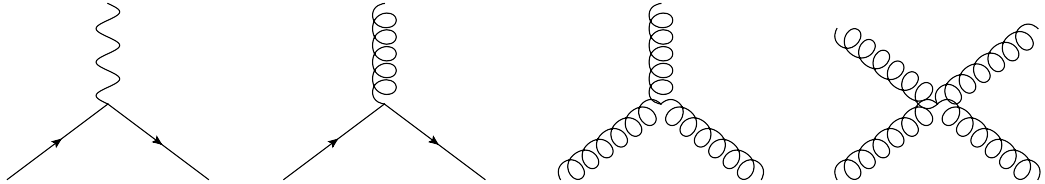


*Figure 1.1: (1st) The QED coupling of a charged fermion to a photon. (2nd) The QCD coupling of a quark to a gluon. (3rd) The QCD coupling of three gluons. (4th) The QCD coupling of four gluons.*

### 1.2.3 Confinement

A property of coloured particles is that of confinement; no free colour charged particle is observed, it is always in a colourless bound state. This is illustrated by the gluons carrying colour charge, and thus never appearing as free themselves. As the strong force is observed only over short distances, typically  $\sim 1$  fm, it means that a free colour singlet gluon cannot exist, otherwise the range of the strong force would be infinite (like electromagnetism).

Another understanding of confinement is through the QCD potential ( $V_s$ ) which,

like that of QED, follows an inverse proportionality to the range, however it also includes a linear term;

$$V_s = -\frac{4}{3} \frac{\alpha_s}{r} + kr , \quad (1.1)$$

where  $\alpha_s$  is the strong coupling ‘constant’ which is small at small distances and large for large distances,  $r$  is the distance and  $k$  is an energy density calculated to be  $0.85 \text{ GeV fm}^{-1}$  [2]. As the distance between two coloured particles increases, the exchange of gluons between them form a gluon field that is stretched into a tube. Like the electric field lines between two charged particles, the colour force between quarks can be represented as field lines, but the gluon self interaction pulls the colour lines together, constricting the force lines into a tube. The attractive linear term of the potential dominates, and as the quarks separate, the energy stored in the potential becomes high enough that a quark-anti-quark pair is created, an energetically favourable situation over two free quarks. Thus, quarks are always found in a colour neutral bound state.

#### 1.2.4 Asymptotic Freedom

The strong coupling ‘constant’  $\alpha_s$  in equation 1.1 is actually a running coupling; it is not constant at all. This is due to vacuum polarisation; virtual particles of colour charge around the quark are polarised such that from a certain distance the charge is partially cancelled out. This is represented in Feynman diagrams as loops of virtual particles in the propagator, as shown in Figure 1.2.

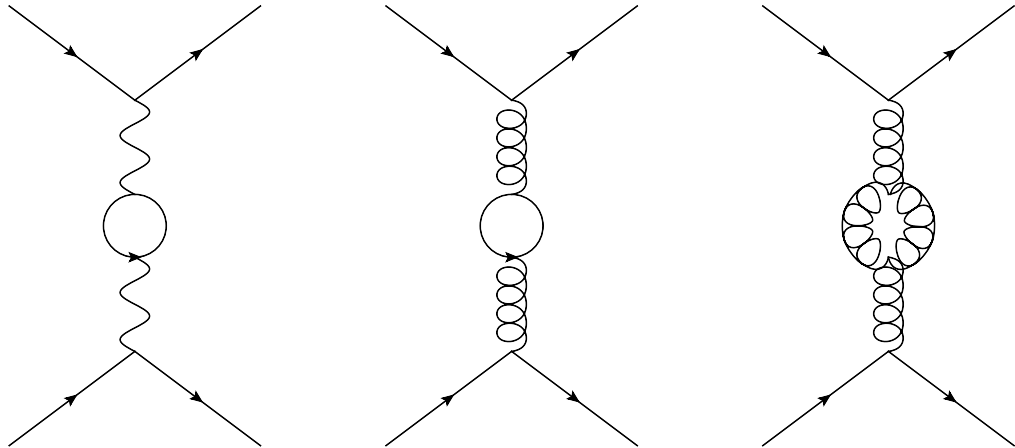


Figure 1.2: Loop diagrams showing vacuum polarisation with a fermion loop for a simple QED interaction (left) and QCD (middle), and with a gluon loop for QCD (right). Note that these represent the simplest vacuum polarisation loops, there are higher order contributions from multiple loops in the propagator to increasingly complex loop structures.

QED has the same phenomenon with virtual leptons leading to charge screening, but for QCD the gluon contribution must be taken into account. As the gluon itself carries a colour and anti-colour charge, and can interact with other gluons, a gluon can give rise to another pair of gluons, with polarisation such that the colour field of the quark is enhanced; the colour charge is anti-screened. Thus, there are two competing screenings; one from quark-anti-quark loops which screen the colour charge, and another from gluon loops which enhance it.

The running coupling of the strong force for a momentum transfer of  $|q^2|$  can be expressed as:

$$\alpha_s(|q^2|) = \frac{\alpha_s(\mu^2)}{1 + \frac{1}{12\pi}(11c - 2f)\alpha_s(\mu^2) \ln\left(\frac{q^2}{\mu^2}\right)} \quad (1.2)$$

where  $\mu^2$  is a momentum transfer for which the strong coupling is known,  $c$  is the

number of colours (3), and  $f$  is the number of quark flavours (6) [1]. The energy scale  $\Lambda_{QCD}$  above which perturbative QCD is applicable is represented to leading order in equation 1.3, and is approximately 200 MeV;

$$\ln \Lambda_{QCD}^2 = \ln \mu^2 - \frac{12\pi}{(11c - 2f)\alpha_s(\mu^2)}. \quad (1.3)$$

This calculation is only valid while the coupling is considerably less than 1, as it relies on perturbation theory. For low momentum transfer interactions, where  $|q^2| \sim \Lambda_{QCD}^2$ , the strong coupling blows up in this formalism as  $\alpha_s \sim 1$ , and perturbation theory can no longer be applied. For  $q^2 \gg \Lambda_{QCD}^2$ , the coupling constant weakens significantly, as the anti-screening effect of virtual gluons dominates over the screening from virtual quarks. This effect is represented in the term comparing the number of colours and quark flavours in the denominator of the strong coupling. It is in this regime that perturbative calculations may be applied to QCD processes such as interaction cross-sections.

## 1.3 Quark-Gluon-Plasma

### 1.3.1 De-confinement

Quarks are not found free in nature, they are confined in groups called hadrons. The theory of QCD predicts that above some critical energy density, the system of quarks and the gluons that hold them together undergo a phase transition which

allows them to move freely. This state of de-confinement is known as a Quark-Gluon-Plasma (QGP) [11], in which there are free colour-charged partons.

The Universe is thought to have existed in this state for the first few microseconds after the Big Bang, its expansion and cooling allowing hadrons to form. The conditions required to form a QGP can be created at particle colliders with heavy-ion collisions.

### 1.3.2 Properties

Calculations using the Lattice QCD framework [12] yield equilibrium properties of the QGP. It uses a discrete model of space-time as a lattice to model QCD interactions that introduces a momentum cut-off related to the lattice spacing. This removes divergences encountered in perturbative QCD due to large coupling strengths, and thus allows calculations of both confinement and the de-confined state.

By extrapolating the lattice spacing towards zero, the continuum is reproduced. Lattice QCD predicts that a critical temperature  $T_c \sim 170$  MeV is required for quarks to become de-confined, and also a critical energy density  $\varepsilon_{cr} \sim 1$  GeV/fm<sup>3</sup> [13]. This assumes a zero baryon chemical potential  $\mu_B$ , understood as zero net baryon number (the number of baryons and anti-baryons is equal) per unit volume, for which increasing temperature results in a rapid change to a QGP. The limitation of lattice QCD calculations is that it is only calculable for zero (or very small) net

baryon chemical potential. Calculations for non-zero  $\mu_B$  indicate a first order phase transition to QGP at the critical energy density  $\varepsilon_{cr}$ . The phase diagram of nuclear matter is shown in Figure 1.3 as a function of temperature and baryon chemical potential.

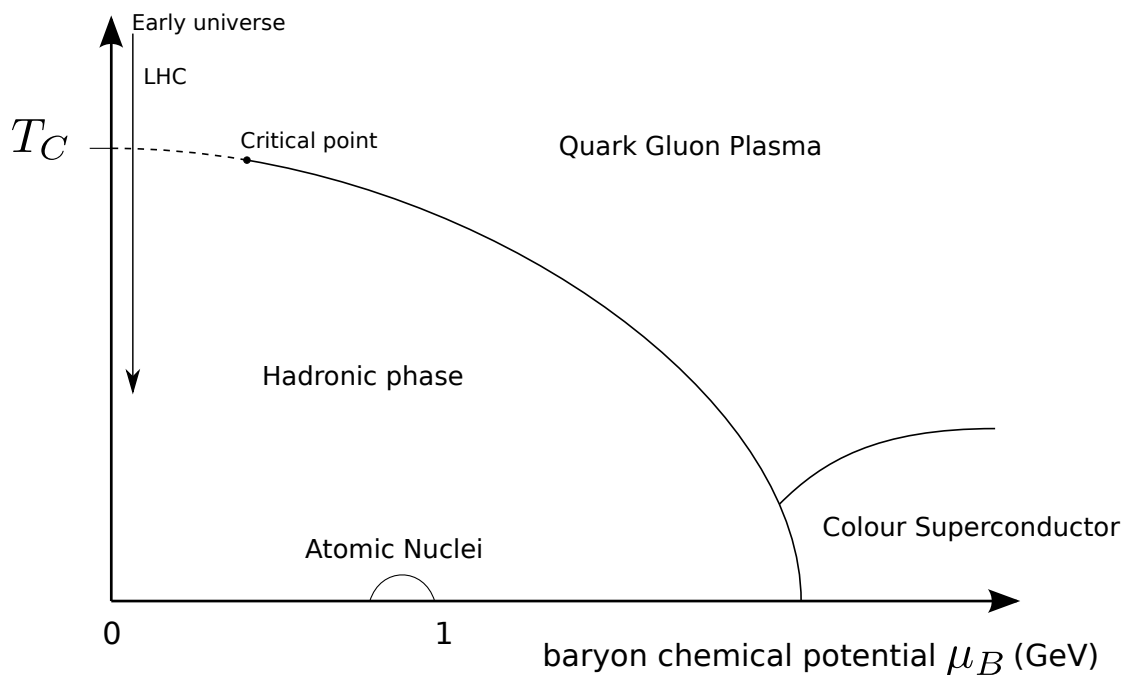


Figure 1.3: Phase diagram of nuclear matter. Cold nuclear matter such as nuclei exist at baryon chemical potential of  $\sim 1$  GeV. Heating matter causes excitations as hadron resonances to appear, before crossing into de-confinement. Above some value of baryon chemical potential, the change to a QGP is a first order phase transition at a critical energy density.

With increasing collision energy, hadrons become more transparent to each other, and systems produced from parton collisions have fewer remnants of the colliding hadrons; thus the baryon chemical potential decreases, approaching the condition of the early Universe.

Methods using the MIT Bag Model with statistical techniques find a similar critical temperature requirement for de-confinement [14].

A consequence of de-confinement is the shedding of the quarks' mass to leave the bare quark mass. The constituent mass of a quark is generated by the binding of the quarks into hadrons, which accounts for 99% of the mass of normal matter [15].

In relativistic heavy ion collisions, the colliding nuclei (modelled as flat discs due to relativistic length contraction) meet and pass mostly through each other, leaving behind scattered remnants. Before these have time to re-scatter and thermalise, hard parton-parton interactions produce high momenta particles in the early stages of the collision, which are not released into a free vacuum as in proton-proton collisions, but immediately interact with the nuclei remnants from the collision. This re-scattering can form the dense, strongly-interacting matter which can, with a high enough energy density and rapid enough thermalisation (within 1 fm/c of the collision), form a QGP.

This 'fireball' of de-confined coloured partons produces many new particles through their elastic and inelastic interactions, which leads to the equipartition of the deposited energy of the collision. Only the inelastic collisions change the chemistry of the system, that is the abundances of the different types of partons (gluons, light and heavy quarks).

The rapidly thermalised system has an internal pressure against the surrounding vacuum, and expands and cools. The expansion happens over a time scale of the

order of 15 fm/c after the collision. When the energy density drops below the critical requirement for QGP, the partons hadronise into confined states of hadrons. The temperature of the system drops below the chemical freeze out temperature  $T_{\text{ch}}$ , so that inelastic collisions no longer contribute to the changing of the chemical composition of the system, and the relative abundances of the types of particles are frozen out. Elastic collisions still occur for a time, keeping the system in thermal equilibrium until the temperature drops below the kinetic freeze out temperature  $T_{\text{k}}$ , where the particles decouple from each other completely with no more re-scattering, and the distribution of the particles' momenta reflects the temperature of the system at this point.

The QGP state is known to be a dense, strongly interacting medium as it reduces the energy of fast partons that would go on to produce jets; this is known as jet-quenching [16]. It also exhibits an increase in strange quark production compared to lower energy heavy-ion collisions that do not produce a QGP, as the energy threshold is reduced by the shedding of some of the quark's mass [17].

Much of the understanding of heavy-ion collisions, and the QGP in particular, requires comparison to proton-proton collisions in which there is no large volume of dense coloured matter. Thus it is a vital part of a heavy-ion physics programme to study and understand proton-proton interactions, in order to provide an experimental control where a QGP is not expected to form, and thus highlight the aspects of heavy-ion collisions that are due to the QGP. There also aspects of proton-proton

physics that are more accessible to ALICE than other LHC experiments, such as low momentum tracking and particle identification.

It has been suggested, however, that proton-proton collisions at LHC energies may produce a QGP state in very high multiplicity events [18]. For nucleus-nucleus collisions, the initial energy density of the system was shown by Bjorken [19] to be:

$$\varepsilon = \frac{1}{\tau A} \frac{dE_T}{dy}, \quad (1.4)$$

where  $A$  is the cross-sectional area of the colliding nuclei, and  $\tau$  is the time for a QGP to form which, though still under debate, is taken as roughly less than or approximately equal to 1 fm/c.

The average transverse energy  $\frac{dE_T}{dy}$  carried by particles produced roughly at central rapidity is related to the multiplicity at central rapidity and mean transverse momentum  $\overline{p_T}$  by:

$$\frac{dE_T}{dy} \simeq \frac{dN_{CH}}{dy} \overline{p_T}. \quad (1.5)$$

At RHIC, colliding gold nuclei at  $\sqrt{s_{NN}} = 200$  GeV has given an initial energy density above 5 GeV/fm<sup>3</sup> [20], and lead nuclei collisions at  $\sqrt{s_{NN}} = 2760$  GeV at the LHC reach a factor of 3 higher [21, 22]. With an average charged particle multiplicity density of  $6.01 \pm 0.01_{-0.12}^{+0.20}$  for  $\sqrt{s} = 7000$  GeV proton collisions [23], achieving an energy density of  $\sim 1$  GeV/fm<sup>3</sup> using equation 1.4, high multiplicity events should certainly be able to exceed the critical energy density for a QGP.

## 1.4 Kinematic Variables

Here it is useful to define some commonly used variables to describe the kinematics, or motions of particles, in particle collisions, as they will be used throughout this work.

The energy and momentum of a particle can be expressed as a four component vector, called ‘four-momentum’, and in a system of natural units ( $\hbar = c = 1$ ) is expressed as

$$P = (E, \vec{p}) = (E, p_x, p_y, p_z) . \quad (1.6)$$

The four-momentum is particularly useful as it is a conserved quantity, its behaviour is understood under Lorentz transforms, and it also provides the Lorentz invariant mass of the particle.

From this, Lorentz invariant Mandelstam variables [1] may be constructed that describe a collision of 2 particles with four-momenta  $P_1$  and  $P_2$  resulting in a final state of 2 particles with four-momenta  $P_3$  and  $P_4$ ;

$$\begin{aligned} s &= (P_1 + P_2)^2 = (P_3 + P_4)^2 , \\ t &= (P_1 - P_3)^2 = (P_2 - P_4)^2 , \\ u &= (P_1 - P_4)^2 = (P_2 - P_3)^2 . \end{aligned} \quad (1.7)$$

The variables are used to represent different types of scattering events; the  $s$ -channel involves the conversion of the incident particles to an intermediate particle before splitting into two particles, and also represents the collision energy between two particles. The  $u$ - and  $t$ -channels represent the exchange of an intermediate particle. In all three cases, the variable represents the squared four-momentum transferred by the intermediate particle.

Although the vast majority of the collisions studied by the LHC experiments are inelastic with more than 2 final state particles, the  $s$  variable is used to quantify the collision energy between the two colliding beam bunches in the centre of mass frame;  $\sqrt{s}$ . For collisions between nuclei, with multiple nucleons, the collision energy is defined per nucleon, denoted  $\sqrt{s_{NN}}$ .

From the components of momentum defined in Cartesian coordinates, as in equation 1.6, the transverse momentum is defined as the momentum of a particle perpendicular to the colliding beam direction:

$$p_T = \sqrt{p_x^2 + p_y^2}. \quad (1.8)$$

In a collision between hadrons, at relativistic energies, the proton interacts not as a single object, but as a dense collection of partons, from the valence quarks to the gluons, quarks and anti-quarks (referred to as ‘sea quarks’), each carrying some fraction of the proton’s momentum. It is impossible to know exactly the interacting parton’s momentum as a fraction of the proton’s, and so the collision products may

be given a longitudinal boost, effectively given extra momentum in one direction from the beam momentum. The transverse momenta of the collision products is unaffected by longitudinal boosts, and results from the fraction of energy lost by the colliding particles.

Rapidity is a kinematic variable which describes, in the limit of a particle's mass being far less than its total energy, the particle's angle with respect to the beam axis using its energy and longitudinal momentum;

$$y = \frac{1}{2} \ln \frac{E + p_z}{E - p_z} . \quad (1.9)$$

The difference in rapidity between two particles is invariant under longitudinal Lorentz boosts [24]. For unidentified particles whose mass is not known (essential in calculating the total energy) a preferred measure called 'pseudo-rapidity' is used. It is based only on the polar angle between the particle and beam trajectories which can be measured directly by the detector,  $\theta$ ;

$$\eta = -\ln\left(\tan \frac{\theta}{2}\right) , \quad (1.10)$$

and in the limit of the particle mass  $m \rightarrow 0$ , the pseudo-rapidity is equivalent to the rapidity.

## 1.5 Proton-Proton Collisions

This section describes the modelling and theory of interactions between protons at relativistic energies.

### 1.5.1 Event Classification

Collisions between hadrons are commonly classified according to the diffractive nature of the interaction. Naturally, this only applies to inelastic collisions where the incoming hadrons break up. Diffraction in high energy collisions occurs when an incident particle enters an excited state, and dissociates into a system of partons which carry the net quantum numbers of the excited particle. This diffractive system then goes on to hadronise into final state particles.

A single(double)-diffractive event has one(both) of the incident particles dissociating. A non-diffractive event describes inelastic collisions with a parton-parton interaction exchanging colour charge with a large momentum transfer (more than a few GeV/c). The resulting spatial distribution of the final state particles is heavily influenced by the diffractive nature of the collision, as shown in Figure 1.4.

In a single-diffractive (SD) event, the intact proton continues at beam rapidity, the other dissociates into particles found at forward rapidities. Double-diffractive (DD) events result in particles found at large positive and negative rapidities. Non-diffractive (ND) events have most particles produced at central rapidity, with few

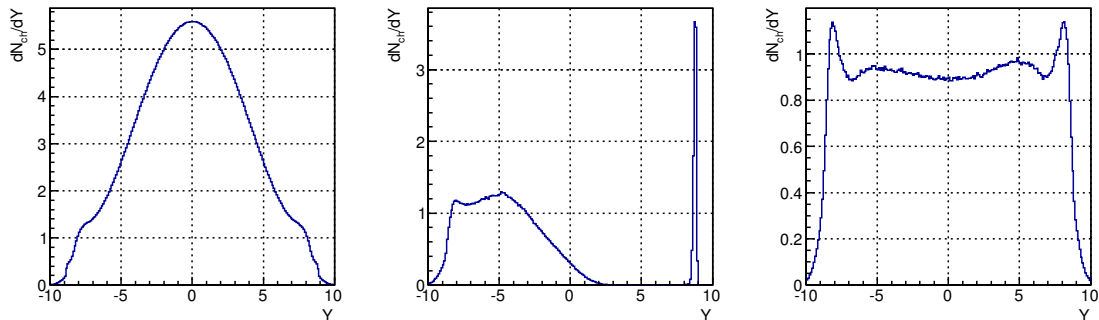


Figure 1.4: From left to right, the rapidity distributions for non-diffractive, single diffractive and double diffractive events respectively, using Pythia (Perugia-0 tune [25]) generated data at  $\sqrt{s} = 7$  TeV.

at forward rapidities.

Though they clearly have different structures, it is difficult to completely distinguish between diffractive and non-diffractive events; DD and ND events can have particles throughout the rapidity range which will trigger a minimum-bias trigger. The SD event type may be recognised as having left one side of the detector empty.

As suggested by the shapes of the rapidity distributions in Figure 1.4, the physical processes behind diffractive and non-diffractive events can be quite different. Ideally, the two types of events would be separated; the study of colour exchanging interactions between partons would best be served with non-diffractive events. However, given the difficulty of such a selection, the single-diffractive events can be removed to leave a so-called ‘non-single-diffractive’ (NSD) sample. This still leaves DD events, difficult to disentangle from ND events, but its contribution to the inelastic cross-section is not too significant, of the order 10% [26] of the total.

Thus, historically, results have been reported for the NSD event class, as have the re-

sults in this thesis. The inelastic event class, combining all detected events diffractive or not, has also been used, having the advantage of smaller event level corrections; results from this thesis are also reported for this class of events.

### 1.5.2 Pomeron exchange

Hadron collisions which involve a ‘soft’ interaction (low momentum exchange), such as diffractive events, cannot be modelled by perturbative QCD due to the large value of the strong coupling. Regge theory can successfully be used here, describing the interaction as a scattering event with the exchange of a ‘Regge-pole’: an object with angular momentum (or spin)  $J$  that is complex [27]. The amplitude of such a scattering is the sum of all the possible exchange particles. These objects can be organised according to their spin  $J$  and mass  $M$  with:

$$J = \alpha_0 + \alpha'(t)M^2, \quad (1.11)$$

where  $\alpha_0$  is the Regge intercept and  $\alpha'(t)$  is the Regge slope for a given exchange momentum  $t$  [28]. Hadrons in a family sharing isospin and other quantum numbers lie on a trajectory according to this relation, as shown in a Chew-Frautschi plot in Figure 1.5. The hadron resonances occur at integer values of  $J$  for mesons.

Regge theory predicts [27] that the total interaction cross-section between hadrons

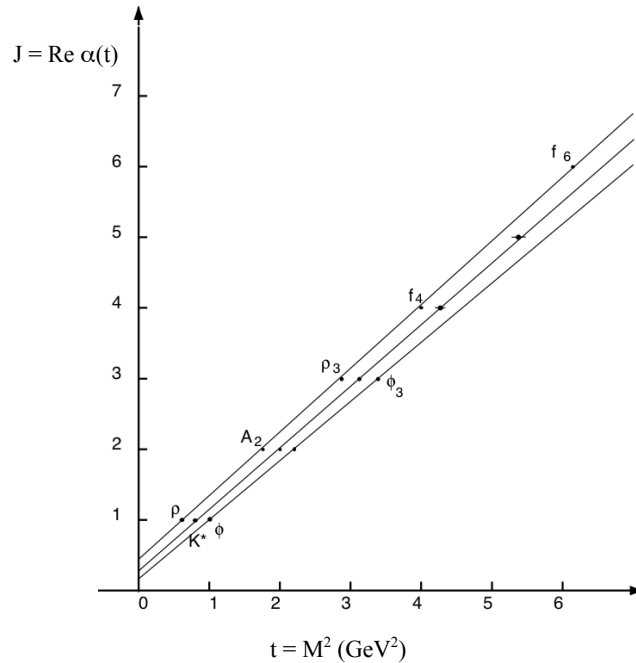


Figure 1.5: A Chew-Frautschi plot from [28] relating angular momentum to the square of exchange energy or mass, for a group of mesons.

is linked to the centre of mass energy as:

$$\sigma_{total} \propto s^{\alpha_0 - 1} . \quad (1.12)$$

For low energy, long-range interactions where the exchange particle is a meson with Regge-intercept  $< 1$ , the total cross-section would decrease with energy. However, the cross-section begins to rise above a certain energy, indicating the exchange of a new trajectory of particles.

The Pomeron is a particular Regge trajectory in the Chew-Frautschi plot with a Regge intercept of  $> 1$ , and fits with the inelastic cross-section increase with energy [28]. It is a hypothetical particle with quantum numbers of the vacuum, and is a colour singlet state, which describes high energy scattering well. Its colour sin-

glet state means it does not radiate quarks and gluons to give particles as does the gluon. A Pomeron exchange between two hadrons can cause both to dissociate into a shower of particles in the forward rapidity regions, with no particles in between due to the Pomeron not radiating partons: this is the rapidity gap.

In the simplest form of Pomeron exchange, it can be considered as the exchange of two gluons between partons of the scattering hadrons. As the collision energy increases, higher order exchanges contribute with more complicated combinations of gluons, or multiple Pomerons. However, at higher energies, especially in the collision of hadrons with partonic structure (as opposed to lepton-hadron collisions), the initial parton-parton interaction can be followed by further interactions that produce particles, thus ‘obscuring’ the rapidity gap with new particles [29].

### 1.5.3 Simulating Proton-Proton Collisions

Simulations of proton-proton collisions are created using Monte Carlo (MC) generators, which use pseudo-random number generators to model the interaction between the partons of the colliding hadrons. The two generators used in this thesis are Pythia [30] and Phojet [31]. The Pythia version used is Pythia6.4 Perugia-0 tune [25], referred to in this work as simply ‘Pythia’, and the Phojet version is 1.12, referred to as simply ‘Phojet’.

Pythia uses a perturbative QCD inspired model [30] in which parton-parton inter-

actions are described by perturbative QCD. This works well for large momentum transfers, but as the momentum transfer approaches zero, the interaction cross-section diverges. A cut-off  $p_T$  of  $\sim 2$  GeV/c is used to curb these divergences by regularising the interaction cross-section at low momentum transfers. This also controls how many initial parton interactions occur. Also modelled by the generator is string fragmentation, initial and final state parton showers and particle decays to provide a full simulation of a hadronic collision. The Perugia-0 version is tuned to CDF data, focusing particularly on colour re-connections during the fragmentation of the simulated collision, allowing the QCD strings of the parton-parton interactions to interact to minimise their potential energy [25].

Phojet uses perturbative QCD for hard parton interactions, and the Dual-Parton Model (DPM) [32] and the Quark-Gluon String Model (QGSM) for soft interactions [31]. These soft interaction models are based on the exchange of reggeons, and allow the exchange of multiple Pomerons, equivalent to multiple parton interactions, due to the inclusion of higher order terms in the expansion of QCD required for high collision energy, soft-parton interactions. It has been shown to describe well the data up to  $\sqrt{s} = 1800$  GeV [33], and to LHC energies for some measurements where other generators do not perform so well [34].

## 1.6 Koba-Nielsen-Oleson scaling

Feynman suggested that the average number of particles produced in collisions rises with the logarithm of  $\sqrt{s}$  [35]. This conclusion is reached by analysing the probability of finding a particle of type  $i$  for a given momentum and mass:

$$P_i(p_T, p_Z, m) = f_i(p_T, \frac{p_Z}{W}) \frac{dp_Z d^2 p_T}{E}, \quad (1.13)$$

where  $W = \sqrt{s}/2$  is half the collision energy, equal to the energy of one of the colliding particles if colliding identical beams, and  $f_i$  is the structure function which is hypothesised to be independent of  $W$ . Through its integration, outlined in [36], the following equation can be reached:

$$\bar{n} = 2f_i(\frac{p_Z}{W} = x_F = 0) \ln W + \text{constants}, \quad (1.14)$$

where  $x_F$  is known as Feynman-x and is the fraction of the colliding particle energy carried as forward momentum by the particle, and the constants refer to other terms which are independent of  $W$ . The scaling of the mean multiplicity with the natural log of the collision energy is called ‘Feynman-scaling’.

Koba-Nielsen-Oleson (KNO) scaling [37] assumes Feynman-scaling, and is derived [38] from considering  $q$  particles chosen from a group of  $n$  particles, where each particle has some energy  $E_q$  and momentum  $p_q$ :

$$\langle n(n-1)\dots(n-q+1) \rangle = \int f^q(x_{F,1}, p_{T,1}; \dots; x_{F,q}, p_{T,q}) \frac{d^3 p_1}{E_1} \dots \frac{d^3 p_q}{E_q}, \quad (1.15)$$

where  $f^q$  is an inclusive function that is assumed to obey Feynman-scaling. In [38], it is shown that by making the substitution

$$\frac{d^3 p_i}{E_i} = \frac{dx_{F,i} d^2 p_{T,i}}{\sqrt{x_{F,i}^2 + \frac{4m_i^2}{s}}}, \quad (1.16)$$

where  $m_i$  is the transverse mass and integrating equation 1.15 by parts gives the following:

$$\langle n(n-1)\dots(n-q+1) \rangle \sim \overline{f^q}(0, \dots, 0) \ln^q \left( \frac{s}{m^2} \right) + \mathcal{O} \left( \ln^{q-1} \left( \frac{s}{m^2} \right) \right), \quad (1.17)$$

where  $m^2$  is some typical mass and

$$\overline{f^q}(x_{F,1}, \dots, x_{F,q}) = \int d^2 p_{T,1} \dots d^2 p_{T,q} f^q(x_{F,1}, p_{T,1}; \dots; x_{F,q}, p_{T,q}). \quad (1.18)$$

By keeping only the leading logarithm terms, this becomes

$$\overline{n^q} \sim \overline{f^q}(0, \dots, 0) \ln^q \left( \frac{s}{m^2} \right) \quad (1.19)$$

and so the average multiplicity is

$$\overline{n} \sim \overline{f^1}(0) \ln \left( \frac{s}{m^2} \right). \quad (1.20)$$

It is shown in [38] that this leads to a result that is uniquely defined by its moments, and eventually yields the following:

$$P(n) = \frac{1}{\overline{n}} \Psi \left( \frac{n}{\overline{n}} \right), \quad (1.21)$$

where  $P(n)$  is the probability distribution of multiplicity and  $\Psi$  is an energy independent function, such that all collisions of the same incoming particles will lie on the same curve as a function of  $z = \frac{n}{\sqrt{s}}$  [37]. The moments that would be energy independent for this scaling are defined as:

$$C_q = \int_0^\infty z^q \Psi(z) dz , \quad (1.22)$$

and uniquely define the  $\Psi(z)$  which can have different forms depending on the colliding particles.

## 1.7 Negative Binomial Distribution

The Negative Binomial Distribution (NBD) has been shown [39] to fit multiplicity distributions rather well at hadron collision energies below 540 GeV [40]. It is a probability distribution of obtaining some random amount of successes in a series of Bernoulli trials until a fixed number of failures occur. Its probability mass function can be written as:

$$P^{NBD}(n, k) = \binom{n+k-1}{n} p^n (1-p)^k , \quad (1.23)$$

where  $n$  is the number of successes,  $k-1$  is the number of failures before the  $k$ 'th failure and  $p$  is the probability of a successful Bernoulli trial. The binomial coefficient

is:

$$\binom{n+k-1}{n} = \frac{(n+k-1)!}{n!(k-1)!} = \frac{(n+k-1)(n+k-2)\dots(k)}{n!}, \quad (1.24)$$

which gives the number of ways to arrange  $n$  failures from a group of  $(n+k-1)$  trials. The number of trials in the coefficient is 1 less than the total number of trials, as the last trial is the  $k$ -th trial resulting in failure. In the limiting case of  $k \rightarrow \infty$  the NBD becomes the Poisson distribution, and when  $k = 1$  it becomes a geometric distribution  $P^{NBD}(n, 1) = (1-p)^n p$ . Examples of the NBD are shown in Figure 1.6.

For fitting to multiplicity distributions, it is represented in the form [40]:

$$P(\bar{n}, n, k) = \frac{k(k+1)\dots(k+n-1)}{n!} \frac{\bar{n}^n k^k}{(\bar{n}+k)^{n+k}}, \quad (1.25)$$

where  $\bar{n}$  is the average multiplicity,  $n$  is the multiplicity and  $k$  controls the shape of the function. The  $k$  parameter is related to the probability of a successful trial by  $p^{-1} = 1 + \bar{n}/k$  [39].

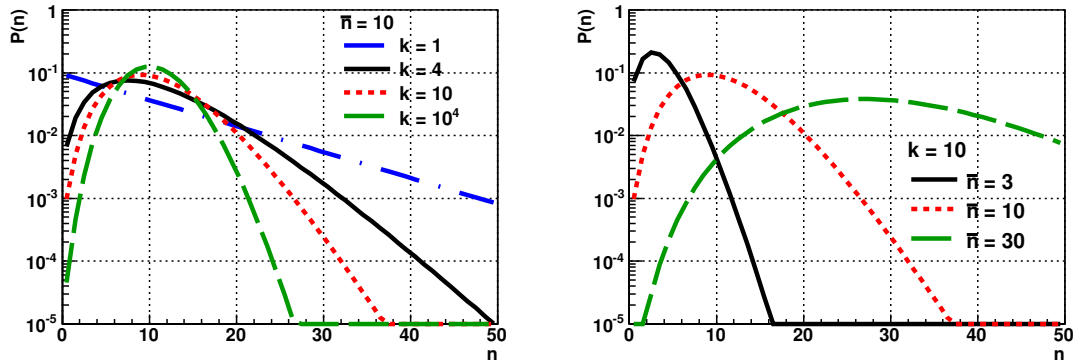


Figure 1.6: Examples of NBD's with parametrisation as in equation 1.25. The left panel shows NBDs of  $n$  with different  $k$  parameters for fixed  $\bar{n} = 10$ . The right panel shows NBDs of  $n$  with different  $\bar{n}$  parameters for fixed  $k = 10$ .

### 1.7.1 Interpretation of Multiplicity Distributions

The reason why the NBD should fit the lower energy multiplicity distributions in preference to other functions is not completely understood. One interpretation, however, is based on the recurrence relation of multiplicities; how the probability of an event with multiplicity  $n$  relates to that of  $n + 1$  [41]. The recurrence relation can be written as:

$$g(n) = (n + 1) \frac{P(n + 1)}{P(n)} . \quad (1.26)$$

In the case of independent emission, where the emission of a particle from the collision system is independent of other particles that may be present, the multiplicity distribution is Poissonian:

$$P(n) \propto \frac{\bar{n}^n}{n!} , \quad (1.27)$$

and the recurrence relation becomes some constant,  $g(n) = a$ .

For the NBD, the recurrence relation becomes:

$$g(n) = a + bn , \quad (1.28)$$

where the constants  $a = \frac{\bar{n}k}{\bar{n}+k}$  and  $b = \frac{\bar{n}}{\bar{n}+k}$ . In the context of this relation, different behaviours of particle production can be considered [42]. Already, it is seen that if  $b = 0$ , particles are produced independently of one another, but this assumes a Poissonian multiplicity distribution. Another simple case is stimulated emission, where the probability of the emission of a particle is enhanced by factor  $(n + 1)$  in

the presence of  $n$  particles, so  $a = b$  and  $g(n) = a(n + 1)$ . This gives  $P(n) = a^n$ , a NBD with  $k = 1$ .

If partial stimulated emission is the mechanism, then additional particles are produced either independently, or by stimulated emission, relating to the  $a$  and  $bn$  terms of the recurrence relation respectively. The relation then becomes:

$$g(n) = a\left(1 + \frac{n}{k}\right), \quad (1.29)$$

where  $k$  represents a number of identical ‘clusters’ with average multiplicity  $\frac{n}{k}$ . So  $k^{-1}$  is the average fraction of particles already present which are stimulating the emission of new particles.

The ‘clan’ model [41] considers the recurrence relation in terms of particles produced through cascades, where the original particle known as the ‘ancestor’ could create new particles through cascading and change its own quantum numbers in the process. All the particles that stem from a common ancestor are grouped as a cluster. In terms of the recurrence relation, a particle can come from either a new 1-particle cluster or from an already existing cluster, the  $a$  and  $bn$  terms of the recurrence relation respectively. This can be applied to a limited interval in pseudorapidity as well as full phase space, where a cluster will have between all and none of its particles in the defined domain. A particle produced from a cluster defined in the domain is then in that domain-cluster, if it is produced from a cluster outside the domain it is considered a new 1-particle domain-cluster. Thus, the  $(n + 1)$ -th particle can come

from a new domain-cluster ( $a$  in recurrence relation) or from a pre-existing domain cluster ( $bn$  in recurrence relation).

The probability  $P(N)$  of producing  $N$  clusters is assumed as Poissonian, and the probability of a cluster producing  $n_C$  particles first requires that the clan not be empty:

$$P_C(n_C = 0) = 0 , \quad (1.30)$$

where  $P_C(n_C)$  is the probability of the creation of a cluster with multiplicity  $n_C$ , and then that a new particle is produced depending on the particles in the cluster  $n_C$ :

$$g_C(n_C) = (n_C + 1) \frac{P_C(n_C + 1)}{P_C(n_C)} = pn_C , \quad (1.31)$$

where  $p$  is the probability of production and assuming  $n_C \geq 1$ . By iterating this equation, one gets the probability of a cluster with multiplicity  $n_C$ :

$$P_C(n_C) = P_C(1) \frac{p^{n_C-1}}{n_C} . \quad (1.32)$$

Through iterations shown in the appendix of [42], the probability of a total multiplicity  $n$  is:

$$P(n) \propto \frac{a(a+b)\dots[a+b(n-1)]}{n!} , \quad (1.33)$$

where  $a = \bar{N}P_C(1)$ ,  $b = p$  and these relate to the  $k$  parameter with  $k = \frac{a}{b}$ . This can

be rearranged to give the probability in the more familiar notation:

$$P(n) \propto p^n \frac{k(k+1)\dots[k+(n-1)]}{n!} = \binom{n+k-1}{n} p^n, \quad (1.34)$$

a NBD as in equation 1.25. Thus, if the multiplicity distributions of hadron collisions are produced via the clan model, then they will continue to follow a NBD.

Above collision energies of  $\sqrt{s} = 540$  GeV, it was found that a single NBD no longer provided a satisfactory fit to the multiplicity distributions [40], a combination of two NBD's was used instead to account for the shoulder structure seen towards higher multiplicities. These two NBD's were interpreted as the multiplicity distributions of soft and semi-hard events, of which only the latter had mini-jets [43], an observable open to different technical definitions [40, 44], generally characterised by a group of particles clustered together with transverse energy above  $\sim 1$  GeV. It was found that the fraction of events with mini-jets agreed with the fraction of semi-hard events.

The fit has five free parameters:

$$P(n) = \alpha_{soft} P^{NBD}(n; \bar{n}_{soft}; k_{soft}) + (1 - \alpha_{soft}) P^{NBD}(n; \bar{n}_{semi-hard}; k_{semi-hard}), \quad (1.35)$$

where  $\alpha_{soft}$  is the relative contribution of soft and semi-hard events to the overall distribution, and the two NBD's each have two parameters. This does not distinguish different production mechanisms between soft and semi-hard events, as they

are simply differently classified events. However, the soft events still exhibited KNO scaling while semi-hard or hard events do not. It was observed that the average multiplicity of semi-hard events is approximately twice that of soft events [43].

Another approach to addressing the change in shape of the multiplicity distribution above ISR energies is to consider multiple-particle exchanges, where multiple parton-parton interactions occur during the collision between the two hadrons. The contributions to the overall multiplicity distribution may come from events with a single hard parton-pair interaction, double and possibly triple interactions also [45]. The single parton interaction seems to produce an energy independent distribution, with the multiple parton interactions increasing with collision energy. This also has an effect on the average transverse momentum for higher multiplicities, which is possibly due to the occurrence of mini-jets at higher energies [46, 47].

## 1.8 Previous Experimental Results

### 1.8.1 Charged Particle Multiplicity

The CERN Intersecting Storage Ring (ISR) was the first hadron collider, producing collisions between protons with centre of mass energy  $\sqrt{s} \sim 30, 44, 53$  and  $62$  GeV. These were studied using the Split Field Magnet (SFM) Detector, which tracked charged particles through its 1 T magnetic field with the then new technology of

Multi-Wire Proportional Chambers. The multiplicity distributions observed at these energies for NSD events are shown in Figure 1.7, and all follow KNO scaling [48].

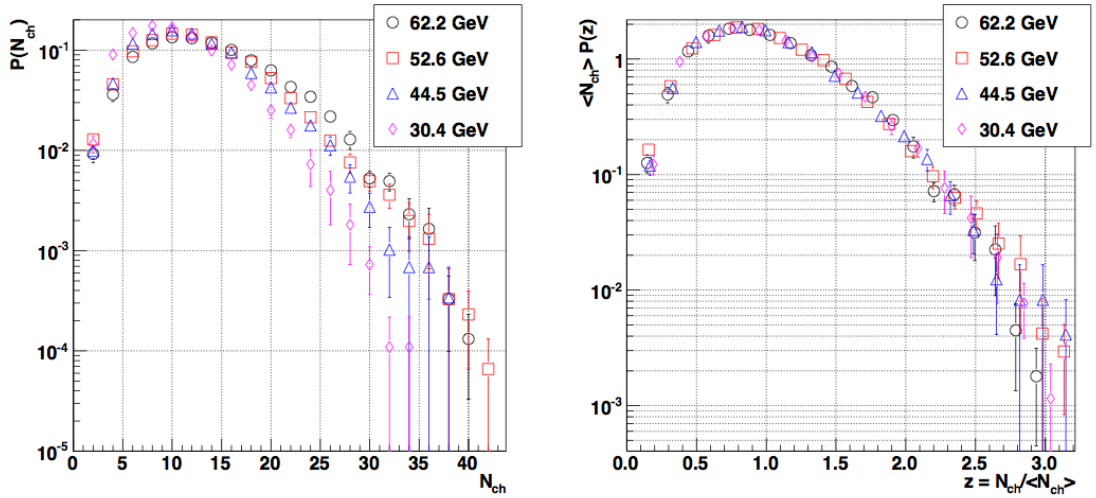


Figure 1.7: The normalised multiplicity distributions in full phase space (left) observed at the ISR [48] with  $\sqrt{s}$  between 30.4 and 62.2 GeV, also shown in KNO variables (right) [39] for NSD interactions.

The Underground Area 5 (UA5) experiment observed collisions at the SPS collider from  $\sqrt{s} = 200$  to 900 GeV. It measured multiplicity distributions in pseudorapidity intervals up to  $|E_T| < 5.0$  as well as full phase space for NSD collisions of protons and anti-protons. The observed multiplicity distribution in full phase space at  $\sqrt{s} = 900$  GeV was the first that could not be described by a single NBD fit, also indicating a violation of KNO scaling, as shown in Figure 1.8.

A combination of two NBDs was successfully fitted to the UA5  $\sqrt{s} = 900$  GeV distribution as shown in Figure 1.9, using the form given in equation 1.35 describing contributions to the total multiplicity from soft and semi-hard events. The average

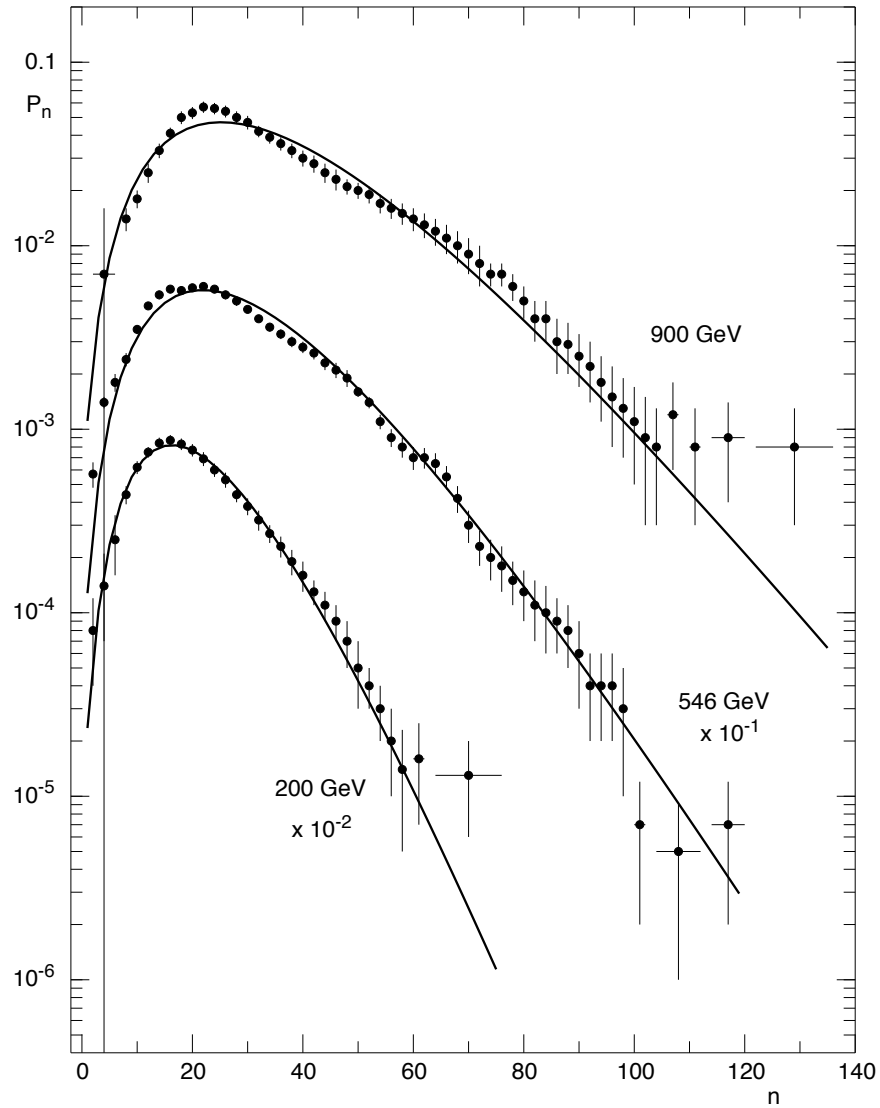


Figure 1.8: UA5 multiplicity distributions in full phase space (from an acceptance of  $|\eta| < 5.0$ ) for NSD proton-anti-proton collisions at  $\sqrt{s} = 200, 546$  and  $900$  GeV [41], each showing the best fit of a NBD. The  $\sqrt{s} = 900$  GeV data clearly show a shoulder structure above  $n = 60$ .

multiplicity of soft events was seen to be roughly half that of semi-hard events, and still followed KNO scaling, unlike semi-hard events [42].

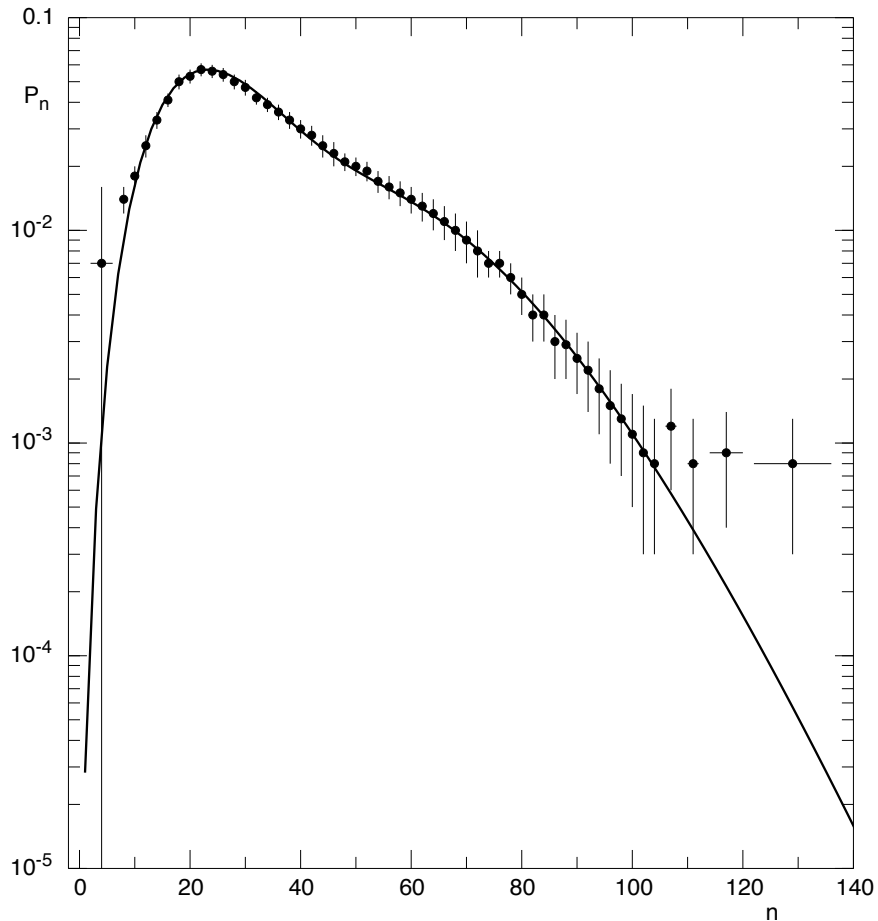


Figure 1.9: UA5 multiplicity distribution in full phase space (from an acceptance of  $|\eta| < 5.0$ ) for NSD proton-anti-proton collisions at  $\sqrt{s} = 900$  GeV [41], shown along with the best fit of the sum of 2 NBDs, reproducing the shoulder structure above  $n = 60$ .

The Tevatron at Fermilab collided protons with anti-protons up to  $\sqrt{s} = 1800$  GeV, and the E735 experiment published multiplicity measurements for NSD events in the full phase space, these are shown in comparison to lower collision energy distributions in KNO variables from UA5 and ISR in Figure 1.10. The onset of KNO scaling violation is clearly visible as the collision energy increases.

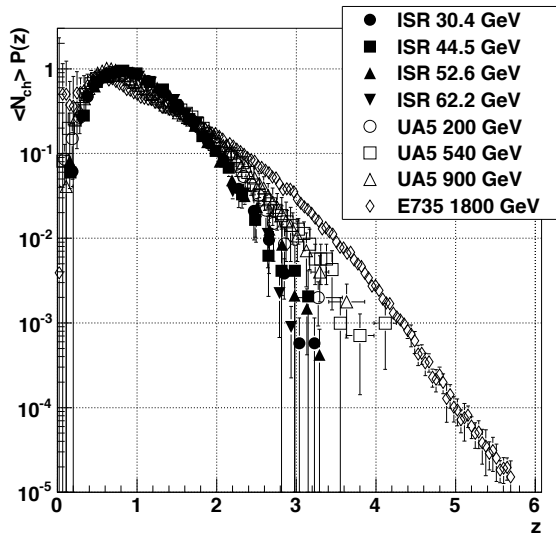


Figure 1.10: The violation of KNO scaling for increasing collision energy, demonstrated by the full phase space multiplicity distributions from E735, UA5 and ISR shown in KNO variables. The filled points from the ISR fall on top of each other, following KNO scaling. Empty points at higher energies lie on separate trajectories, violating the predicted scaling. Figure taken from [39]. Data from [48], [49], [50] and [45]

The Collider Detector experiment at Fermilab (CDF) observed proton-anti-proton collisions with  $\sqrt{s} = 600$  GeV and 1800 GeV. The data were separated into soft and hard events by classifying events with a jet cluster with transverse energy above 1.1 GeV as hard, and those without as soft [44]. The multiplicity distributions for these inelastic event classes in KNO variables is shown in Figure 1.11. The sum of the soft and hard events, the minimum bias event selection, shows KNO scaling within errors for pseudorapidity interval of  $\pm 1$ , as well as the sub-group of soft events, between the two collision energies. The hard events, those deemed to have mini-jets present, show a clear violation of KNO scaling between the two energies. It was theorised that the soft and semi-hard event types could be interpreted as single and double parton interactions [47].

## 1.8. PREVIOUS EXPERIMENTAL RESULTS

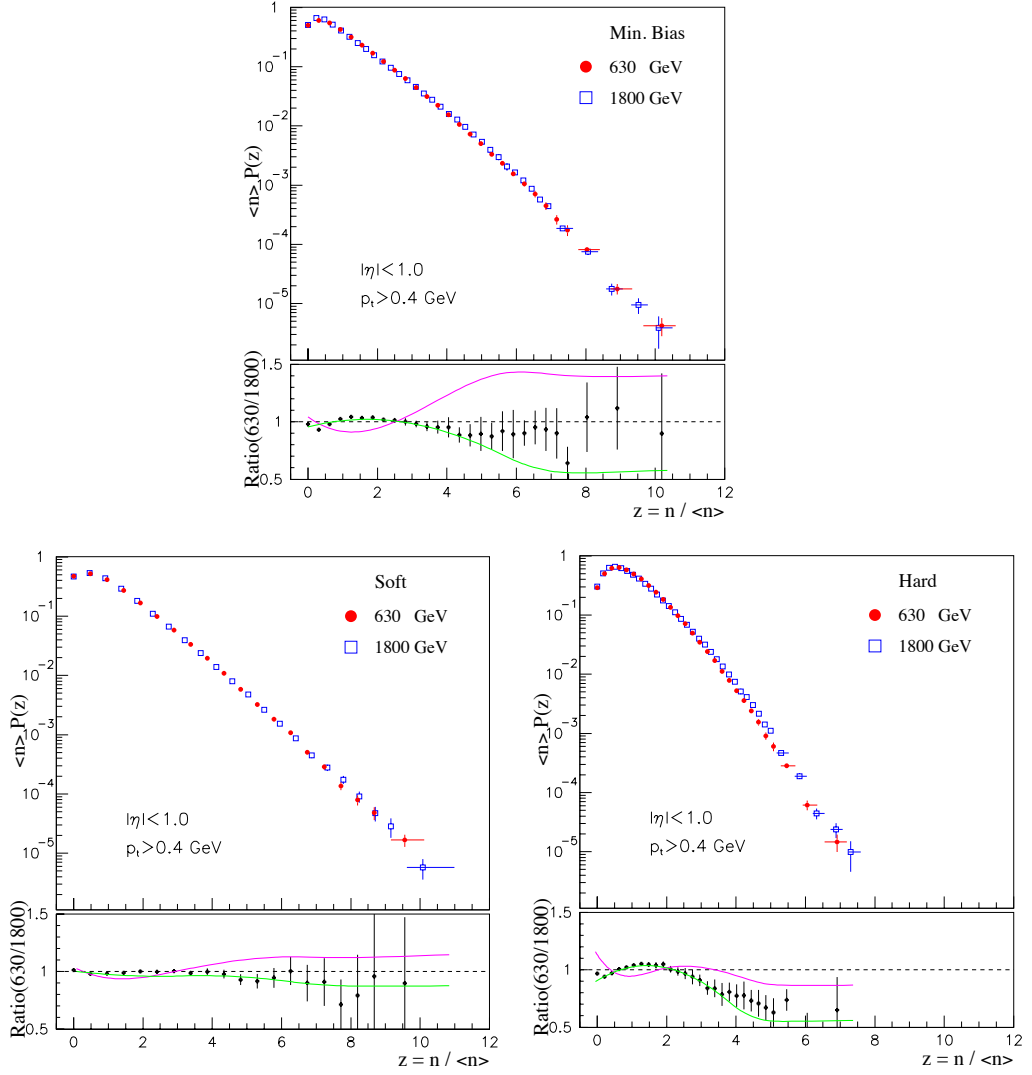


Figure 1.11: Multiplicity distributions from CDF [44] in KNO variables for different event selections at  $\sqrt{s} = 630 \text{ GeV}$  and  $1800 \text{ GeV}$ . The top panel includes all minimum bias data, the bottom left comprises soft events and the bottom right comprises hard events.

The ALICE [51] and CMS [52] experiments have both published multiplicity distributions for proton-proton collisions at  $\sqrt{s} = 900, 2360$  and  $7000$  GeV for NSD events [23, 53, 54]. ALICE also selects all inelastic events, and inelastic events with at least 1 track in the pseudorapidity selection. The distributions from both in comparable pseudorapidity intervals are shown in Figure 1.12, indicating excellent agreement between the two experiments. As the CMS detector is designed for high luminosity data taking, it has collected enough data to populate the exponentially reducing tail of the multiplicity distribution, further than ALICE has currently published.

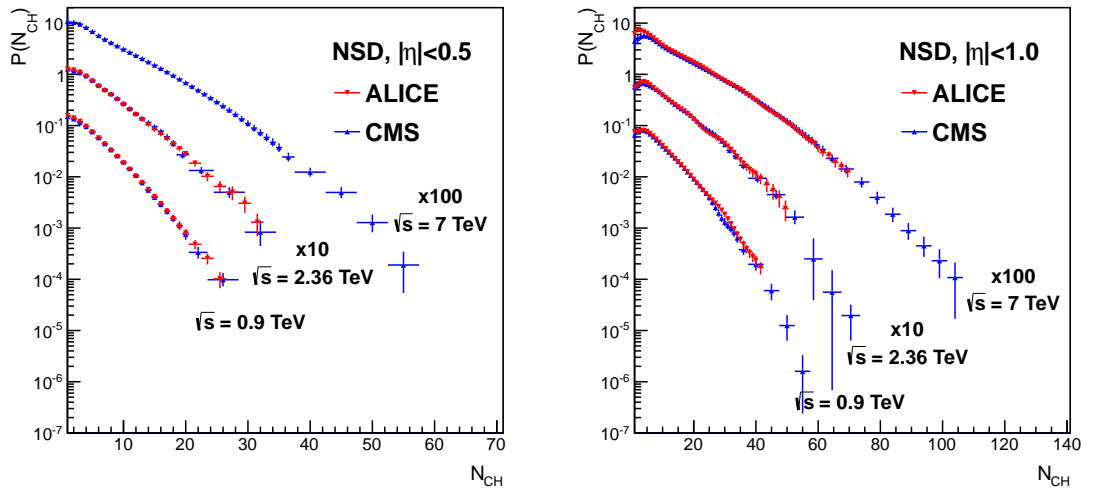


Figure 1.12: Published multiplicity distributions from ALICE [23, 53] and CMS [54], for proton-proton collision energies of  $\sqrt{s} = 0.9, 2.36$  and  $7$  TeV, and pseudorapidity range of  $|\eta| < 0.5$  ( $|\eta| < 1.0$ ) shown in the left (right) panel. Note that for  $\sqrt{s} = 7$  TeV and  $|\eta| < 1.0$ , the ALICE distribution is from inelastic events rather than NSD, but this only affects the first few low multiplicity bins.

A comparison of multiplicity distributions at  $\sqrt{s} = 900$  and  $7000$  GeV for a small and large pseudorapidity interval is shown by CMS in Figure 1.13. It clearly shows a strong violation of KNO scaling in the  $|\eta| < 2.4$  interval, yet for  $|\eta| < 0.5$  the scaling

holds. This is interpreted as the increasing contribution of multiple sub-processes of differing hardness in elastic collisions between hadrons [54].

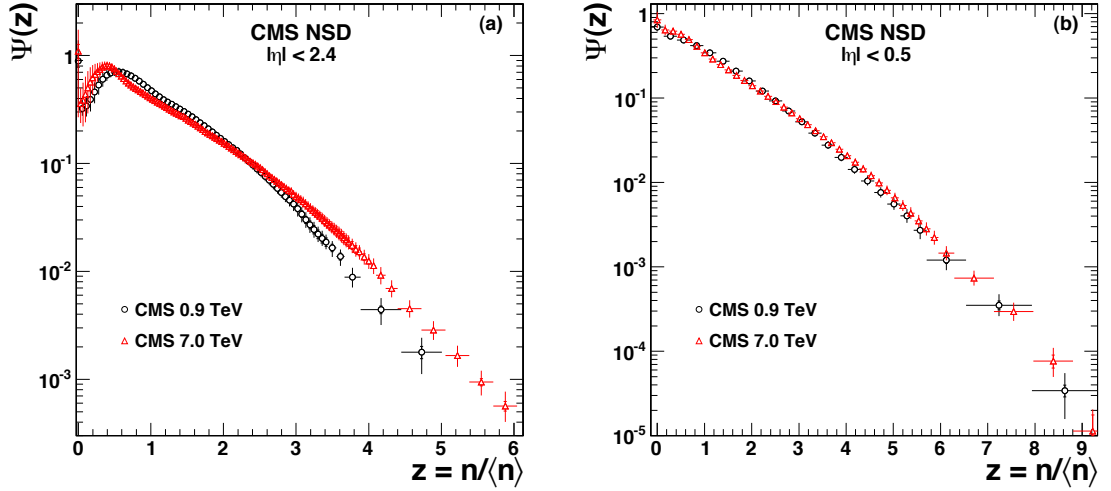


Figure 1.13: Multiplicity distributions in KNO variables from CMS [54] at  $\sqrt{s} = 0.9$  and 7 TeV in the pseudorapidity interval  $|\eta| < 2.4$  in the left panel (a) and  $|\eta| < 0.5$  in the right (b).

Figure 1.14 shows the pseudorapidity density in the central region for NSD and inelastic proton-proton collisions as a function of centre of mass energy. The NSD data points are from the range  $|\eta| < 0.5$ , the inelastic points from  $|\eta| < 1.0$  [23]. The events of type INEL>0 are inelastic events with at least 1 track in  $|\eta| < 1.0$ , so the pseudorapidity density is higher due to the exclusion of events with 0 multiplicity (but have tracks outside this interval).

The multiplicity distribution in the range  $|\eta| < 0.5$  can provide the pseudorapidity density through its average value, due to the plateau structure of the pseudorapidity density in the central region.

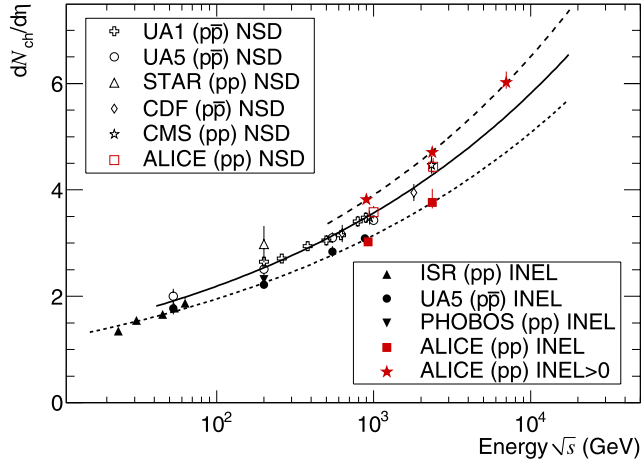


Figure 1.14: Pseudorapidity density in the range  $|\eta| < 0.5$  for NSD events, and in the range  $|\eta| < 1.0$  for inelastic events, as a function of the collision energy [23]. The lines show power law fits to the data. Data points from [54, 55, 56, 57, 58, 59, 60, 61].

## 1.8.2 Mean Transverse Momentum

Early measurements of the mean transverse momentum with respect to multiplicity for hadron collisions showed a similar structure above ISR energies, sometimes referred to as the ‘ledge’ effect; the rise-plateau-rise shape of the correlation shown in [62].

Figure 1.15 shows the mean transverse momentum published by ALICE for inelastic events in the pseudorapidity interval  $|\eta| < 0.8$  at the proton-proton collisions energy  $\sqrt{s} = 900$  GeV [63]. The mean  $p_T$  for each multiplicity bin is extracted from a fit to the  $p_T$  spectrum for all charged particles. The measurement was made with two minimum  $p_T$  thresholds of 0.15 GeV/c and 0.5 GeV/c, and compared to various tunes of the Pythia MC and to the Phojet MC generators revealing the failure to reproduce the observed shapes for most of them. There is clearly a change in the

slope with increasing multiplicity, but further structure cannot be discerned.

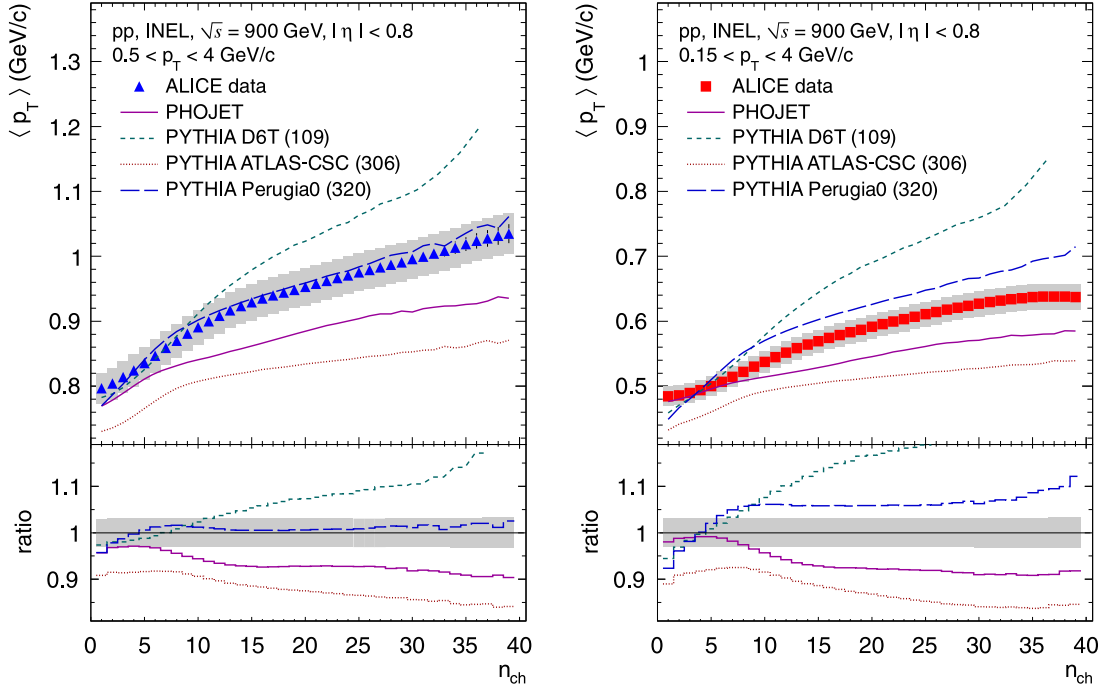


Figure 1.15: The ALICE published data of mean  $p_T$  versus charged multiplicity for inelastic proton-proton collisions at  $\sqrt{s} = 900$  GeV, with minimum  $p_T$  of 0.15 GeV/c (left panel) and 0.5 GeV/c (right panel), compared to various MC generators [63].

The CDF Collaboration, at the Tevatron collider, presented a measurement of mean  $p_T$  versus multiplicity in the pseudorapidity interval  $|\eta| < 1.0$  for tracks with  $p_T$  above 0.4 GeV/c [44], comparing two sub-samples of the minimum bias data deemed ‘hard’ and ‘soft’, as shown in Figure 1.16. The soft sample is seen to have a collision energy invariant correlation of mean  $p_T$  with charged multiplicity, whereas the hard sample shows a generally larger mean  $p_T$  for the higher collision energy. The shape of the minimum bias correlation shows the same change in slope as seen in lower energy measurements, with hints of a rise in the tail of the distribution, but as the statistics run out here, another change in the slope cannot be concluded. It is

also worth noting that in the separate data samples, the first change in slope of the correlation is present for the soft events, whereas the hard events show a more linear shape.

A comparison of soft and hard events has been published also by ALICE [64] for  $\sqrt{s} = 900$  and  $7000$  GeV, for charged tracks in  $|\eta| < 0.8$  and with  $p_T > 0.5$  GeV/c, shown in Figure 1.17, although there is no comparison between collision energies for hard and soft events, and different minimum  $p_T$  thresholds are not considered. The hard and soft events are distinguished by the presence of a charged track with  $p_T > 2$  GeV/c, which suggests a hard parton interaction during the collision. The results are compared to various MC generator tunes of Pythia. The rise of mean  $p_T$  predicted by many of the MC generators at high multiplicity for  $\sqrt{s} = 7000$  GeV is not reproduced in the minimum bias data. After the initial change in slope of the correlation at low multiplicity, the slope is unchanged up to the highest presented multiplicity. The mean  $p_T$  increases with multiplicity, confirming that this trend seen at lower energies continues to  $\sqrt{s} = 7000$  GeV.

The mean  $p_T$  for NSD or inelastic proton-proton events for various collision energies is shown in Figure 1.18, taken from the ALICE publication [63].

## 1.8. PREVIOUS EXPERIMENTAL RESULTS

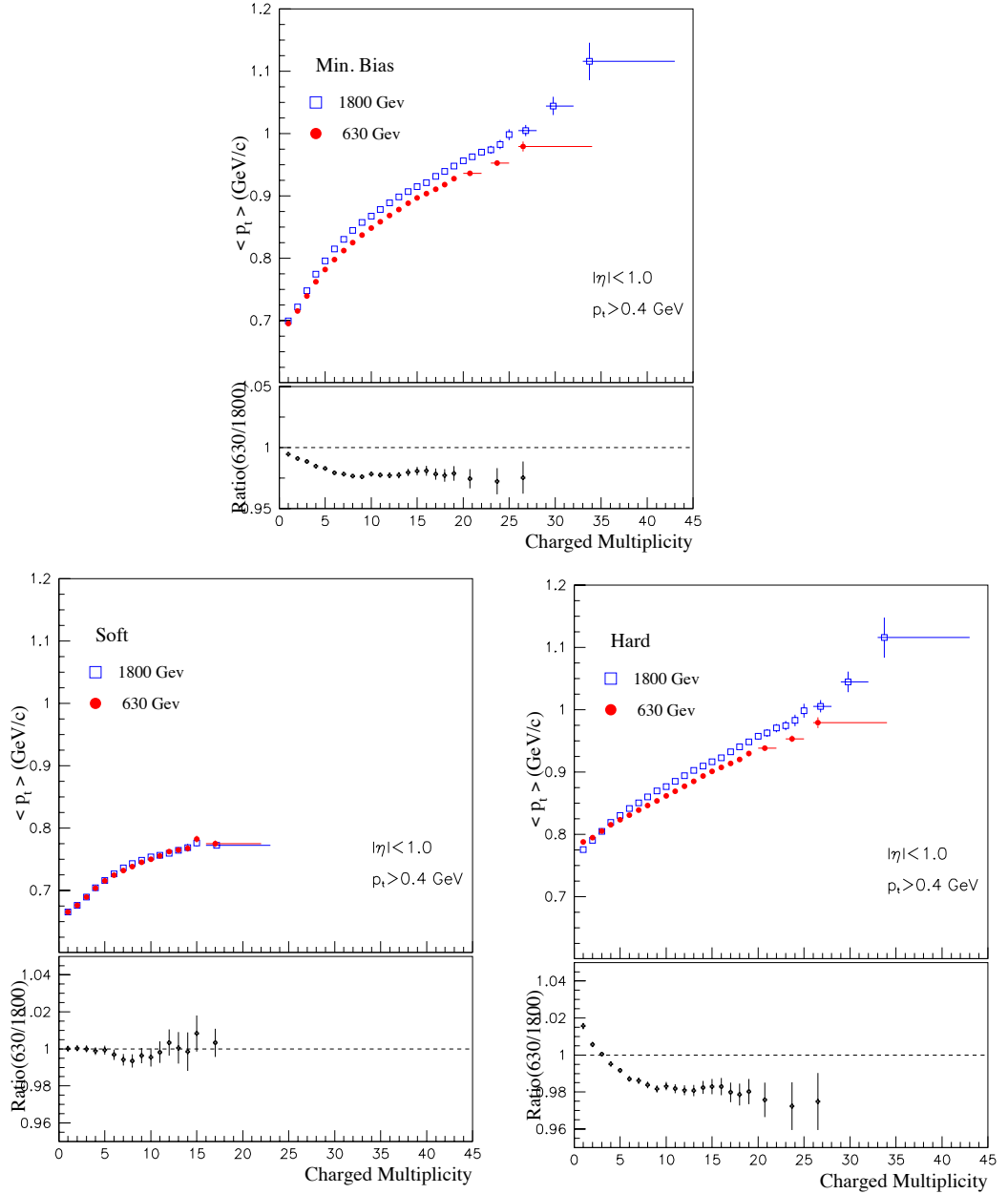


Figure 1.16: Average transverse momentum per event as a function of multiplicity from CDF [44] for different event selections at  $\sqrt{s} = 630 \text{ GeV}$  and  $1800 \text{ GeV}$ . The top panel includes all minimum bias data, the bottom left comprises soft events and the bottom right comprises hard events.

## 1.8. PREVIOUS EXPERIMENTAL RESULTS

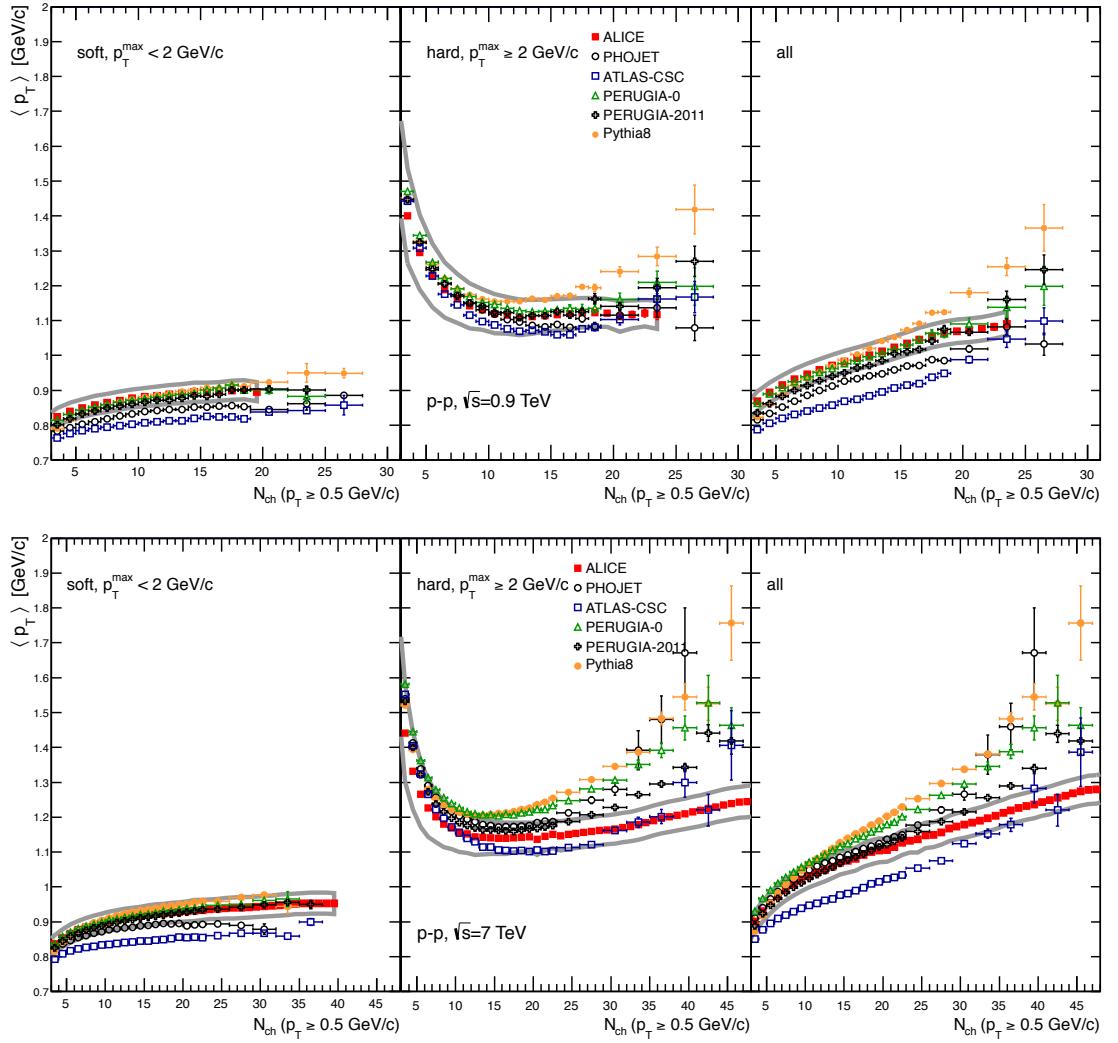


Figure 1.17: Mean  $p_T$  versus charged multiplicity for inelastic proton-proton collisions at  $\sqrt{s} = 900$  GeV (top row) and  $\sqrt{s} = 7000$  GeV (bottom row) [64]. The events are divided into soft and hard events, left and middle panels respectively, with the correlation for all events shown in the right hand panels.

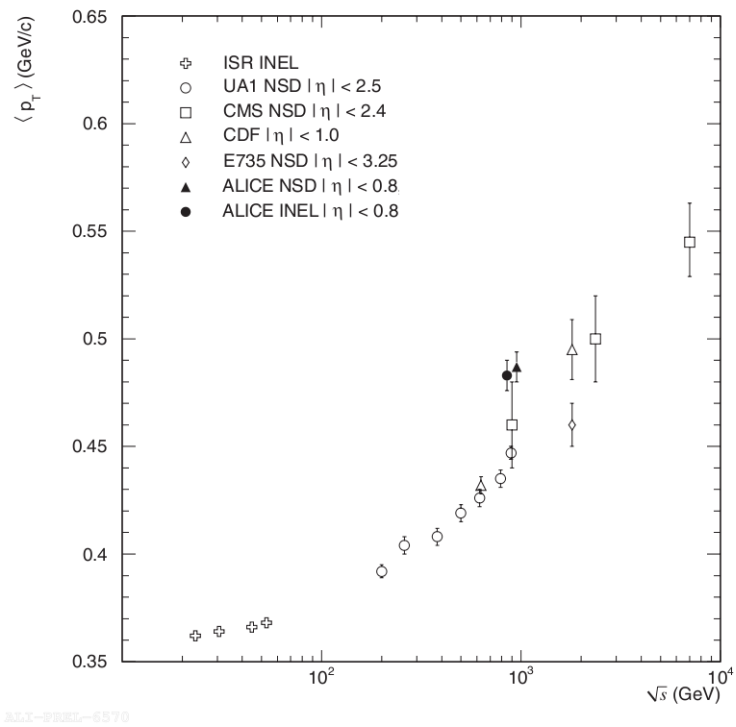


Figure 1.18: The mean  $p_T$  per event for NSD and inelastic proton-proton collisions from various hadron collider experiments as a function of collision energy. Figure is taken from [63]. Data points are from [61, 65, 66, 67, 68, 69].

## 1.9 Summary

The theory of QCD predicts the state of QGP in high energy density environments such as those produced in heavy-ion collisions, and possibly a minority of very high multiplicity proton-proton collisions. Measurements of the QGP show it is a short-lived state of dense, strongly interacting matter in thermal equilibrium, that rapidly expands and cools. Proton-proton collisions provide a vital baseline with which to compare to and understand heavy-ion collisions, and in themselves provide an insight to the fascinating physics of parton interactions and particle production through measurements of global observables, such as multiplicity and average transverse momentum per event.

---

---

# CHAPTER 2

---

## THE ALICE EXPERIMENT AT THE LHC

### 2.1 The LHC

The Large Hadron Collider [70] is the flagship accelerator at the CERN laboratory in Switzerland. It is a superconducting synchrotron designed to accelerate protons and lead ions, bringing them to collision in the centre of detectors along its 26.7 km circumference.

At 45 – 170 m below the ground, in the tunnels excavated for the LEP accelerator, the LHC provides collisions for four main experiments. There are two high luminosity experiments, ATLAS [71] and CMS [52], looking for rare events, a beauty physics experiment, LHCb [72], and a heavy ion experiment, ALICE [51]. These four are housed in caverns at intersection points along the LHC, as shown in figure 2.1. In addition, smaller experiments share the interaction points of the large detectors to study cross-sections [73], forward particle production [74] and search for exotic particles [75].

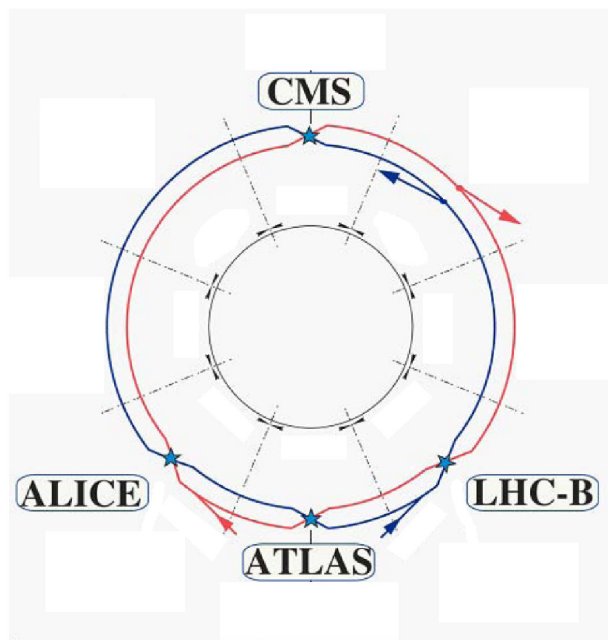


Figure 2.1: Schematic layout of the LHC and its four main experiments [70]

The protons, to be fed into the LHC, are created initially by stripping hydrogen atoms of their electrons. These protons are then injected from the LINAC2 (linear accelerator) into the Proton Synchrotron Booster which accelerates the protons to an energy of 1.4 GeV before injecting them into the Proton Synchrotron (PS). The

PS ring accelerates protons up to 25 GeV, at which point they are fed into the SPS, which accelerates protons to 450 GeV. Then they can be fed in either direction into the LHC, where they are accelerated up to 4 TeV. Figure 2.2 shows the layout of the injection complex.

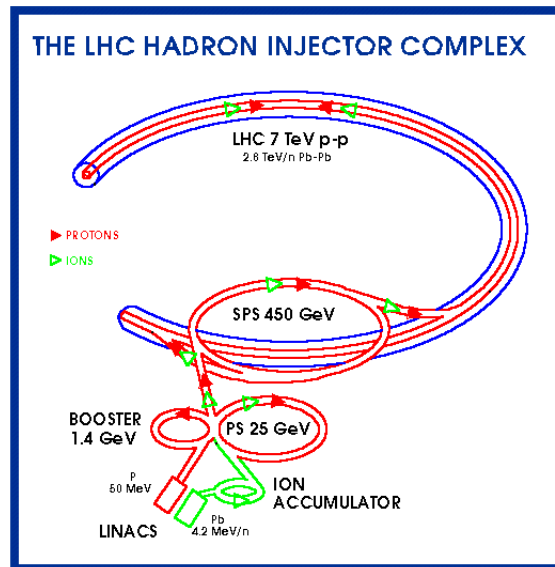


Figure 2.2: The various stages of acceleration of both protons and ions on their way to injection into the LHC [76]

The protons travel inside the LHC in bunches separated by at least 25 ns in time, which defines one ‘bucket’, and the beam can be up to a millimetre wide, it is narrowed by focusing magnets around the collision points to achieve high luminosities. The LHC can circulate up to 2808 bunches of protons at the same time. The collision rate is the product of the luminosity and the collision cross-section, with the luminosity describing the particle flux per second of both beams per unit area and the cross-section describing the likelihood of an interaction between two particles. The design luminosity for proton-proton collisions is  $L = 10^{34} \text{ cm}^{-2}\text{s}^{-1}$ ,

and the proton-proton collision cross-section, at 7 TeV, for inelastic collisions is  $\sigma_{inel} = (69.4 \pm 7.3) \text{ mb}$  [77], where  $1\text{b} = 10^{-28} \text{ m}^2$ , giving a possible collision rate of 700 MHz. The highest achieved luminosity with the LHC machine so far is  $7.7 \times 10^{33} \text{ cm}^{-2} \text{ s}^{-1}$  as of 2012 [78]. The normal proton-proton luminosity delivered to ALICE is of the order  $10^{30} \text{ cm}^{-2}\text{s}^{-1}$ , giving a collision rate of the order  $10^5 \text{ Hz}$ .

For the heavy-ion programmes, carried out at the end of 2010 and end of 2011, purified lead was heated to  $500^\circ\text{C}$  to create lead vapour. This is ionised and mass separated to obtain  $Pb^{27+}$ . The ions were then accelerated and ionised further in stages before being fully ionised to become  $Pb^{82+}$  and reaching 177 GeV/nucleon inside the SPS. From here, they are injected into and accelerated by the LHC to 1.38 TeV/nucleon, corresponding to a collision energy of  $\sqrt{s_{NN}} = 2.76 \text{ TeV/nucleon}$ , or a total centre of mass energy of 574 TeV. Data were collected at an average luminosity of  $5 \times 10^{23} \text{ cm}^{-2}\text{s}^{-1}$  [79], with roughly  $10^7$  ions per bunch. Though the lead-ion runs are primarily intended for the ALICE experiment, the ATLAS and CMS experiments also recorded heavy-ion data at similar luminosities.

## 2.2 The ALICE detector

The sub-detectors which make up the ALICE experiment, as shown in Figure 2.3, may be grouped in terms of their function. There are tracking detectors which collect information about the path of charged particles, and can also be used to pinpoint

the interaction vertex. There are detectors which measure the rate of energy loss of particles,  $dE/dx$ , which is used to identify a particle's species, and those that use the time of flight for particle identification. Then, there is the electromagnetic calorimetry that detects and measures the energy of electrons and photons. The Muon Spectrometer tracks muons which are used to measure the production of heavy quark resonances via their dimuon decay products. The detectors in forward positions, as well as providing detector coverage at small angles to the beam line, are also used for global event characteristics and triggering the recording of an event. The pseudorapidity coverage of some of the ALICE sub-detectors is shown in Figure 2.4. Some detectors fall into more than one of the above categories, their information is used for multiple purposes.

The central barrel is contained inside the solenoid magnet of ALICE which produces a uniform magnetic field of 0.5 T over all the detectors inside it. This changes the trajectory of charged particles inside the magnet in the direction orthogonal to the beam line. In this field, particles with a transverse momenta of less than 50 MeV/c, emanating from the interaction point inside the beam pipe, will not reach the innermost layer of detectors. The solenoid magnet, a distinctive red in colour, is 15.8 m in diameter and 14.1 m in length, with a steel return yoke.

The forward muon spectrometer consists of a dipole magnet providing a 0.67 T magnetic field, 7 m from the interaction point. It is 5 m long, 9 m tall and made of 28 steel modules.

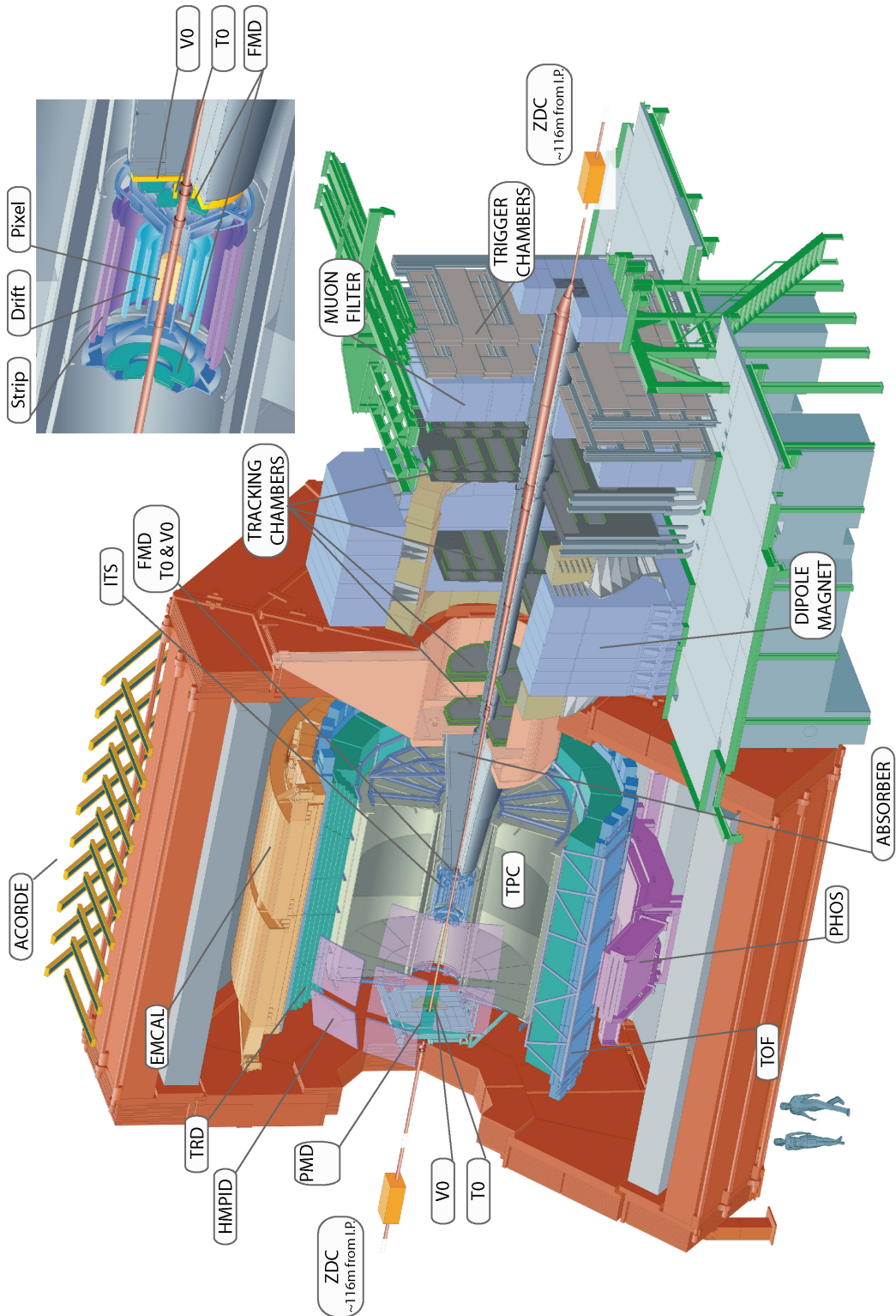


Figure 2.3: The ALICE detector [80]

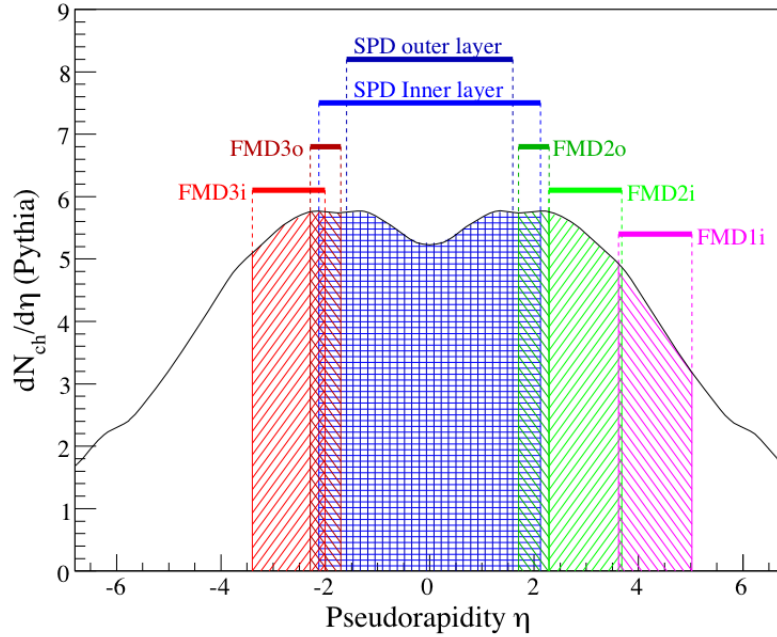


Figure 2.4: The Pseudorapidity coverage of some of the ALICE detectors [51]

The coordinate system in ALICE is referred to throughout this chapter to describe the layout of the detector systems. The  $z$  coordinate follows the beam line of the LHC, with  $z = 0$  at the centre of the detector, also known as the interaction point, or nominal interaction point. The  $x$  axis points towards the centre of the LHC ring, and the  $y$  axis points straight up. Each side of the detector along the  $z$  axis is noted as the ‘A’ and ‘C’ side, indicating beams incoming from the LHC in an anti-clockwise and clockwise direction respectively. The muon spectrometer is on the ‘C’ side of the experiment.

### 2.2.1 Inner Tracking System

The ITS, or Inner-Tracking System [81], is a six-layer silicon vertex detector positioned in close proximity to the interaction point to provide high resolution vertex reconstruction (better than  $100 \mu\text{m}$ ) [82], in order to track and identify particles and reconstruct secondary vertices such as those from decays of charmed hadrons. The detector also improves the momentum and angle resolution of particles tracked by the Time Projection Chamber (TPC) [83], and reconstructs particles that pass through inter-sector gaps, or “dead space”, in the TPC. The layout of the three pairs of detector layers is shown in Figure 2.5.

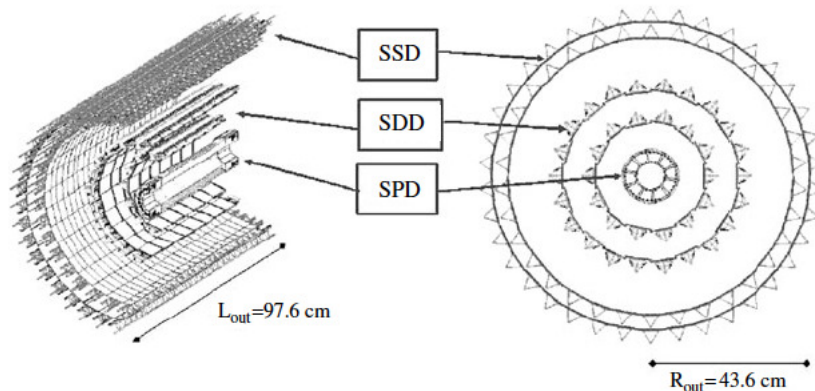


Figure 2.5: Schematic layout of the six layers of the ITS [82]

The ITS has six layers of detectors; two Silicon Pixel Detector layers, two Silicon Drift Detector layers and finally two Silicon Strip Detector layers. It provides rapidity coverage of  $|\eta| < 0.9$  for all vertices located within the length of the interaction region, designed to include at least all the vertices with a  $z$  position  $\pm 1\sigma$  around the nominal interaction point of  $z = 0$ . They are located between 4 cm and 44 cm

from the middle of the beam line, optimally positioned to be as close to the beam line and to match tracks found by the ITS to the tracks found by the TPC.

### **Silicon Pixel Detector (SPD)**

The SPD [81] is designed to determine the primary vertex position and impact parameter of secondary tracks from weak decays of charmed hadrons. It can cope with a particle density of  $80\text{ cm}^{-2}$  [82] in the inner layer, though in reality is subjected to up to  $16\text{ cm}^{-2}$  [79]. It uses pixels to take measurements of charged particle multiplicities. Short tracks, or “tracklets”, can be constructed from two hits in each layer of pixels.

The two layers of the SPD have around  $10^7$  channels with one-bit information, corresponding to an individual pixel and whether it has been hit or not. Each pixel is a silicon diode which is reverse biased to increase the depletion region across the diode junction, and to obstruct the flow of current with high resistance. Ionizing radiation, in this case a charged particle, will activate a pixel by creating electron-hole pairs in the depleted zone which are attracted to either side of the junction and collected by electrodes to generate a signal. The layers present a small thickness to traversing particles, around 1% of a radiation length, in the active regions, allowing the  $p_T$  cut-off for low momentum particle measurements to be  $100\text{ MeV}/c$ .

The pixels are arranged on chips in cells with 8192 pixels each. Each pixel is  $50\text{ }\mu\text{m}$  in  $r\phi$  and  $425\text{ }\mu\text{m}$  in  $z$ . Each chip has an active area of  $12.8$  by  $70.7\text{ mm}^2$ . There are

1200 chips in total, 400 on the inner layer and 800 on the outer layer. To provide a fast minimum-bias interaction trigger, each chip outputs whether it has had a pixel hit or not, instead of querying all  $10^7$  pixels.

### **Silicon Drift Detector (SDD)**

The two intermediate layers of the ITS are occupied by the Silicon Drift Detectors, (SDD) [81], another two-dimensional readout detector to cope with the high particle density even at the radii of these two layers (14.9 cm and 23.8 cm from the beam axis). The SDD has an active area of  $1.31 \text{ m}^2$ , with modules arranged alternately closer and further from its mounting frame to create overlaps of the active areas.

Each detector unit is made of a high purity silicon bulk of  $70.2 \times 75.3 \text{ mm}^2$  in area,  $300 \mu\text{m}$  thick, with cathodes laid along the top layer. The electric field generated by these cathodes creates a drift region that directs electrons to the outer edges of the cell, where anodes collect the charge created by the charged particle ionising the silicon. There are 84 and 176 of these modules in the inner and outer layer respectively.

Like gaseous detectors, the SDD exploits the drift time, up to  $5.4 \mu\text{s}$ , of the deposited charge from the traversing particles to localise the impact point in one dimension, enhancing resolution and multi-track capability. The  $z$  coordinate of the hit is found from the time taken for the electrons to reach the anode collection wires. The  $r\phi$  coordinate is found from which anode wire collects the charge, as there are many

anode wires at the edge of each detector cell.

### **Silicon Strip Detector (SSD)**

The SSD [81] occupies the outer two layers of the ITS at radii of 38.1 cm and 43.1 cm from the beam axis. Both layers are of double-sided silicon strips, and are constructed such that the 768 strips on one side of the layer overlap the 768 of the other at an angle of 35 mrad. Therefore, a hit in two strips gives the position of the hit. They are crucial for connecting tracks from the ITS to the TPC as well as providing  $dE/dx$  information for identifying low momentum particles. It is capable of resolutions of  $20\ \mu\text{m}$  in  $r\phi$  and  $800\ \mu\text{m}$  in  $z$ . There is a compromise made on the  $z$  resolution to give better resolution in  $r\phi$ , which is the direction that particles are bent by the magnetic field of the solenoid, so as to increase the transverse momentum resolution. Combining this information with those from other layers in the ITS provides the  $z$  information.

### **2.2.2 Time Projection Chamber (TPC)**

The Time Projection Chamber, or TPC [83], is the biggest detector of its kind ever built, with a gas volume of  $\sim 85\ \text{m}^3$  and dimensions of 5 m in length, an inner radius of 87 cm and outer radius of 250 cm; giving a rapidity coverage of  $|\eta| < 1.5$ . It is the primary tracking detector in the central region of the ALICE experiment, providing track finding, charged particle momentum measurement, particle identification and

two-track separation for particles with  $p_T \leq 100$  GeV/c and  $|\eta| < 0.9$ .

The cylindrical gaseous volume is split into two halves along the beam direction by a high-voltage electrode with a potential of 100 kV positioned at the axial centre aligned to the nominal interaction point,  $z = 0$ . As shown in Figure 2.6 this gives two drift regions of 2.5 m with a highly uniform electrostatic field of 400 V/cm. This is achieved by encasing the whole drift region in a field cage with electrode strips at intervals around the drift region of decreasing voltage from the central cathode towards the read out plates of the end-caps.

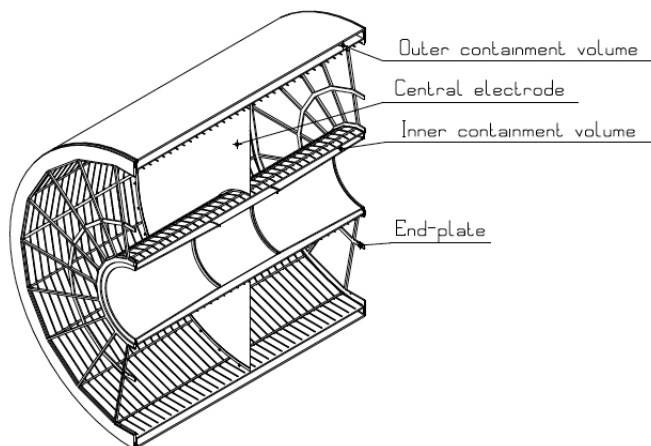


Figure 2.6: Diagram of the TPC field cage, measuring 5 m in length and 2.5 m in radius [83]

The drift gas, a mixture of neon, carbon dioxide and nitrogen (all low-Z gases presenting a small radiation length) at ambient pressure, is optimised to have low diffusion and scattering for electrons while keeping ion mobility high. The maximum drift length is 2.5 m, and the maximum drift time of electrons in this mixture is  $92 \mu\text{s}$ , defining the time during which the TPC is sensitive. Another consideration is to keep effects from ageing minimal, which is minimised by the chosen gas mixture

providing rapid ion evacuation, and to minimise the build up of space charge, a collection of charge grouped in one area of the TPC which takes a long time to dissipate. Space charge is more of a problem for lead-lead collisions rather than proton-proton due to the difference in multiplicity, it is negligible in the latter case, but even at the largest multiplicities it will only affect the tracking by a few mm, correctable after reconstruction.

The end-plates of the TPC, which handle the readout, are segmented into 18 trapezoidal sectors, each segmented radially in two chambers with varying pad sizes optimized for the radial track density, totalling about 560,000 pads. The technology of the read out pads is Multi-Wire Proportional Chambers (MWPC), recording the charge deposited by the drift electrons created from the ionization of the drift gas by the charged particle.

When a charged particle traverses the TPC active area, the gas mixture is ionised, leaving a memory of the path of the particle with a trail of electrons and ions. The electrons drift to the readout plates at the end-caps of the TPC, and the ions drift to the high voltage cathode in the centre of the TPC due to the electrostatic field. The time of arrival of the signal clusters will give the  $z$  position of the hit, and the position of the signal clusters give the  $(r\phi)$  of the hit. These clusters are fitted to reconstruct tracks that have their momentum calculated by the curvature of their path due to the magnetic field. The space-point resolution was found to be around 0.8 mm along the  $z$  direction after 2.5 m drift.

Figure 2.7 shows the track finding efficiency as a function of transverse momentum for just the TPC, and the TPC and ITS together. The efficiency for the TPC and ITS+TPC goes to 90% at very high momenta, a value that is determined by the TPC dead space, that is space which holds support structures or cables. Approximately 10% in azimuth of the TPC is considered dead space, or non-sensitive, as it contains the boundaries between readout pads along with service pipes and cables.

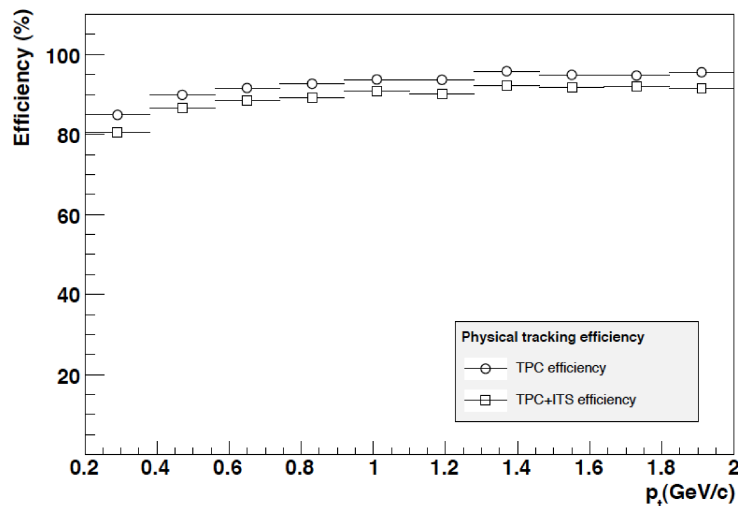


Figure 2.7: Physical track-finding efficiency for just the TPC, and the TPC and ITS combined, as a function of  $p_T$  [51] (modified)

### 2.2.3 Transition Radiation Detector (TRD)

The TRD [51] in ALICE is designed to identify electrons with momenta above 1 GeV/c, taking over from the TPC providing identification below such momenta, as well as providing a high momentum trigger to increase the number of recorded heavy quarkonia such as the  $J/\psi$  and  $\Upsilon$ . Particles first pass through the radiator,

then into the drift chamber filled with a Xe/CO<sub>2</sub> mixture and an accelerating field before reaching the readout pads. The radiator provides a boundary of different dielectric constants for an incident particle to traverse, thus experiencing different electric fields, and if it has a high enough Lorentz factor it will emit transition radiation. The transition radiation of electrons passing through the radiator can be used with the specific energy loss in the drift chamber to reject pions, achieving the desired pion rejection factor of 100 at momenta of 2 GeV/c (that is, only 1% of these pions are erroneously identified as electrons).

A single TRD module is typically 107 mm in depth, and arranged in five stacks of six as a super module. The layering of these cells cumulatively increases the probability of inducing transition radiation from incident particles. The TRD is designed to have 18 of these super modules, arranged outside the TPC with a full azimuthal coverage, and pseudorapidity coverage of  $|\eta| < 0.9$ . At the time of recording the data used in this thesis, 7 modules were installed and operational.

#### **2.2.4 Time of Flight (TOF) Detector**

The TOF [51] identifies charged particles using a time measurement with tracking and momentum information from the inner detectors to assign the particle a mass value. Providing particle identification for pions and kaons with momenta below 2.5 GeV/c and protons up to 4 GeV/c, the TOF can provide  $\pi/K$  and  $K/p$  separation better than  $3\sigma$ . Designed to operate efficiently with low occupancy during

high multiplicity heavy ion collisions, the TOF comprises  $10^5$  independent channels, spread over the large area of the full azimuth surrounding the TRD. The desired particle separation requires a timing resolution of at least 100 ps, provided by the Multi-gap Resistive-Plate Chamber (MRPC) design of the TOF. These chambers are made up of two sets of stacked glass with five gas gaps of a quarter millimetre, with a high voltage applied to the stack giving a uniform electric field. Ionizing particles crossing the gas gaps cause an electron avalanche, due to the applied high voltage, and are collected by the electrodes either side of groups of five gas gaps. Given the thin profile of the chambers (see figure 2.3), there is no drift time associated with avalanche electrons, providing a fast and clear peak well separated from zero time. After testing, the TOF was found to give a resolution better than 50 ps and almost 100% efficiency [84].

### 2.2.5 Electromagnetic Calorimeter (EMCal)

The EMCal [51] is a lead scintillator sampling calorimeter situated on the inside of the ALICE magnet at a radius of 4.5 m, outside the TRD. Constrained by spatial and weight limitations inside the magnet, it covers  $107^\circ$  in azimuth and  $|\eta| < 0.7$  in pseudorapidity. The addition of this calorimeter to the detector array, especially the ability to measure the energy of neutral particles, allows studies of jet physics and efficient triggering on hard jets and photons in all LHC running modes including lead ion collisions. This detector is focussed towards high transverse momenta particles

and jets, so does not require more than modest granularity and resolution.

### **2.2.6 High Momentum Particle Identification Detector (HMPID)**

The HMPID [51] extends the particle identification range in momentum for pions and kaons up to 3 GeV/c and protons up to 5 GeV/c for individual tracks. With it, inclusive particle ratios and transverse momentum spectra can be measured for these particles. Exploiting Cherenkov radiation created from the particle passing through a 15 mm radiator and detected by a Multi-Wire Proportional Chamber (MWPC), the Cherenkov angle can be reconstructed to an accuracy of about 3 mrad per track, assuming 50 particles/m<sup>2</sup>.

### **2.2.7 Photon Spectrometer (PHOS)**

The PHOS [51] is a high resolution electromagnetic spectrometer designed to probe the initial phase of nucleus-nucleus collisions with direct photons, as well as jet quenching through high momenta pion and jet correlations. The high resolution comes from the dense lead-tungstate scintillator crystal that acts as a calorimeter of  $20X_0$  and high photo-electron yield. The discrimination between charged hadrons and photons is made with the Charged Particle Veto layer that lies in front of each calorimeter module. The PHOS is made up of 5 detection modules, in a single arm layout that sits underneath the central barrel at a radius of 460 cm from the

interaction point. It covers the pseudorapidity range  $|\eta| < 0.12$  and an azimuthal arc of  $100^\circ$ .

### 2.2.8 Muon Spectrometer

The Muon Spectrometer [51] arm detects muons in the pseudorapidity range of  $-4.0 < \eta < -2.5$ , or polar angle of  $171^\circ - 178^\circ$ , allowing measurements of quarkonia masses through the dimuon decay channel of quarkonia such as the  $J/\psi$  and  $\Upsilon$  species. It allows also the study of open heavy flavour hadron production, as many muons are produced from the semi-leptonic decay of these states. A passive absorber made from concrete and carbon gives shielding to the spectrometer from hadrons and photons from the interaction vertex, thus filtering out background particles giving a cleaner sample of muons. After the absorber, a set of tracking chambers with a magnet around the middle provides tracking of muons along with a measure of their momenta. These tracking chambers are highly granular to cope with the large flux of muons found in heavy ion collisions. An iron wall 1.2 m thick sits after the tracking chambers, and filters out muons with less than 4 GeV/c of momentum so that the trigger chambers beyond can provide trigger signals picking out heavy quark resonance decays.

### 2.2.9 Zero Degree Calorimeters (ZDC)

The ZDC [51] measures the energy of particles close to the beam line, at almost  $0^\circ$ . This information can be used to determine, in lead-lead collisions, how many nucleons left the collision intact, and therefore its impact parameter. They are 116 m away from the interaction point, and made of two detector types, one to measure neutrons which is placed between the beam pipes, and the other to measure protons that are deflected by the magnetic fields to the side of the beam pipe. They can also give position information about the spectator nucleons, giving a measurement of the reaction plane of the collision. The calorimeters are sheets of tungsten alloy or brass, for neutrons or protons respectively. Quartz fibres are interspersed between these sheets, and give off Cherenkov light when the particle showers from the hadrons hitting the metal sheets pass through them. This light travels along the fibres to be amplified into a measurable signal proportional to the energy of the incoming hadrons.

### 2.2.10 Photon Multiplicity Detector (PMD)

The PMD [85] is a highly granular photon detector covering the phase space of  $2.3 < \eta < 3.5$ , situated 361.5 cm from the interaction vertex, opposite the muon spectrometer. It uses two planes of proportional gas counters either side of a lead converter to measure the shower of photons from the interaction vertex, using the first detector plane as a veto to discriminate against charged particles. It provides

measurements of the photon multiplicity and electromagnetic energy distribution.

### 2.2.11 Forward Multiplicity Detector (FMD)

The FMD [51] measures the charged particle multiplicity in the forward region from the interaction vertex, a polar angle range of  $0.75^\circ - 21^\circ$  or  $1.7 < |\eta| < 5.1$  in pseudorapidity. It is made of 5 discs with silicon semiconductor detectors placed at intervals along the beam pipe around the interaction vertex to provide the wide coverage in small angles around the beam. There are 3 discs on the A-side, a pair of inner and outer discs roughly 80 cm from the interaction point, and another disc 320 cm from it. On the C-side, there is an inner and outer disc 70 cm from the interaction point.

### 2.2.12 V0

The V0 [51] scintillator counters, located either side of the interaction vertex at 340 cm on the opposite side of the muon spectrometer for V0A and 90 cm on the same side for V0C, fulfils many useful roles in ALICE for both proton-proton collisions and heavy-ion collisions. Each of the two detectors is made of 4 rings of 32 scintillator counters, covering the pseudorapidity ranges of  $2.8 < \eta < 5.1$  for V0A and  $-3.7 < \eta < -1.7$  for V0C. The most important function is to provide fast trigger information, it is 84% efficient at triggering on at least one charged particle,

contributing to the minimum bias trigger selection. It can also discern collisions between protons and residual gas in the beam pipe by exploiting the timing information between the two discs to locate the vertex of the event along the beam line. In heavy ion mode, it can provide a centrality trigger, as the number of particles it records correlates with the number of particles produced in the collision.

### **2.2.13 T0**

The T0 [51] provides the live collision start time for the TOF detector with a timing resolution of 50 ps, as well as providing redundancy to the V0 counters and being able to produce minimum bias and centrality triggers. It is made of two arrays of 12 Cherenkov counters, the basic elements of which are PhotoMultiplier Tubes (PMTs) attached to quartz radiators, and they are situated at 375 cm for T0-A opposite the muon arm and 72.7 cm for T0-C in front of the absorber for the muon arm. They cover a pseudorapidity of  $-3.18 < \eta < -2.97$  and  $4.61 < \eta < 4.92$  for T0-C and T0-A respectively.

### **2.2.14 ALICE COsmic Ray DEtector (ACORDE)**

The ACORDE [51], an array of plastic scintillator counters sitting on top of the ALICE magnet, provided triggering of cosmic muons used to align and calibrate central barrel tracking detectors, and detects single and multiple muon events al-

lowing the study of high energy cosmic rays. The array consists of 120 scintillator counters placed in pairs, one over the other, along the top of the ALICE magnet, achieving a 90% efficiency. Atmospheric muons need at least 17 GeV of energy to reach the detector underground, and the TPC can track and measure the momentum of muons up to 2 TeV, defining a wide range of energy in which the ALICE detector can measure cosmic rays with the use of the ACORDE triggering.

### 2.3 Central Trigger Processor (CTP)

The trigger [86] is an electronic decision corresponding to whether an event, seen by the detector, will be read out or not. The CTP manages the triggers in the experiment and is located inside the cavern along with the detector, minimising the latency of signals arising from cable lengths.

The CTP operates by receiving trigger inputs that come from the triggering detectors, which it then processes to make a decision which is passed on as a trigger signal to the Local Triggering Unit of the detectors. The ALICE trigger is designed as a 3-level system, L0, L1 and L2. It can receive three levels of trigger input and can give three levels of trigger signals. This is due to the various speeds of the detectors involved in the decision.

The CTP generates a L0 signal if one or more of the detectors detects a signal that may correspond to a collision having taken place, such as when one pixel in the SPD

has fired. If there are no vetoes on this level, such as when any of the detectors are busy reading out the last event's data, then the CTP sends a L0 trigger signal to the readout detectors, which can begin to digitise the information in their channels. If the event passes additional criteria, then a L1 trigger signal is sent, which tells the detectors to continue processing the event, otherwise it is ignored. The L1 signal also affords more time to calculate more detailed event characteristics on-line, such as whether the event really looks like a jet event (in case one does not care about minimum bias events but specific types of events). After this, a L2a or L2r (accepted or rejected) signal is sent about  $100 \mu\text{s}$  (programmable) after the L0. This corresponds to the drift time of the TPC, being the slowest detector to read out data. This is the final deciding trigger on whether the event information is readout to Data Acquisition.

Some of the detectors dedicated to providing trigger signals are the T0, V0 and ZDC, all placed at forward positions. The T0 is a fast-timing trigger detector, employing Cherenkov detectors to supply trigger signals, as well as an early 'wake-up' signal to the TRD and start time for the TOF. The V0 rejects beam gas interactions using the time-difference between the two asymmetrically positioned scintillator arrays, and contributes to the multiplicity measurement.

The CTP constructs trigger decisions for, often, complex requirements; such as requiring a trigger input signal from a group of trigger detectors to trigger the readout of another group of detectors. An example of this is the minimum-bias

‘OR’ trigger, which requires a hit in either the SPD, or one of the V0 counters, thus creating a larger acceptance in phase space for the trigger than a single detector could achieve. This is implemented through classes and clusters. A trigger class is made of a trigger condition along with a cluster of detectors to respond to this trigger. The trigger condition is a logical function of trigger inputs, for example a combination of trigger inputs from the SPD and V0 can be made to produce a trigger condition.

Another feature of the CTP is the ability to downscale trigger classes, in order to increase the rate of relatively rare triggers, and control the rate of common triggers. This is achieved by setting a percentage of common triggers to be allowed, so the detectors spend less time as busy reading out events, thus allowing the readout of a rare event when it occurs. In this way, rarer events can be collected at a useful rate without compromising the amount of minimum-bias data taken.

The CTP is a crucial part of the data taking effort at ALICE, ensuring through its handling of trigger inputs and outputs that the optimum yield of interesting events are obtained, balancing requirements for different event types and beam parameters. The monitoring of the trigger input rates is accessed through a few methods in the control room, including a streaming readout on a large display, to display the rate of trigger signals on-the-fly. This streaming readout was developed for the control room of ALICE, and can display 3 updating graphs of the rate of L0 and L2 triggers, along with their ratio, for multiple trigger classes. A screenshot of the output during

a data-taking run is shown in Figure 2.8. This allows tuning of the triggers to get the optimum rate of events recorded.

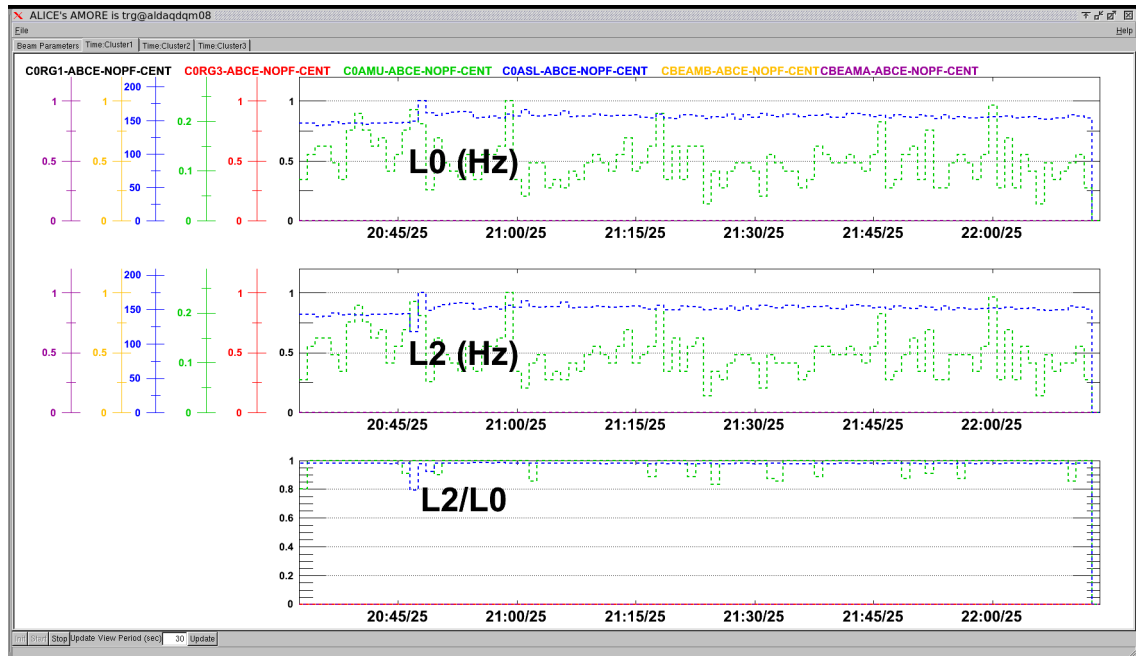


Figure 2.8: A screenshot of the monitoring tool during development, used at the control room of ALICE to display the periodically updated history of trigger rates for a data taking run in 2011.

## 2.4 Data Acquisition (DAQ)

The DAQ [51] controls and manages the flow of data at the ALICE detector during LHC collisions. It is designed to achieve a data storage rate of 1.25 GBytes/s.

After the CTP has issued a positive trigger decision to the detectors, the data is sent by the DAQ system via many hundreds of optical data cables to a computer farm known as Local Data Concentrators (LDC). The LDCs check the integrity of the data and process them into sub-events. Sub-events are passed onto one of 40

Global Data Collector computers to merge them into a whole event. This event is stored by DAQ in one of 20 Global Data Storage servers temporarily, before being archived at CERN where it becomes available for off-line analysis.

## 2.5 High Level Trigger (HLT)

The event data collected by the DAQ can reach a rate of 25 GByte/s. The HLT [51] performs three functions to reduce this rate, while retaining the physics information, for which it collects the detector information in parallel with the DAQ LDC. First, its computer farm performs an on-line reconstruction and analysis to decide if the event is worth keeping. Second, it can read out only part of the detector in which there is interesting information. Lastly, it compresses the data by over an order of magnitude before it is sent to the DAQ to be stored at CERN.

## 2.6 Detector Summary

The ALICE apparatus is a collection of detectors used together to measure the aftermath of hadron collisions produced by the LHC. The central barrel detectors, inside the solenoid magnet, provide tracking and particle identification for particles above transverse momenta of 150 MeV/c, along with fast triggering information and precise vertexing capabilities. The muon spectrometer, with its own dipole

bending magnet, detects muons to study dilepton invariant mass, using an absorber to filter out other particles such as electrons and hadrons. Detectors close to the beam line provide information such as the timing of a collision used with the TOF, and centrality information in lead-lead collisions. The CTP manages the input and output of trigger signals to control what types of events are recorded, with the HLT allowing higher selectivity of interesting data, and the DAQ system managing the flow and storage of data.

---

---

## CHAPTER 3

---

### MULTIPLICITY AND MEAN $P_T$

The multiplicity distribution is a probability distribution to produce a number of particles in a given type of proton-proton interaction, for example inelastic collisions. The data from the ALICE detector is analysed to construct such distributions, subject to fixed selections ensuring data quality. Selections on the spatial acceptance and momentum space of the data are used to create distributions with as much information about the collisions as possible, and for comparison with other results. This analysis requires selections at the level of events and also individual tracks, as well as corrections for triggering and tracking efficiency.

The mean transverse momentum as a function of multiplicity indicates the average momentum of particles produced in the collision according to how many particles were produced. For this analysis, after event and track level selections, an efficiency correction is applied during the mean transverse momentum calculation for each event.

## 3.1 Event Selection

This analysis looks at inelastic proton-proton collision events recorded by ALICE, yet not all of these events can be used. Only events that produce a hardware trigger are recorded. The event sample is reduced further by quality cuts and background rejection, and tuned for the two event types under study; Non-Single Diffractive and Inelastic.

### 3.1.1 Trigger Selection

The CTP, introduced in section 2.2, provides a suite of fast trigger decisions tailored to target specific types of events. The ‘Minimum-Bias’ (MB) triggers target all inelastic proton-proton collisions which produce particles, as long as at least one of the particles is seen by a trigger detector, and apply little biasing toward a subset of these events, hence the name.

The detectors used in the MB triggers are the SPD and the two V0 detectors. The

three fast L0 signals produced by these detectors are interpreted by the CTP to give trigger decisions, and an event is recorded if any of the three detectors produces a trigger signal. These three signals are recorded in the event data, and used off-line to provide further selections of event types.

The two triggers used in this analysis are

**MBOR:** (VOOR or SPDOR) and  $\overline{\text{VOBG}}$ ,

and

**MBAND:** VOAND and SPDOR and  $\overline{\text{VOBG}}$ ,

where VOOR is a hit in either V0 detector, VOAND is a hit in both, SPDOR is a hit in any pixel of the SPD, VOBG signals a beam-gas collision identified by the time difference of two hits in each of the V0 detectors, and a bar over the trigger name means no signal registered in that trigger.

The MBOR trigger provides the least possible bias in selecting inelastic collision events, allowing a hit in any of the three detectors to satisfy its requirements. For this reason, this is the trigger condition used when selecting events for analyses studying inelastic collisions.

The MBAND trigger has a more restricted acceptance, designed to exclude single diffractive events that tend to produce particles in one side of the detector and

none in the other. The requirement that both V0 detectors register a hit biases against single diffractive events, thus providing an optimum choice for a non single diffractive analysis.

The efficiencies of these triggers at selecting events with different processes are shown in Table 3.1 for all the 3 collision energies used. These efficiencies were calculated using detailed simulations of the ALICE detector that match its status during data taking. The two models, Pythia [30] and Phojet [31], differ mostly in their predictions of double-diffractive events, but agree on the suppression of the single diffractive events by the MBAND trigger, especially at higher collision energies. This justifies the use of the more restrictive trigger in selecting Non-Single-diffractive events, even though the overall efficiency for this class is between 85% and 95%. The fraction of diffractive and non-diffractive events, as well as the inelastic cross section, is shown for the three collision energies in Table 3.2.

### 3.1.2 Vertex Selection

The Interaction Point (IP) of an event is where the hadron collision took place. It is referred to here as the ‘vertex’ of the event, though there can be many vertices. Multiple collisions in the same event, known as ‘pileup’, have multiple vertices, and the decay of heavy particles produced in the collision also have vertices with charged particles emanating from them. The vertex of the collision between the LHC hadrons is called the ‘primary’ vertex, secondary vertices refer to weak decays. The choice of

Table 3.1: Trigger efficiencies in percent for the MBOR and MBAND triggers in selecting events with given processes

MBOR						
	900 GeV		2760 GeV		7000 GeV	
	pythia	phojet	pythia	phojet	pythia	phojet
Non-diffractive (ND)	99.96	99.98	99.89	99.97	99.81	99.94
Single-diffractive (SD)	59.94	59.49	43.80	41.64	32.99	31.08
Double-diffractive (DD)	91.61	97.82	88.75	95.66	87.01	93.94
Non-Single-diffractive (NSD)	98.97	99.69	98.25	99.65	98.42	99.35
Inelastic (INEL)	91.37	90.28	91.02	86.13	86.73	83.56
MBAND						
	900 GeV		2760 GeV		7000 GeV	
	pythia	phojet	pythia	phojet	pythia	phojet
Non-diffractive (ND)	95.42	97.97	95.42	97.91	95.17	97.49
Single-diffractive (SD)	10.94	10.78	3.61	2.70	0.947	0.606
Double-diffractive (DD)	34.43	64.90	35.70	90.72	37.89	59.07
Non-Single-diffractive (NSD)	88.25	93.52	86.62	95.18	88.92	93.73
Inelastic (INEL)	73.19	74.15	75.59	73.63	73.21	72.19

Table 3.2: Inelastic cross section for proton-proton collisions with  $\sqrt{s}$  of 900 GeV [87], 2760 GeV and 7000 GeV [88], and the fraction of non-, single- and double-diffractive events in generated inelastic events for Pythia and Phojet.

	900 GeV		2760 GeV		7000 GeV	
$\sigma_{INEL}$	$50.3 \pm 0.4 \pm 1.0$ mb		$62.8^{+2.4}_{-4.0} \pm 1.2$ mb		$73.2^{+2.0}_{-4.0} \pm 2.6$ mb	
	pythia	phojet	pythia	phojet	pythia	phojet
ND	71.1%	66.3%	73.9%	71.7%	73.2%	69.4%
SD	19.5%	23.4%	13.3%	23.3%	17.9%	23.1%
DD	9.7%	1.0%	12.8%	5.6%	9.0%	7.5%

the primary vertex in the case of pileup is the vertex with the most contributions, or tracks pointing to it.

The primary vertex of the event is determined with the SPD tracklets (see section 2.2.1). If the  $x$ ,  $y$  and  $z$  coordinates of the vertex cannot be found, usually due to there only being one tracklet available, then the  $z$ -position of the vertex is reconstructed assuming the radial co-ordinates of the vertex are the same as the average radial co-ordinates during that data-taking period.

For this analysis, there is an overall selection of events which have a vertex within 10 cm along the beam axis from the nominal vertex point, the centre of the central barrel detectors. For all three energies analysed, the distribution of the vertex  $z$ -coordinate follows a Gaussian with a sigma of  $\sim 6.2$  cm, and a mean  $< 1.5$  cm, so this selection removes  $\sim 10\%$  of events with a reconstructed vertex.

A further selection is made of the vertex  $z$ -position depending on the pseudorapidity selection of the measurement, as it affects the acceptance of tracks in each detector. The track selection criteria are summarised in Table 3.4. Four pseudorapidity intervals were considered, and the acceptance of primary tracks with regard to the individual track pseudorapidity controls the choice of the  $z$  vertex selection used. Figure 3.1 shows the acceptance of global tracks, using the ITS and TPC detectors together, as a function of pseudorapidity and vertex  $z$  position. A cut is made to show only cells where at least 20% of primary tracks are found. The same is shown for SPD tracklets in Figure 3.2 and, as this shows a tighter acceptance on tracks, it ultimately constricts the vertex ranges used, as the tracklet cluster information is used in the reconstruction of the majority of global tracks.

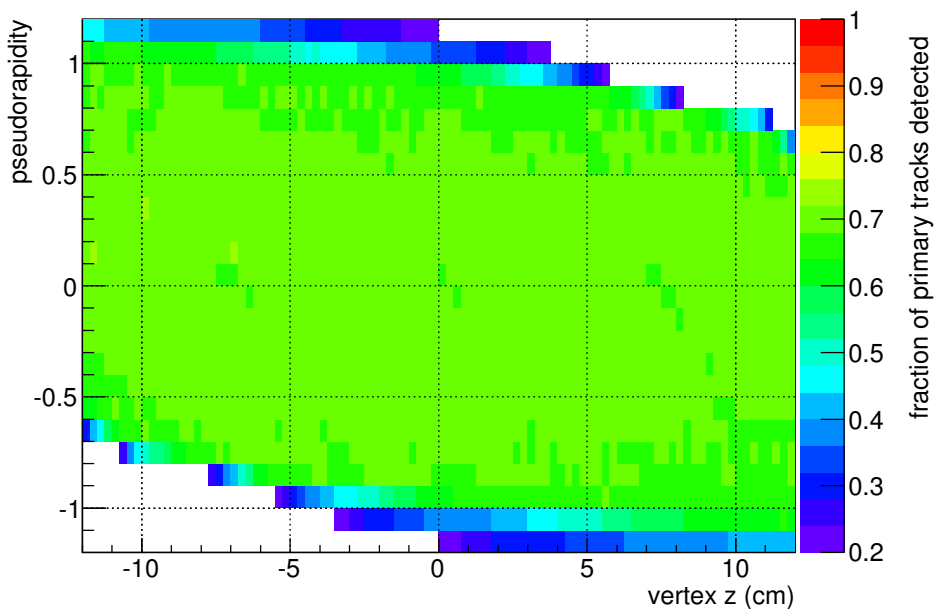


*Figure 3.1: Acceptance of global tracks as a function of pseudorapidity and vertex  $z$  position (cm), cell shading represents the fraction of primary tracks found*

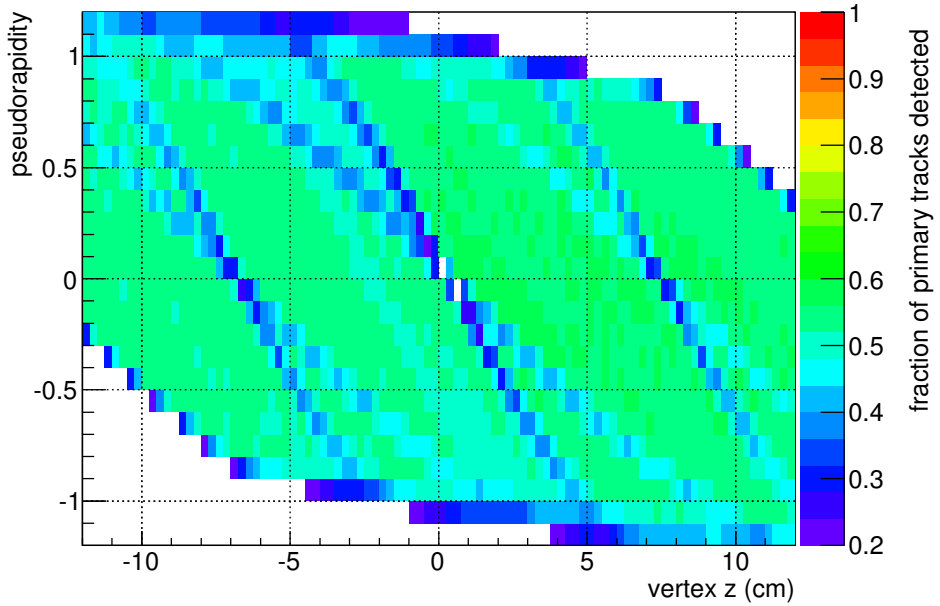


Figure 3.2: Acceptance of SPD tracklets as a function of pseudorapidity and vertex  $z$  position (cm), cell shading represents the fraction of primary tracks found

The vertex  $z$  cuts chosen using these acceptance maps are given in Table 3.3. Also shown are the approximate fraction of events with a good reconstructed vertex kept after the vertex cut is applied, correct for all the data sets used in this study. The tightest cut excludes almost half of the events, but this will not affect significantly the results more than removing the final few bins of multiplicity, which are generally removed anyway due to low statistics. Without this cut, however, a bias towards low multiplicity events would be introduced. Events with a large displacement in  $z$  from the detector centre would have tracks of large pseudorapidity that would be missed, causing an erroneous measure of the event multiplicity.

The edges of the acceptance regions have a lower primary track reconstruction efficiency, so it is prudent to make the vertex cuts slightly tighter than shown in the

Table 3.3: Selection of the primary vertex  $z$  position (cm) depending on the pseudorapidity interval required, along with the approximate fraction of events with a good vertex selected

$ \eta_{\max} $	$ \text{vertex-Z}_{\max} $ (cm)	percentage of events retained (%)
0.5	10	$\sim 92$
0.8	7	$\sim 81$
0.9	5	$\sim 64$
1.0	4	$\sim 51$

acceptance maps. This also reduces the correction applied to the measurement to remove the detector effects and extract the true distribution from it.

The combined efficiency for triggering and vertex construction is shown for the three studied collision energies using Pythia and Phojet generated data in Figure 3.3, as well as including the contamination of the NSD sample with SD events.

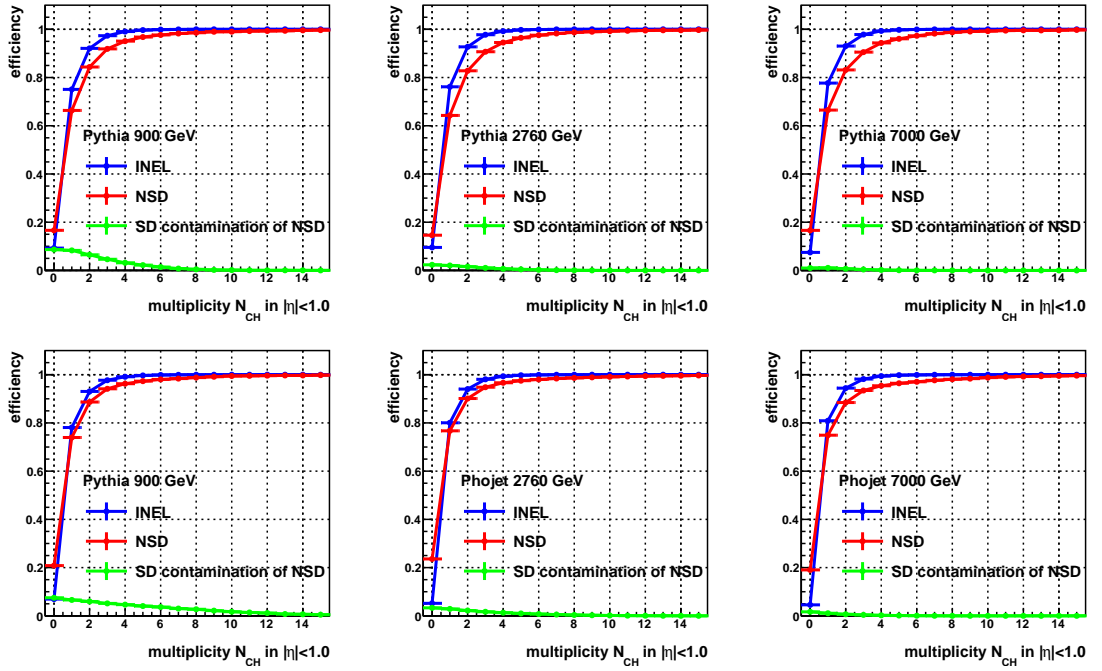


Figure 3.3: Combined triggering and vertexing efficiencies for inelastic and NSD events as a function of charged multiplicity in  $|\eta| < 1.0$ , estimated using Pythia and Phojet generated data at the three studied collision energies. The fraction of SD events included in the NSD selection is shown. The triggers for selecting inelastic and NSD events are ‘MBo’ and ‘MBo’ respectively, described in the text.

## 3.2 Primary Track Selection

After selecting the pseudorapidity interval in which to look for tracks, cuts are applied to the tracks individually to select primary particles. In this study, a primary

particle has the following properties:

- it was produced in the hadron collision,
- it is a product of a strong or electromagnetic decay,
- it is a stable particle.

The first two conditions can be met by requiring the track to come from the primary vertex. This is achieved using a selection on the distance-of-closest-approach (“dca”) of the track to the vertex. It will select particles produced in the hadron collision itself, and discriminate against those produced in secondary (pileup) and material interactions.

This selection will also remove many particles produced in weak decays, also called “feed-down” decays. This is because the time taken for a weak decay is significantly longer than a strong decay, roughly  $10^{-10}$  seconds compared to  $10^{-24}$  seconds, and so a particle that decays weakly will travel on average a few centimetres before decaying. A selection of 2 cm is applied to the z-dca of the track to the vertex, measured along the beam line direction. The radial dca distribution of global tracks with and without SPD hits is shown in Figure 3.4 and Figure 3.5, and displays a strong dependency on the transverse momentum of the track. Therefore, the radial dca selection is transverse momentum dependent, and follows the form of equation 3.1,

$$\text{dca}_{\text{max}} = 0.0182 + \frac{0.035}{P_{\text{T}}^{1.01}}, \quad (3.1)$$

where  $p_T$  is in GeV and  $dca_{\max}$  is in  $cm$ .

The tracks reconstructed with hits in the SPD layers have a narrower  $dca$  distribution than the tracks without, as the SPD hits allow a more precise fitting of the track, otherwise the fitting extrapolates further. To account for this, the  $dca$  cut is widened by 50% for tracks without hits in the SPD, shown in Figure 3.5 as the black line.

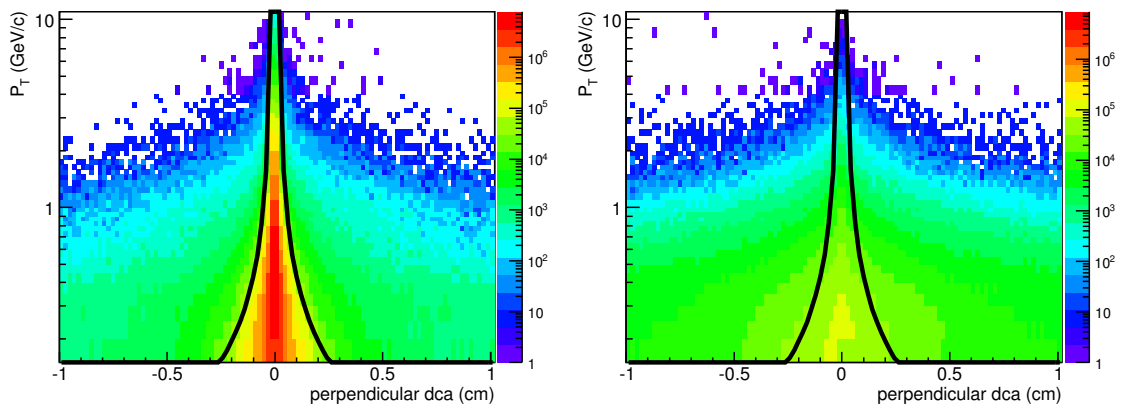


Figure 3.4: The perpendicular  $dca$  distribution ( $x$ -axis) of global tracks with SPD hits as a function of transverse momentum ( $y$ -axis), created from Monte Carlo data. The left hand plot shows primary tracks, the right hand shows secondaries from weak decays and material interactions. The black line shows the  $dca$  cut.

The efficacy of this cut is shown in Figure 3.6, for the transverse momentum range of 150 MeV/ $c$  to 10 GeV/ $c$ . The majority of the primary tracks are selected, approximately 98.4% and 83.1% for tracks with and without SPD hits respectively, to give an overall selection of 96.2% of the primary tracks. The selection also includes 27.9% of the secondaries overall, 32.6% and 19.3% from tracks with and without SPD hits respectively. The  $dca$  distribution of tracks from weak decays follows an approximately exponential distribution that comes from the distance travelled in

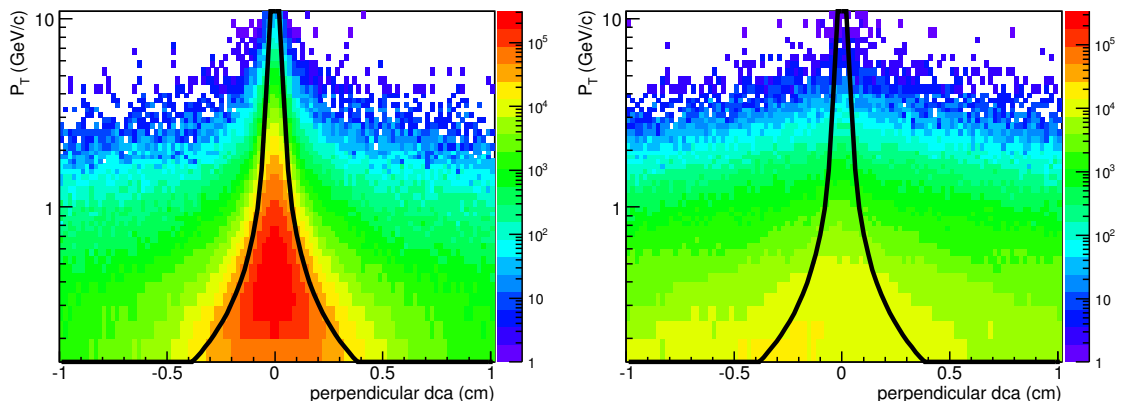


Figure 3.5: The perpendicular dca distribution ( $x$ -axis) of global tracks without SPD hits as a function of transverse momentum ( $y$ -axis), created from Monte Carlo data. The left hand plot shows primary tracks, the right hand shows secondaries from weak decays and material interactions. The black line shows the dca cut.

the mean lifetime of the decaying particle. For the material secondaries, the dca distribution is flat with a broad peak around the vertex. The flatness comes from the random material interactions and gamma conversions, and the broad peak is from particles produced by the collision products interacting with material and getting scattered in the process from the primary particle trajectory. The shape of the primary dca distribution comes from the tracking resolution of the detectors. The tracks without SPD hits have a broader shape due to the lower tracking precision, and the secondaries include tracks produced outside the SPD layers. Primary tracks without SPD hits occur due to inactive modules in the SPD or a poor reconstruction.

The contamination of the sample of primary tracks with secondaries is shown in Figure 3.7, counting tracks with and without SPD hits together. On average, the total contamination is 2.8%, for tracks with transverse momentum above 400 MeV/c

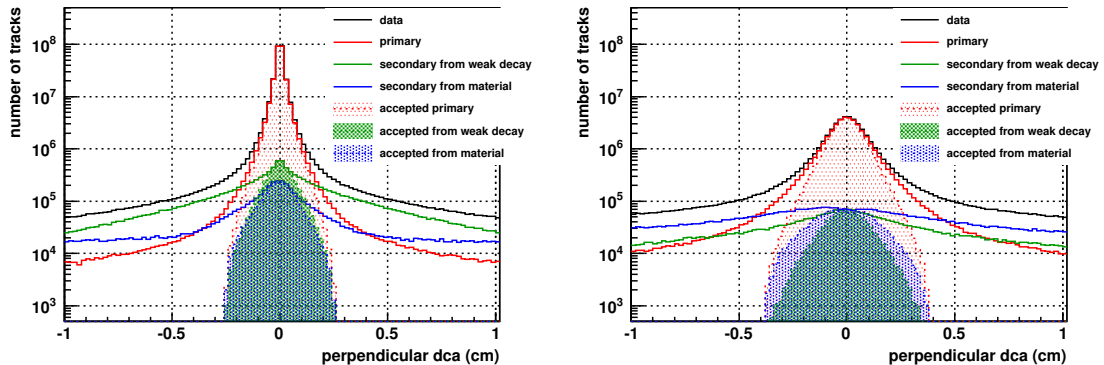


Figure 3.6: Perpendicular dca of tracks to the primary vertex. Left plot shows global tracks with SPD hits, the right plot shows those without. Solid lines represent all tracks of the type specified in the legend, shaded regions represent tracks accepted by the dca cut.

it is less, and at the lowest momenta it reaches a peak of 8%. This level of contamination is not insignificant, but is accounted for in each analysis. In the case of the multiplicity distribution, the unfolding process corrects for acceptance and efficiency effects, as well as background contamination, as shown in section 3.5. For the mean transverse momentum analysis, the effect of the secondaries is included as a systematic error.

### 3.3 Pileup

Pileup is the occurrence of two or more collisions in the same bunch crossing, such that one recorded event contains particles from multiple independent collisions. Clearly, multiple collisions in one event will contaminate analyses and measurements made of multiplicity and mean momentum, so identifying pileup events is important for ensuring a pure sample of events. This is especially important for the multiplicity

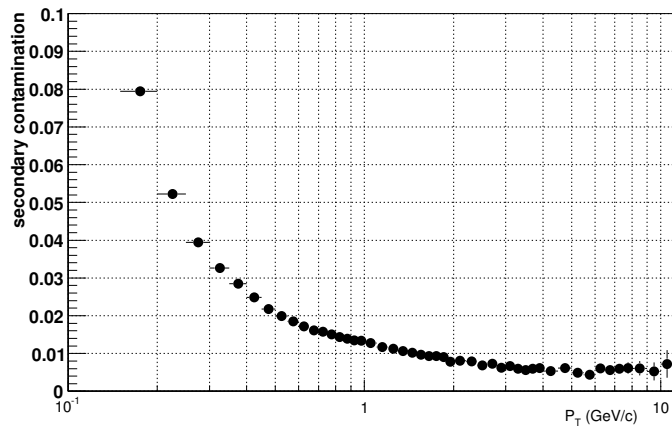


Figure 3.7: Fraction of accepted tracks which are secondaries, as a function of transverse momentum.

analysis, as it will clearly bias the measurement towards higher multiplicity events. After removing events identified as pileup, the effect of the remaining pileup needs to be known; and for this the phenomenon must be modelled accurately.

The number of interactions in an event follows a Poisson distribution [89], as each interaction in an event is a ‘successful trial’ in an unknown large number of trials. Thus, the probability for  $n$  interactions in a bunch crossing is

$$P(\mu, n) = \frac{e^{-\mu} \mu^n}{n!} \quad (3.2)$$

where  $\mu$  is the average number of interactions per bunch crossing.

### 3.3.1 Average Number of Interactions, $\mu$

The average interaction number for a particular run is calculated using the CTP ‘scalars’; counters of the number of fired trigger classes (see section 2.3) which is recorded every minute. The rates of two trigger classes were used for this calculation, “CINT1B” and “CBEAMB”, defined thus:

**CINT1B:** MBor and Beam A and Beam C,

**CBEAMB:** Beam A and Beam C,

where **Beam A/C** indicates the presence of that beam (anti-clockwise or clockwise beam) during the bunch crossing. Thus, **CBEAMB** indicates both beams present during a bunch crossing, meaning a collision between protons from each beam can happen, and **CINT1B** indicates that an interaction was detected while both beams were present.

Simply dividing the number of interaction triggers (**CINT1B**) by the number of bunch crossings with both beams present (**CBEAMB**) gives the probability of at least 1 interaction, which is equal to  $1 - e^{-\mu}$ , or 1 minus the probability of no interaction occurring. To account for background noise, such as triggers from cosmic rays, beam-gas collisions and shower particles from the collimators, the rate of interaction triggers when there is one or no beams present is used to correct the number of **CINT1B** triggers.

Therefore, the average number of interactions per bunch crossing with both beams present is

$$\mu = \ln(\text{CBEAMB}) - \ln(\text{CBEAMB} - \text{CINT1B}_{\text{corrected}}), \quad (3.3)$$

where  $\text{CINT1B}_{\text{corrected}}$  is the interaction trigger count corrected for background sources [90].

### 3.3.2 Pileup Simulation

Using the Poisson description of pileup, the contribution of multiple collision events to the multiplicity distribution can be predicted, given the average number of interactions is known (using equation 3.3), and the multiplicity distribution for single collision events is known. The single event distribution cannot be directly measured, as there is always the chance of pileup in the measured data, but an approximation can be taken by using data recorded with a lower than average interaction rate. In this instance, the pileup is simulated for data with an average number of interactions of 0.061, and the approximately single event distribution uses data with  $\mu < 0.028$ . It must be taken from data, rather than Monte Carlo simulations, to ensure the right shape for the distribution.

Treating the single collision event distribution as a probability distribution, random samples are taken to create the multiplicity distributions for n-interaction events. For events with more than 1 interaction, the measured multiplicity will depend on

the restrictions on counting primary tracks. Firstly, the interaction with the largest multiplicity is assigned to be the primary interaction, as the vertex is found with greater precision, so the other interactions will be the pileup interactions. Secondly, only tracks within a  $z$ -coordinate cut of 2 cm about the primary vertex are counted, so tracks from pileup interactions that fall within this window are also counted. The  $z$ -dca distribution of reconstructed tracks is shown in Figure 3.8.

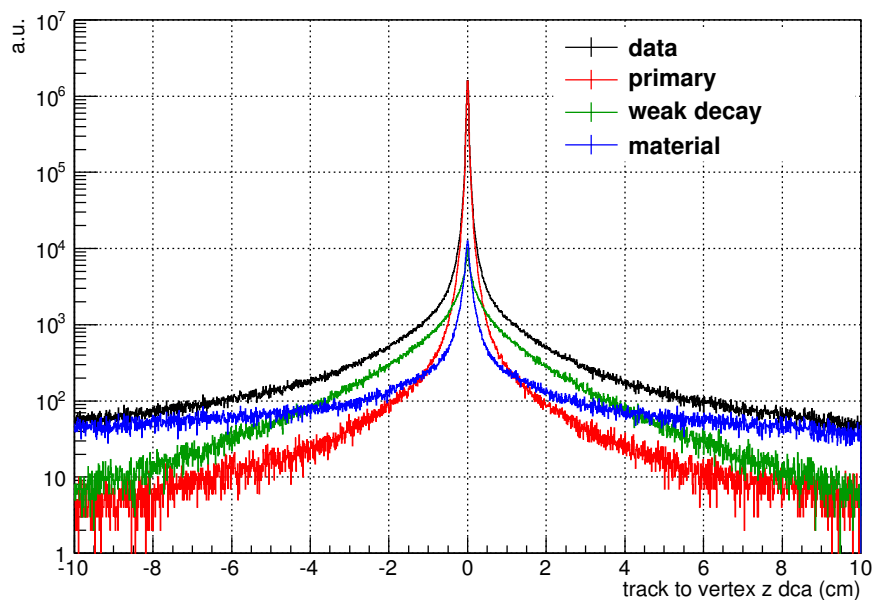


Figure 3.8:  $z$ -dca of tracks to the primary vertex, showing contributions from primary particles, secondaries from weak decay and from material interactions

Though there is also a momentum-dependent radial dca cut of tracks to the vertex, it is assumed in this simulation that the multiplicity in the probability distribution only contains tracks within this dca cut.

Incorporating the effects of how multiplicity is measured into the simulation, the distributions for events with multiple interactions are created using  $10^8$  random

events from the single event probability distribution, and scaled according to the interaction probability. The multiple interaction distributions simply need to be scaled relative to the single interaction shape, using equation 3.4;

$$A(n) = \frac{N_{single} P(n)}{N_{event} P(1)} = \frac{N_{single} \mu^{n-1}}{N_{event} n!}, \quad (3.4)$$

where  $N_{single}$  is the integral of the single interaction distribution, and  $N_{sample}$  is the number of samples used to simulate the multiple interaction distributions.

Figure 3.9 shows the relative abundances of events with different number of interactions as a function of multiplicity, simulated using the parameters of the 7 TeV data, which has the largest interaction probability, and largest reach in multiplicity.

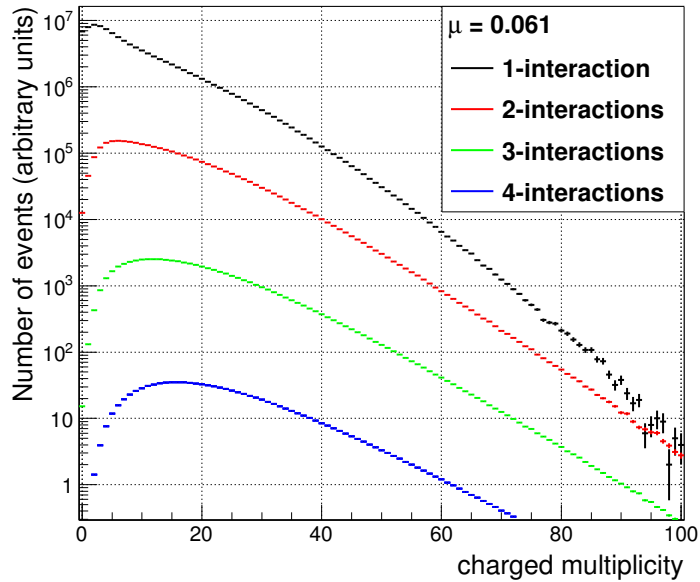


Figure 3.9: Relative abundances of  $n$ -interaction events, scaled assuming the 7 TeV data interaction probability per bunch crossing ( $\mu$ ) of 0.061, using a small sample of this data at lower  $\mu$  to serve as the ‘single’ distribution.

### 3.3.3 Discoverable Pileup

The pileup detection algorithm used during data analysis has two control parameters: the minimum separation between collision vertices in  $z$  and the minimum number of tracks associated to the vertices. Studies [91] show that the best performance of the pileup tagger is found requiring a minimum  $z$  separation between vertices of 0.8 cm, and  $\geq 4$  contributors to each vertex. This makes false positives a negligible occurrence (roughly 0.1%), whereas using  $\geq 3$  contributors gives  $\sim 1\%$  false positives, and  $\geq 2$  contributors has up to 10% false positives.

Given the optimal vertex  $z$  separation threshold, one can see how much pileup is discoverable, purely due to the vertex positions. The vertex  $z$  distribution is very well described by a Gaussian curve, and the typical sigma, or standard deviation about the mean, for the data used in this analysis is  $\sim 6.2$  cm. From Figure 3.10, using the vertex distribution from the 7 TeV data to simulate pileup events with 2 and 3 interactions, the fraction of pileup events with a  $z$  vertex separation less than 0.8 cm is  $\sim 8\%$ , assuming an interaction probability of 0.061 per bunch crossing, the highest of all three data sets. For the triple interaction events, using either the minimum or maximum  $z$ -separation as the  $z$ -separation for that event had a negligible effect on the fraction of events below threshold, as the interaction probability means triple interaction events contribute approximately 0.06% to the data sample.

Using the suggested parameters, the pileup tagging algorithm was found to have an efficiency of 40 – 60% [91] for pileup events with a  $z$  separation  $> 0.8$  cm, so a

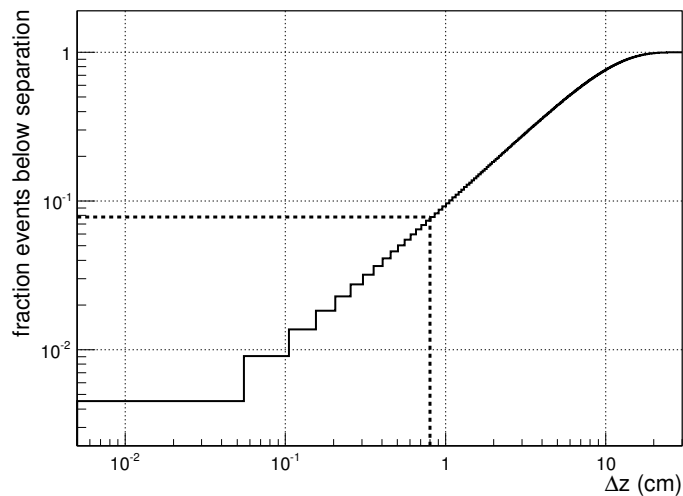


Figure 3.10: Fraction of pileup events (double and triple interaction) with less than the largest separation in vertex  $z$  position (cm). Dotted line shows fraction of events with  $z$  separation less than 0.8 cm.

factor of 0.5 is applied in the model to the findable pileup to simulate the pileup tagging. It should also be noted that the  $z$ -dca cut for primary tracks results in 81% of pileup events not being affected by tracks from pileup, given the  $z$ -vertex distribution and  $z$ -dca distributions described previously. From this model, for the 7 TeV data, it is seen that 34% of all pileup would be identified, only counting events as pileup if the observed multiplicity is affected by tracks from the pileup interactions. Figure 3.11 shows the model predicted performance of the pileup tagger at reducing the abundance of pileup in the multiplicity distribution for 7 TeV, using tracks in  $|\eta| < 1.0$ . Above a multiplicity of  $\sim 80$ , fluctuations due to low statistics become apparent, but are smoothed over by averaging multiple bins, and the trend can still be interpreted to show that at about a multiplicity of 90, the pileup (predicted to be 25%) is reduced to 15%.

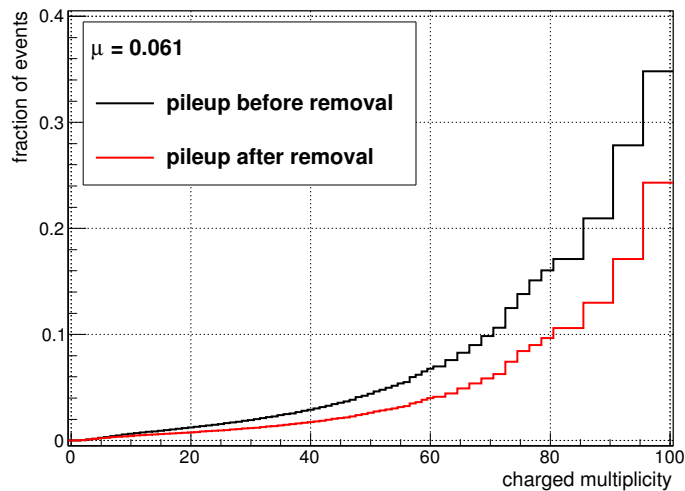


Figure 3.11: Fraction of pileup per multiplicity bin, from pileup simulation of 7 TeV data, before and after removal of tagged pileup events.

To compare this prediction with the pileup tagging effect on data, the ratio of the multiplicity distributions before and after tagged pileup is removed is compared in Figure 3.12. It shows good agreement up to multiplicities of 50, above which the predicted change is larger than seen in data. This is most likely due to the tagging efficiency having a multiplicity dependence, which was not studied, or uncertainty in this efficiency depending on the generator model used. However, the difference is less than 10% at the highest multiplicities, and this will be incorporated into the systematic uncertainty of the multiplicity distribution before deconvolution.

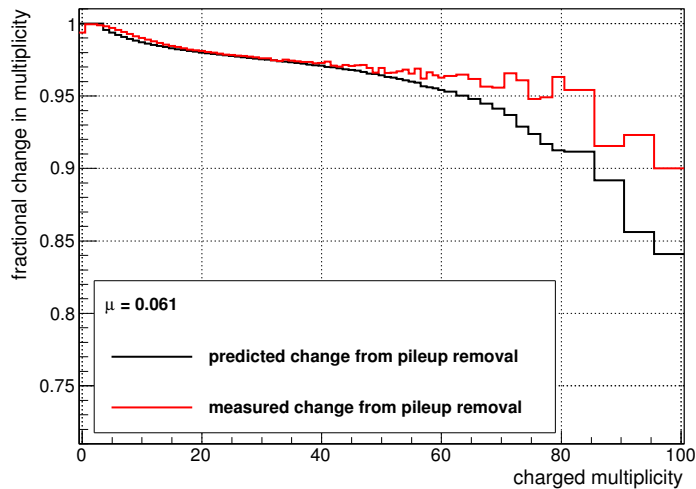


Figure 3.12: Ratio of multiplicity distributions before and after pileup removal, from pileup model (black) and from 7 TeV data (red).

### 3.4 Multiplicity Counting

The detectors used to provide tracks in this analysis are the ITS and TPC. They can each find tracks of their own, the ITS is able to construct “tracklets” from two hits in the SPD layers, as well as “ITS-standalone” tracks from all six layers including the SPD (called standalone as it ignores all other detectors apart from the ITS). The optimal tracking efficiency comes from combining all the detector information together, either by tracking one particle through both detectors, or each detector tracking particles the other does not detect.

The analysis framework provides access to different groups of tracks according to which detectors they are from. The broadest category is the “global” track, which uses as many detectors as possible to construct each track, normally this means at

least the TPC is used, usually along with the ITS. Particles not detected by the TPC but by the ITS are reconstructed as “ITS-complimentary” tracks.

For a track to be considered in this analysis, it must satisfy criteria ensuring it is of good quality and is a primary track. Each type of track mentioned above has different criteria, shown in Table 3.4, and the ITS-complimentary tracks use the same criteria as the global tracks while ignoring the TPC specific criteria. The dca requirements refer to the distance of closest approach of the track to the primary vertex, and a kink daughter is a particle that has decayed and its track has a kink in it.

An algorithm was developed to construct a multiplicity measure using the four types of tracks mentioned above, within a specified pseudorapidity interval. It is split into two loops, the first over all tracks except the SPD tracklets, and the second over the tracklets.

In the first loop, the tracks are selected for quality of reconstruction (different requirements for each track type) and primary track selection. Tracks that fail the primary track requirements are labelled as “secondary”, and those that fail the quality requirements are labelled as “rejected”. The selected global and ITS-complimentary tracks are grouped together to make one multiplicity measure, as they are mutually exclusive and therefore can be summed without double counting. At this point, before the tracklets are counted, there are two multiplicity measures called “ITSSA”

*Table 3.4: Quality criteria for different types of tracks to be accepted as primary tracks.*

Global	<p>Number of TPC clusters <math>&gt; 70</math></p> <p><math>\chi^2</math> per TPC cluster <math>&lt; 4</math></p> <p>Not a kink daughter</p> <p>Successful ITS and TPC refit during reconstruction</p> <p><math>dca_z &lt; 2</math> cm</p> <p><math>dca_{xy}</math>(with SPD clusters) <math>&lt; 0.0182 + \frac{0.035}{p_T^{1.01}}</math></p> <p><math>dca_{xy}</math>(without SPD clusters) <math>&lt; 1.5 \times \left( 0.0182 + \frac{0.035}{p_T^{1.01}} \right)</math></p>
ITS-standalone	<p>Successful ITS refit during reconstruction</p> <p>Not a kink daughter</p> <p><math>dca_z &lt; 2</math> cm</p> <p><math>dca_{xy}</math>(with SPD clusters) <math>&lt; 0.0182 + \frac{0.035}{p_T^{1.01}}</math></p> <p><math>dca_{xy}</math>(without SPD clusters) <math>&lt; 1.5 \times \left( 0.0182 + \frac{0.035}{p_T^{1.01}} \right)</math></p>
SPD tracklet	Two hits in the SPD layers pointing towards the primary vertex

and “ITSTPC”. The latter measure is clearly the measure of choice as long as the TPC is used, which for the data used in this thesis is always the case.

The second loop over the tracklets first checks whether the tracks are associated to any tracklet, in that the track and tracklet are deemed to be from one particle. If this is the case, tracklets associated to “secondary” tracks are ignored, and those associated to “rejected” tracks are counted. Then all the un-associated tracklets within the pseudorapidity range are also counted to complete the multiplicity measure. This is done for both the ITS-standalone tracks and the group of global and ITS-complimentary tracks to give two more multiplicity measures, “ITSSA+” and “ITSTPC+”. These measures give an even better account of the event multiplicity, but the caveat is that with the SPD, there is no possible  $p_T$  selection, and so the measure will always have tracks with  $p_T$  as low as 50 MeV/c included.

Thus, for the multiplicity measurement for all  $p_T$ , the ITSTPC+ counting method is used, and for multiplicity measurements with a minimum  $p_T$  threshold, the ITSTPC method is used.

Figure 3.13 shows the correlation of measured and true multiplicity according to the Pythia generator for the two counting methods of tracks with the respective  $p_T$  cut.

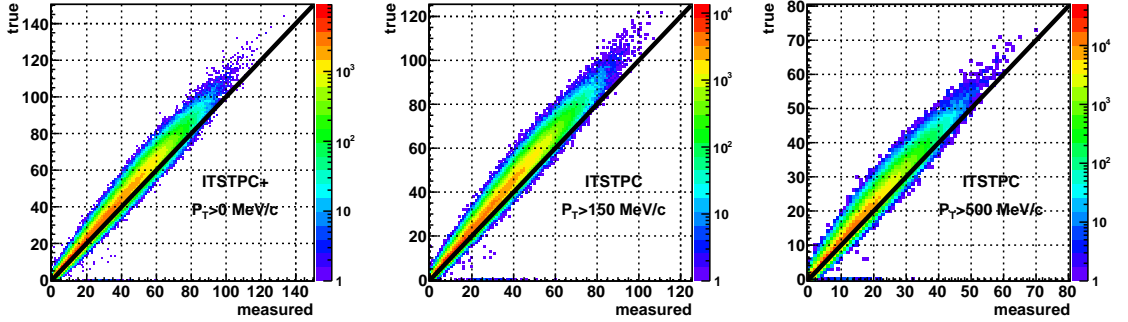


Figure 3.13: The correlation of measured multiplicity with the true multiplicity according to Pythia generated data at  $\sqrt{s} = 7000$  GeV and in the interval  $|\eta| < 1.0$ . Lines are drawn to show where the true multiplicity equals the measured multiplicity. (Left) ITSTPC+ measurement (includes SPD tracklets) for tracks with  $p_T > 0$  MeV/c. (Centre) ITSTPC measurement (without SPD tracklets) for tracks with  $p_T > 150$  MeV/c. (Right) ITSTPC measurement (without SPD tracklets) for tracks with  $p_T > 500$  MeV/c.

### 3.5 Unfolding the Multiplicity Distribution

The measurements made of event multiplicities from proton-proton collisions do not give the exact value of the observable, the true multiplicity. A collision event with a given multiplicity, a “cause”, is picked up by the detector as a measured multiplicity, an “effect”, which typically has a spread of values, as shown in Figure 3.14.

The relationship between cause and effect can be represented as a detector “response” matrix, using a detailed simulation of the detector with an event generator to provide the matrix cell contents, as shown in Figure 3.15.

In this way, the measurement of the multiplicity with the detector described by the response matrix can be represented as the matrix equation 3.5, where  $m$  is the measured distribution,  $R$  is the response matrix and  $g$  is the generated, or true,

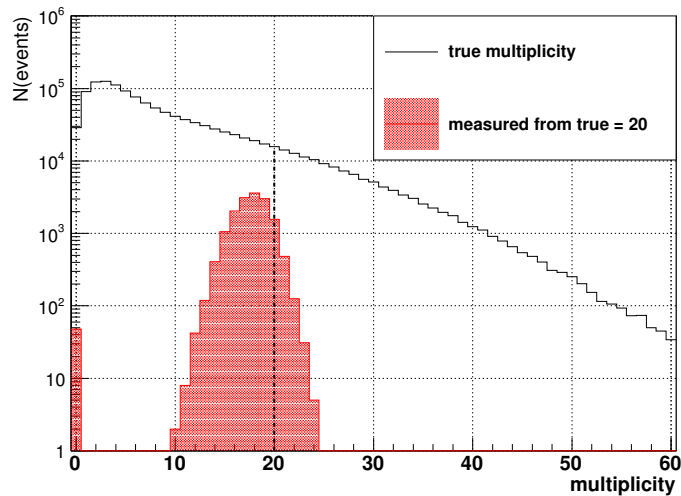


Figure 3.14: A generated multiplicity distribution (black) and the measured multiplicity distribution from events with true multiplicity of 20 (red), using Pythia simulated 7 TeV data.

distribution;

$$m_i = \sum_j R_{ij} g_j. \quad (3.5)$$

The problem is how to obtain the generated distribution, given the measured distribution and the detector response. The solution is known as deconvolution; the process of unravelling the effects of a matrix on a vector.

### 3.5.1 Naive Solution

The simplest approach to correct the measured distribution for detectors would be to use bin-by-bin correction factors, calculated using the true and measured vectors of a Monte Carlo event simulation. However, this approach only works if there is no bin migration, it can only correct the effects of efficiency of event detection, and it

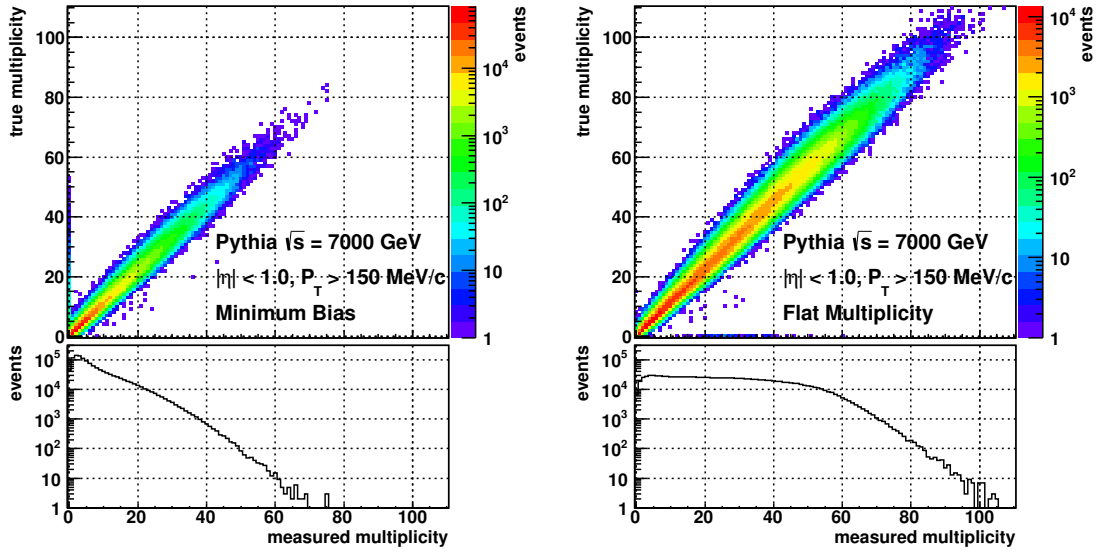


Figure 3.15: Response matrices on the top rows built using ITSTPC tracks from  $\sqrt{s} = 7$  TeV Pythia generated data, with the projected measured multiplicity underneath. The left matrix is generated from a physically motivated, unaltered (“Minimum Bias”) multiplicity distribution. The right matrix is made from an artificially populated “flat” distribution, which extends to higher multiplicity with a similar overall population to the minimum bias matrix.

also biases towards the model of the event generator.

From the form of equation 3.5, one may naively re-arrange the formula to obtain a direct solution, essentially inverting the response matrix to get equation 3.6;

$$g = R^{-1}m. \quad (3.6)$$

Though technically this is an exact solution, it only works if applied to the convoluted distribution from the response matrix. Another measured distribution which is statistically independent of the response matrix will yield a nonsensical result with large fluctuations; the bin-to-bin differences are amplified by the inverse matrix. The fluctuating result is technically correct, in that when operated on by the response

### 3.5. UNFOLDING THE MULTIPLICITY DISTRIBUTION

matrix it will produce the measured distribution, but the huge differences between adjacent bins destroys the overall shape of the distribution, as shown in Figure 3.16.

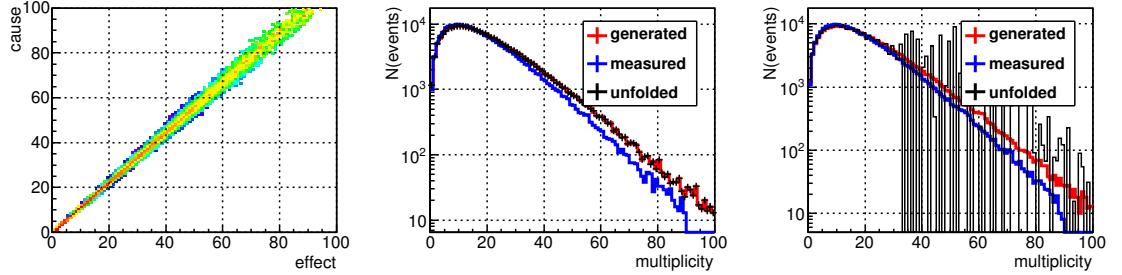


Figure 3.16: (Left) A response matrix generated from a negative binomial probability density function as the “cause” and multiplicity dependent efficiency and smearing for the “effect”. (Centre) Using the measured distribution from the response matrix with the inverse matrix, the unfolded distribution matches the truth perfectly. (Right) Creating a new randomly sampled truth from the negative binomial pdf, and a new measured distribution, the result is now fluctuating wildly.

This instability, that causes such wild fluctuations when the initial distribution is changed within statistical agreement to that used in the response, comes from the off diagonal elements of the response matrix describing bin migration. This is best described using a simple response matrix, such as equation 3.7, where  $\varepsilon$  is the bin migration factor, taking values between 0 (unit matrix) and up to 0.5 (almost every event is migrated into an adjacent bin).

$$R = \begin{pmatrix} 1 - \varepsilon & \varepsilon & & & \\ \varepsilon & 1 - 2\varepsilon & \varepsilon & & \\ & \varepsilon & 1 - 2\varepsilon & \varepsilon & \\ & & \varepsilon & 1 - \varepsilon & \\ & & & & \varepsilon & 1 - \varepsilon \end{pmatrix} \quad (3.7)$$

For a response with a very strong diagonal ( $\varepsilon$  is close to zero), unfolding with its inverse will likely produce a satisfactory result, but only because such a matrix implies

an almost exactly linear correlation between the true and measured distributions. For matrices that describe an even chance that an event will migrate by only *one* bin, where  $\varepsilon$  approaches 0.5, the negative correlations between bins in the inverted matrix produce the large fluctuations in unfolding distributions only slightly varied from the response matrix measured distribution. For any response matrix, as its determinant gets smaller, or becomes essentially zero, the matrix inversion method of unfolding becomes useless.

What this deconvolution method lacks is the importance of the distribution shape; the correlation between the bins as well as their values. The importance of the distribution shape can be imposed on the unfolding process through regularisation; this analysis examines two unfolding procedures which provide regularisation.

It is also worth noting that the measured distribution requires some treatment before unfolding; the low statistics of the higher multiplicity bins often results in discontinuity of the distribution. Feeding this into an unfolding procedure essentially requires that the solution also has such a discontinuity, introducing fluctuations in the tail of the solution. To avoid this, all high multiplicity bins with an adjacent empty bin of lower multiplicity are removed, as shown in Figure 3.17.

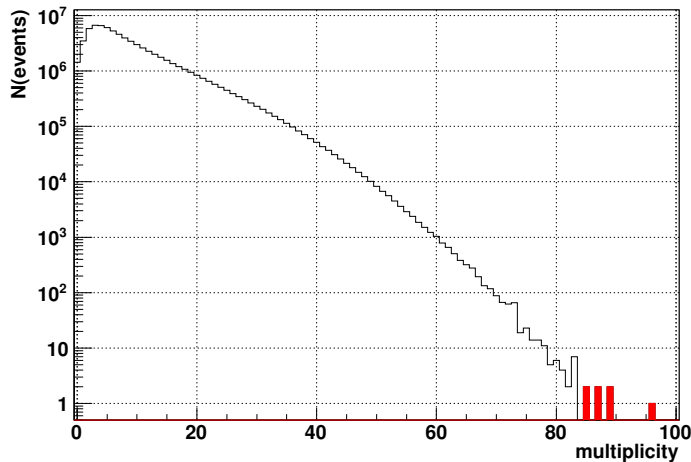


Figure 3.17: Multiplicity distribution from Pythia simulated  $\sqrt{s} = 7$  TeV data, with isolated high multiplicity bins shown in red. These red bins are removed before the distribution is unfolded.

### 3.5.2 Single Value Decomposition Unfolding

Single Value Decomposition (SVD) unfolding, as described in [92] and implemented in the ROOT framework [93], is similar to Tikhonov regularisation, as discussed in [94] and [95], where in minimising the inverse matrix equation, a smoothing term is added containing a Tikhonov matrix, much like the SVD method. It differs, however, by decomposing the response matrix and rotating and rescaling the matrix equation to introduce a weighting to the minimisation, and to expose the singular values of the matrix which is used to decide on the optimal regularisation strength, and thus suppress fluctuations.

The deconvolution can be expressed as a minimisation of the  $\chi^2$  between the mea-

sured vector and the solution folded with the response matrix;

$$(Rg - m)^T M^{-1} (Rg - m) = \min, \quad (3.8)$$

where  $M$  is the covariance matrix of the measured vector  $m$ . This is equivalent to the standard chi-squared test (see equation 3.19).

The solution to this equation can be given by decomposing the response matrix as follows:

$$R = USV^T, \quad (3.9)$$

where  $S$  is a diagonal matrix of the singular values of the response, and  $U$  and  $V$  are orthogonal rotation matrices whose columns are called the left and right singular vectors [92]. The rotation matrices rotate the response into a basis where the singular values are exposed, and back again. This technique allows the straightforward calculation of the pseudo-inverse of the response matrix, as shown in equation 3.10;

$$R^{-1} = VS^{-1}U^T, \quad (3.10)$$

but this is not used at this stage as the regularisation is yet to be applied; it gives the same solution as the inverse response matrix with the same problems detailed in section 3.5.1.

Before the regularisation is applied, the unknowns in the system of linear equations represented by equation 3.8, the vector  $g$  is normalised such that it represents the

deviation from the generated distribution used to populate  $R$ :

$$\omega_i = g_i / g_i^{response} . \quad (3.11)$$

This gives two advantages; first that if the generated vector used in  $R$  is similar to that being unfolded, the normalisation gives a smooth vector requiring fewer terms during the decomposition. The second is that this changes  $R$  from a probability matrix to an event filled matrix, where bins with low population are not considered to have low uncertainty, and bins with larger populations are given more weight: the statistics of the bin defines its uncertainty.

The equations are also rescaled by the uncertainties in the covariance matrix  $M$ , such that the uncertainties are incorporated into the matrix  $R$  (now  $\hat{R}$ ) and the measured vector  $m$  (now  $\hat{m}$ ). This now means the covariance of the rescaled  $\hat{m}$  is the unit matrix  $I$ , and gives all the equations in the system equal weighting.

After these changes, there are still small singular values that will result in unphysical oscillations in an exact solution. A regularisation term is added to the left hand side of equation 3.8 that imposes smoothness by increasing in magnitude for oscillatory solutions. The strength of the regularisation is controlled by a parameter,  $\tau$ . To avoid applying SVD to the system for every value of  $\tau$ , the system is rotated further such that the regularisation term is proportional to the unit matrix  $I$ . This changes the  $\hat{m}$  vector into the  $d$  vector, also with a unit covariance, and allows the solution of the regularised system ( $\tau \neq 0$ ) to be expressed in terms of the unregularised system

( $\tau = 0$ ), avoiding unnecessary SVD operations.

For a non-zero regularisation parameter, the solution can be expressed in terms of the non-regularised system to avoid doing many SVDs:

$$z_i^{(\tau)} = \frac{d_i s_i}{s_i^2 + \tau}, \quad (3.12)$$

where  $z_i^{(\tau)}$  is the rotated regularised solution and  $d_i$  is the rotated version of the measured distribution  $m_i$  [92]. The fraction effectively acts as a low pass filter to suppress the contributions from small valued components of  $\mathbf{s}$ , the vector of singular values.

The choice of  $\tau$  comes from inspecting the distribution of  $\mathbf{d}$ , as the statistically significant values will all be much larger than 1, typically the first  $k$  bins for a very smooth measured distribution. The statistically insignificant ones are all distributed about 1 above bin  $k$ , what with each component of  $\mathbf{d}$  having an uncertainty of 1 due to rescaling based on the errors of the measured data and response matrix. An example of a typical  $d_i$  distribution is shown in Figure 3.18.

From inspecting the  $d_i$  distribution, the critical bin  $k$  can be identified after which the contributions from those linear equations just add noise, and so the regularisation parameter is set to the singular value of that bin,

$$\tau = s_k^2. \quad (3.13)$$

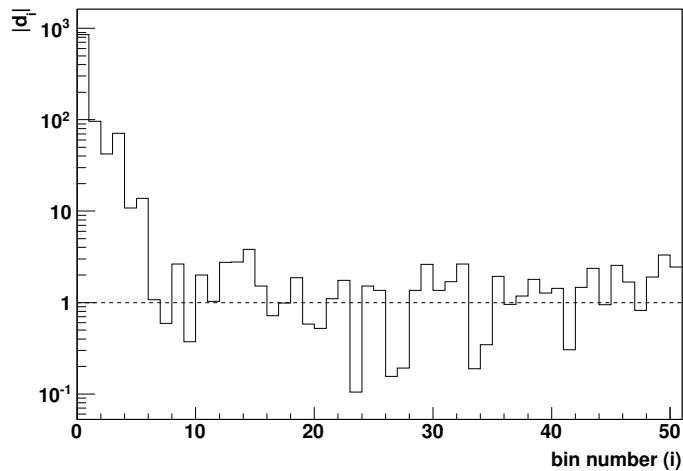


Figure 3.18: The distribution of the rotated  $m$  vector,  $d_i$ , taken from Phojet simulated 7 TeV data, indicating how many bins contribute significantly to the unfolded distribution. In this example, the critical bin  $k$  would be 6.

Without  $\tau$ , this method is effectively producing the inverse response solution complete with unstable oscillations, even after taking into account the uncertainty of the response and measured distributions. Setting  $\tau$  appropriately gives a much more stable solution, as shown in figure 3.19 comparing the SVD solution with and without the regularisation, using a response map filled according to the expected multiplicity distribution; the higher multiplicity area of the response is sparsely populated.

So, in the case of unfolding multiplicity distributions using a response matrix populated according to a physical model of multiplicity, the procedure yields a stable and smooth result, which matches well to the true generated distribution. Filling the response matrix according to the expected multiplicity distribution does mean that it becomes more sparsely populated as multiplicity increases, as it follows a generally inverse exponential shape. This is fine if the response covers the range

### 3.5. UNFOLDING THE MULTIPLICITY DISTRIBUTION

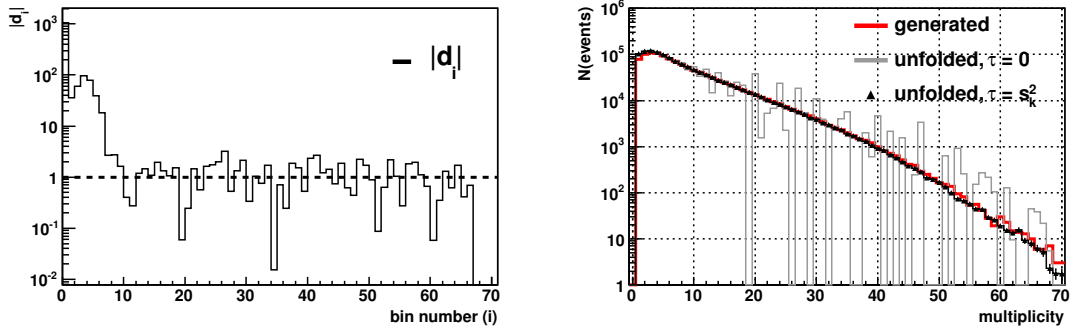


Figure 3.19: (Left) Distribution of rotated measured vector from Pythia simulated 7 TeV data, showing the ideal cut-off bin to be  $\sim 10$ . (Right) The unregularised unfolded distribution (grey line), regularised unfolded distribution (black triangles) and generated distribution (red) from Pythia simulated 7 TeV data and using a Phojet simulated 7 TeV data response map filled with Minimum Bias events.

measured in the data, as is the case in Figure 3.19 where the Phojet measured distribution reaches up to  $\sim 70$  charged particles with  $p_T > 150$  MeV and  $|\eta| < 1.0$  and the Pythia response covers up to the same range. However, the measured data at 7 TeV reaches higher multiplicities than predicted by the models, such that the minimum bias response maps will not be able to unfold the tail of the measured distributions.

This can be overcome by populating the response map at higher multiplicities with more events, requiring the generator to produce an event sample with an approximately flat multiplicity rather than a more physical distribution. Unfolding the test distributions as above with a flat multiplicity map yields results such as Figure 3.20, showing various choices of cut-off bin, but each yielding unsatisfying results. The  $d_i$  distribution, when using the flat multiplicity map, does not behave as expected by the unfolding method; instead of an exponentially falling line which then randomly

fluctuates about 1, there seems to be two decaying shapes of different slope superimposed. Choosing a cut-off bin based on when  $d_i$  becomes statistically insignificant leads to a choice of  $\sim 30$  in this case, but it clearly is not acceptable, containing a large spike at the beginning, a satisfactorily smooth mid multiplicity region and strongly oscillating tail. Smaller cut-off values dampen the higher multiplicity oscillations as expected, but produce a lower multiplicity structure, an indication of over-determining the solution. Clearly, there is no choice of cut-off value which provides an adequate solution over the whole range of multiplicity when using a flat multiplicity response map, a requirement to deal with the high-multiplicity-reaching proton-proton data.

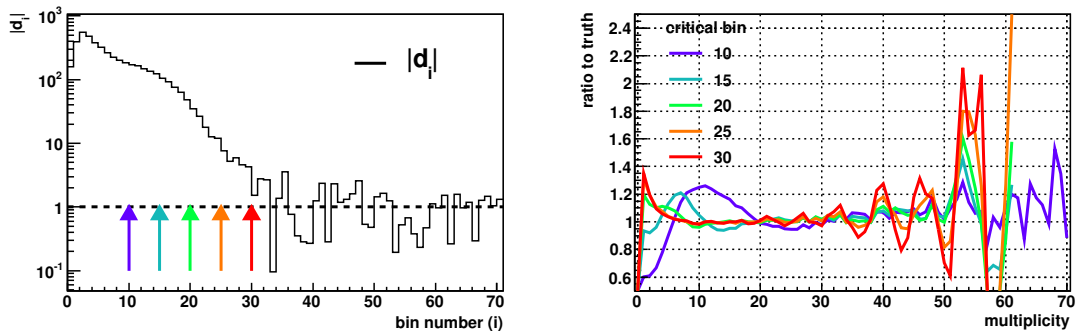


Figure 3.20: (Left) Distribution of rotated measured vector from Pythia simulated 7 TeV data, and response map with artificially increased high multiplicity population, and coloured arrows indicating choices of cutoff bin. (Right) Ratio of unfolded distributions to generated truth using different choices of the cutoff bin, shown in colours.

The failure of this unfolding method, when using a flat multiplicity response map, may be due to the un-physical shape of the response map itself. The events generated to fill it are produced according to an expected multiplicity distribution, giving a low population of high multiplicity events. To populate the higher multiplicity bins,

the simulation then produces events according to a box distribution. This means the response map is filled with two different shapes of multiplicity distribution, which could be causing the instability at either end of the unfolded vector, or more simply the un-physical shape of the response map is imposing itself on the unfolded result. The two shapes could also be applying an unfairly high weight to the high multiplicity area of the response, which is not as well understood by the Monte Carlo programs as the low to medium multiplicity regions.

Thus, a different unfolding method is used.

### 3.5.3 Unfolding Based on Bayes Theorem

An iterative approach to solving the matrix equation 3.5 is presented by D'Agostini [96], and studied by Cowan [95] and Adye [97], based on Bayes theorem [89]. Equation 3.14 shows the theorem for the simple case of two events,  $A$  and  $B$ , where the probability of event  $A$  given that  $B$  has happened is expressed in terms of the probability of  $B$  given  $A$  has happened, and their individual probabilities, i.e.:

$$P(A|B) = \frac{P(B|A)P(A)}{P(B)}. \quad (3.14)$$

The procedure treats the generated and observed distributions as cause and effect, and the response matrix as the probability distributions for each given cause  $g_i$  producing an effect  $m_j$ , where  $\mathbf{g}$  and  $\mathbf{m}$  are vectors of the generated, or true, and

measured distributions respectively. With this notation, Bayes' theorem becomes

$$P(g_i|m) = \frac{P(m|g_i)P(g_i)}{\sum_l P(m|g_l)P(g_l)}, \quad (3.15)$$

where  $P(g_i|m)$  is the probability that given a measurement  $\mathbf{m}$  is made, the  $i$ th element of the generated vector is the cause, the sum in the denominator gives the total probability of measuring  $\mathbf{m}$  (the efficiency of the detector on measuring  $\mathbf{m}$ ), and  $P(g_i)$  is the probability of  $g_i$  occurring.

The probability of the generated events  $P(g_i)$  is the solution sought after, so in practice an initial guess is used in its place,  $P_0(g_i)$ , a best guess of what the result could be or a uniform distribution if none is known.

Thus, for each measurement value  $m_j$ , equation 3.15 can be applied as so;

$$P(g_i|m_j) = \frac{P(m_j|g_i)P_0(g_i)}{\sum_l P(m_j|g_l)P_0(g_l)}, \quad (3.16)$$

where  $P(m_j|g_i)$  is essentially an element of the response matrix after it has been normalised such that each cell represents the probability of a generated event  $g_i$  being the cause of a measurement  $m_j$ . This normalisation is given by;

$$\sum_j P(m_j|g_i) \equiv \epsilon_i \leq 1, \quad (3.17)$$

where  $\epsilon_i$  is the efficiency of measuring an event  $g_i$ . So, this normalisation means that taking all the possible measurement cells for a given generated event gives the probability distribution of that generated event producing a measurement  $m_j$ . In

this analysis, the efficiency  $\epsilon_i$  is set to 1, so that the unfolding recovers the true distribution of the triggered events, after which efficiency corrections are applied. The  $g_0$  bin, a true multiplicity of 0 in a given pseudorapidity range, is also used, as events can be recorded in which there are no tracks in the accepted pseudorapidity range, but there are tracks outside this range. The  $m_0$  bin is used similarly.

Equation 3.16 corresponds to the inverse of the response, and an estimate of the solution is given by:

$$\hat{g}_i = \sum_j m_j P(g_i | m_j), \quad (3.18)$$

where  $\hat{g}_i$  is the estimate of the true generated distribution. If the initial distribution  $P_0(g_i)$  and estimator of the solution  $P(\hat{g}_i)$  do not agree, then the solution does not agree with the measured data. However, this step brings the (so far guessed) knowledge of the generated distribution closer to the truth, as the solution estimate lies between the initial guess and the true distribution, as shown in Figure 3.21.

A subsequent calculation using the previous solution as the *a priori* initial distribution will yield an even closer estimate, as the procedure builds upon the information found in the previous iteration, and these iterations are continued until a satisfactory convergence has been achieved. This updating of the probabilities based on new information, i.e. the agreement between the solution and the prior distribution, is the basis of the Bayesian interpretation of probability [89].

Although the calculation of the estimated solution does not actually create the

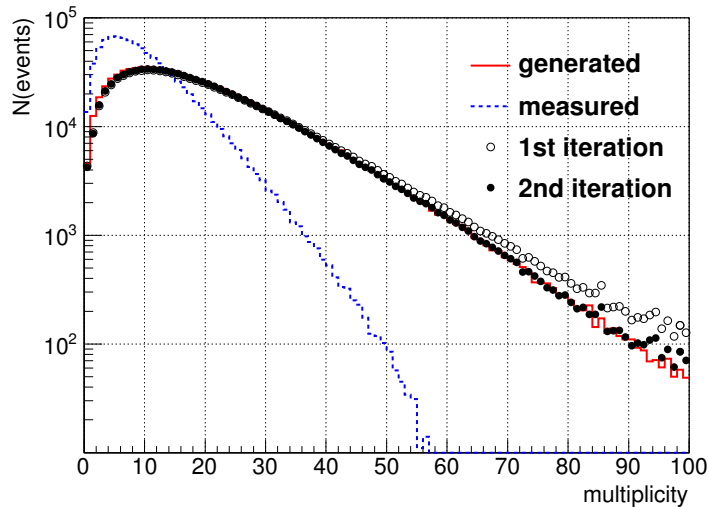


Figure 3.21: Two iterative unfolding steps using toy data and a uniform prior distribution. The second step (closed circles) is much closer to the true generated line (red) than the first step (open circles).

inverse of the response matrix, if an infinite (or very large) number of iterations are used the solution does converge to the oscillating solution given by the inverse response, shown in Figure 3.22. By stopping the iterations after a convergence condition has been met, the procedure does not reach the oscillatory stage, which is an inherent regularisation of this method.

### Convergence

The regularisation afforded by this method is controlled by the choice of prior distribution and the number of iterations used.

For the first parameter, a uniform prior is the default starting point, as it means that all causes, or generated multiplicity values, are considered as possible contribu-

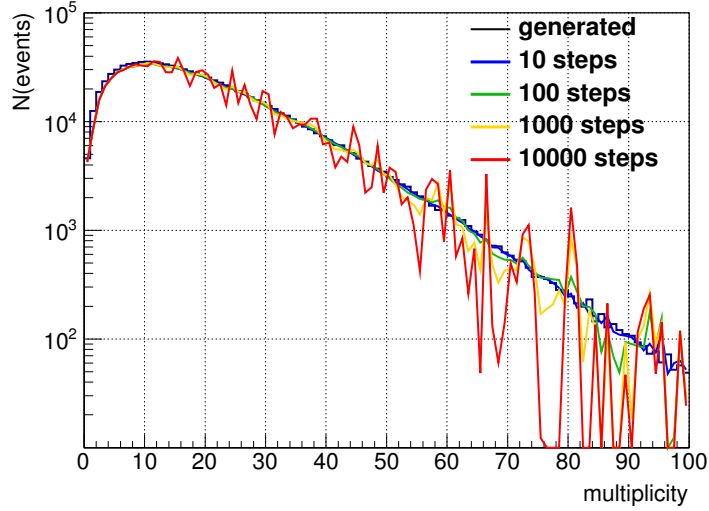


Figure 3.22: Unfolding results of toy data using an increasing number of iterations. More iterations introduces the oscillatory instability also found using the inverse matrix solution. The smoothest result is from the fewest iterations, in this example 10 iterations (blue line).

tions to an effect, or measured multiplicity value. Using a physically motivated or estimated distribution with a shape similar to the truth would achieve convergence in fewer iterations, especially when the distribution has a steep inverse exponential slope such as the multiplicity. This is borne out in the fact that using the true generated vector in unfolding the measured vector for a Monte Carlo sample provides the solution in one step. However, it introduces the assumption that any bins of the prior distribution without a value will not contribute to the measured distribution regardless of the number of iterations. This is a problem for this measurement, as the Pythia and Phojet generators predict a more steeply falling slope in multiplicity at  $\sqrt{s} = 7$  TeV, and thus do not provide many events with very high multiplicity. Therefore, a flat prior is used to give an unbiased start to the unfolding.

The second control of regularisation lies in the number of iterations used, clearly

too few iterations may not yield a solution close to the truth and too many introduces wild oscillations. A measure of agreement is needed between each iteration to judge whether the method has converged. The solution given by each iteration cannot be used directly in an agreement test, as the true distribution of real data is unknown. However the solution can be convoluted by the response matrix to show what measurement distribution would be seen if that solution were true. Comparing this “folded solution” with the measured data at each iteration then gives an agreement measure to test convergence, which when satisfied means a satisfactory solution to equation 3.5 has been found.

To test the agreement between the folded iteration result and the measurement, a straightforward  $\chi^2$  test can be used, the simplest form of which is:

$$\chi^2 = \sum_i \frac{(f_i - m_i)^2}{\sigma(f_i)}, \quad (3.19)$$

where  $\mathbf{f}$  is the iteration result folded with the response matrix, and  $\sigma(\mathbf{f})$  is the uncertainty of the folded result. This assumes that only the folded iteration result has uncertainties, which are also uncorrelated; both assumptions are untrue. The original measured distribution  $\mathbf{m}$  has uncorrelated Poissonian errors, which need to be taken into account as follows;

$$\chi^2 = \sum_i \frac{(f_i - m_i)^2}{\sqrt{\sigma(f_i)^2 + \sigma(m_i)^2}}, \quad (3.20)$$

where  $\sigma(\mathbf{m})$  is the uncertainty of the original measured distribution. In addition,

the unfolding procedure moves entries in the iterative result between bins, such that the errors of those bins are now correlated, requiring a covariance matrix to incorporate these into the agreement calculation. Thus, as shown in [89] the  $\chi^2$  equation becomes

$$\chi^2 = \sum_i \sum_j (f_i - m_i) V_{ij}^{-1} (f_j - m_j), \quad (3.21)$$

where  $V_{ij}^{-1}$  is an element of the inverse covariance matrix incorporating the covariance of the folded result,  $\mathbf{f}$ , and the variance of the measured distribution  $\mathbf{m}$ , by simply adding  $\sigma(\mathbf{m})$  to the diagonal of  $V(\mathbf{f})$  before inverting it.

### Covariance Determination

The covariance matrix  $V$  is too complicated to calculate analytically during the iteration process, but can be calculated numerically with toy simulations, as shown in [98]. Each iteration step of the unfolding needs to have a covariance matrix, which will be unique due to the correlation of uncertainties increasing with each iteration. Therefore, enough covariance matrices must be prepared to cover a reasonable amount of iterations, this analysis found 20 to be enough.

For every iteration, the propagated errors from the finite events in the generated response matrix and statistical error of the measured data are both estimated using 1000 pseudo experiments each. Every pseudo experiment begins with either the data or response matrix being ‘‘Poisson-shaken’’, a term coined here to mean that each

cell of the data vector or response matrix is set to a random number taken from a Poisson distribution with the cells original value as the mean. The 1000 unfolded solutions, and the 1000 solutions folded again, are then used in equation 3.22, where  $\mathbf{x}$  is the unfolded/folded vector, to compute the matrices for the data-shaken and response-shaken covariances separately:

$$\text{cov}(x_i, x_j) = E[x_i x_j] - E[x_i]E[x_j]. \quad (3.22)$$

These separate covariances are added together to hold the total uncertainty introduced and propagated through this iterative method, as the two sources of error, finite MC statistics and measured data variance, are uncorrelated.

With the covariance matrices for the  $n$ th iteration result and its folded version, the  $\chi^2$  from equation 3.21 can be used when making comparisons with the previous iteration solution and the original measured vector respectively. The variance of the measured vector and the prior vector are added to the covariance matrices before inversion. Now there are two  $\chi^2$  checks for convergence; one between the current and prior solution, and another between the folded version of the current solution and the measured distribution.

A successful unfolding would achieve  $\chi_{\text{folded}}^2 \sim 1$ , showing neither over-determination of the result (small  $\chi_{\text{folded}}^2$ ) or an ambiguous fit ( $\chi_{\text{folded}}^2$  much more than 1). This value shows that the two distributions are likely to have come from the same underlying function, the differences consistent with sampling and statistical uncertainties.

Therefore, a threshold of  $\chi_{\text{folded}}^2 < 1.1$  is used for the measured and folded result vector comparison to stop iterating. There is a hard limit of 20 iterations, found through numerous tests of the method to be the maximum number of iterations needed for convergence to occur, whether or not the above agreement requirement is met.

The other test of convergence is to measure how much the  $\chi_{\text{folded}}^2$  changes between each iteration, as so:

$$\Delta\chi_{\text{folded}}^2(n) = \frac{\chi_{\text{folded}}^2(n)}{\chi_{\text{folded}}^2(n-1)} - 1, \quad (3.23)$$

where  $n$  is the iteration number, and 1 is subtracted to reveal simply the fractional change in the agreement measure. This is particularly useful for when the solution converges before satisfying the  $\chi_{\text{folded}}^2 < 1.1$  requirement, as shown in Figure 3.23. The  $\chi_{\text{folded}}^2$  agreement measure converges almost asymptotically after a rapid change for the first 5 or 6 iterations. After these first few iterations, the  $\chi_{\text{folded}}^2$  changes much less rapidly, and more iterations will introduce oscillations into the solution. A threshold of  $\Delta\chi_{\text{folded}}^2 < 2\%$  was found to be the optimal cutoff to prevent the solution being ruined in the pursuit of a satisfactory  $\chi_{\text{folded}}^2$ .

### Model Dependence

It is worth checking if the choice of generator used to produce the response matrix influences the unfolded result. With Pythia and Phojet simulated data sets read-

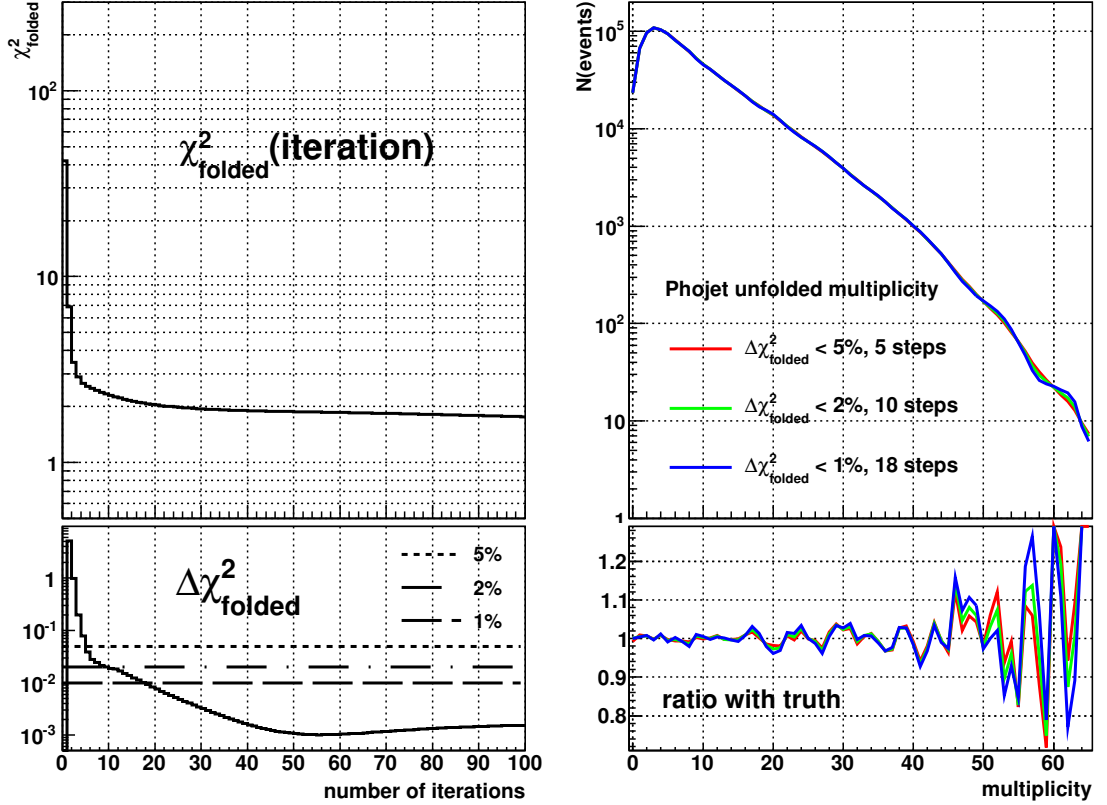


Figure 3.23: These plots are from unfolding Phojet simulated 7 TeV data with a Pythia flat multiplicity response map. (Top left) The agreement measure  $\chi^2_{\text{folded}}$  as a function of number of iterations. In this case, it shows a convergence to a solution that does not meet the agreement criteria between the folded solution and the measured distribution. (Bottom left) The fractional change in  $\chi^2_{\text{folded}}$  for each iteration, with lines marking a change of 5%, 2% and 1%. (Top right) The three unfolding solutions when iterations are stopped at a  $\Delta\chi^2_{\text{folded}}$  of 5%, 2% and 1%. (Bottom right) Ratio of the three unfolding solutions from top right with the true generated multiplicity. For increasing number of iterations, the deviations from the true shape increase.

ily available in the analysis framework, comparisons were made between these two models, unfolding a measured distribution of one using the response map generated with the other. The first set of tests used response maps populated according to the model distribution of the multiplicity; as such they follow a generally negative exponential shape and are poorly populated at higher multiplicity. This should not affect the unfolding of the model distributions, however, as they both have a similar range.

The results of this are shown in Figure 3.24, and clearly show that the procedure gives a satisfactory solution when using a response map filled with a different model of similar shape and range, and similar number of events. The iterations stopped after achieving a  $\chi_{\text{folded}}^2 < 1.1$  in only 6 – 8 steps. This is as expected, because the response map describes which true multiplicities contribute to a measured multiplicity, regardless of how the true multiplicities are distributed. Obviously, more events in a true cell gives more reliable information on how it contributes to the measured distribution.

For the data collected at the LHC, which reaches higher multiplicities than predicted by Pythia and Phojet [23], especially at  $\sqrt{s} = 7$  TeV, a response map filled according to a uniform distribution is needed to populate the map at high multiplicities. This also has the benefit of distributing the number of events more evenly between the lower and higher multiplicity bins, reducing the introduced uncertainty from unfolding into the less populated tail of the distribution.

### 3.5. UNFOLDING THE MULTIPLICITY DISTRIBUTION

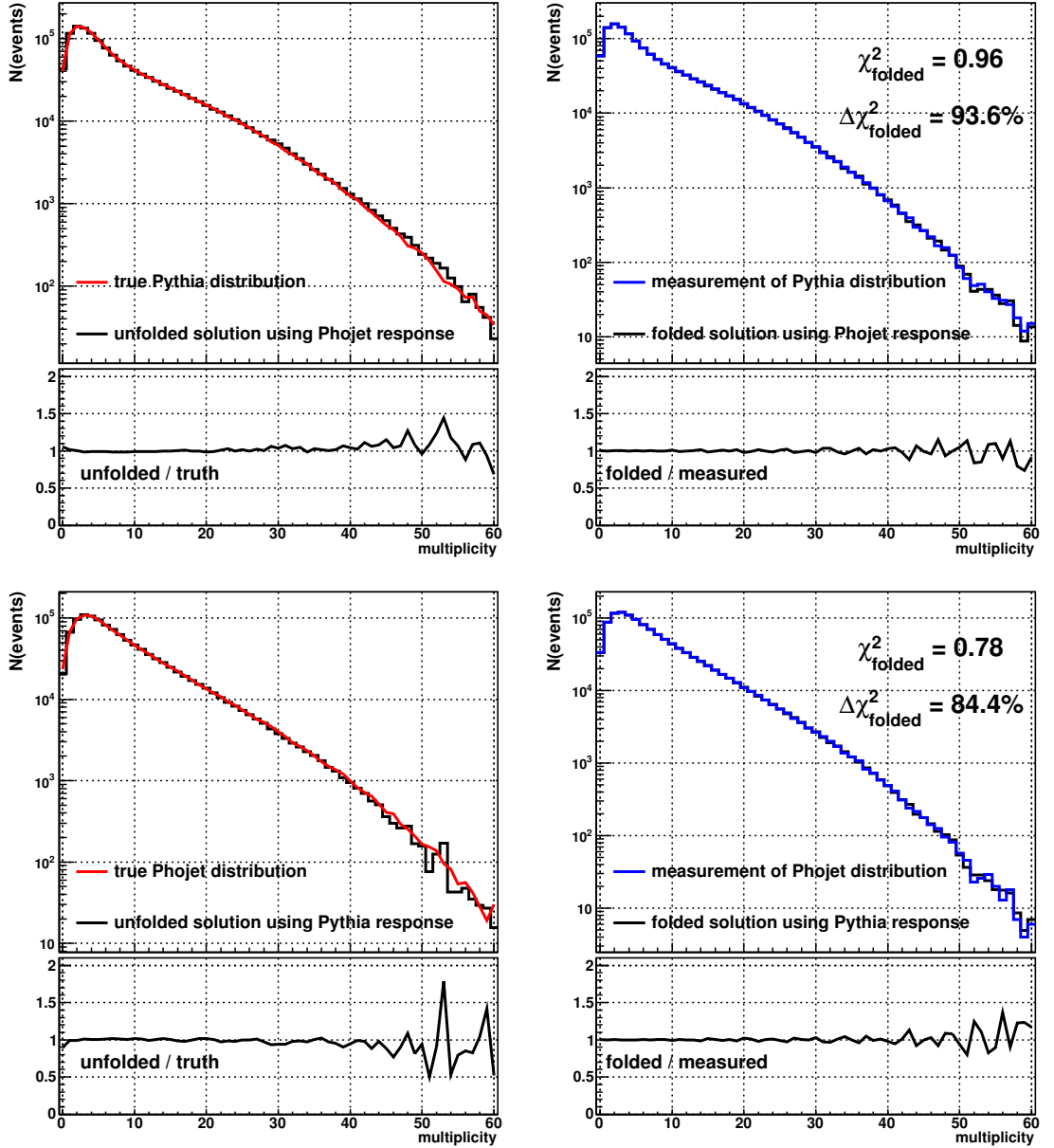


Figure 3.24: Results of unfolding Pythia data with a Phojet minimum bias response matrix and vice versa. (Top left) Unfolded (black) and true (red) Pythia distribution using Phojet minimum bias response map, with their ratio underneath. (Top right) Measured (blue) and convolved version of unfolded (black) Pythia distribution using Phojet minimum bias response map, with their ratio underneath. (Bottom left) Unfolded (black) and true (red) Phojet distribution using Pythia minimum bias response map, with their ratio underneath. (Bottom right) Measured (blue) and convolved version of unfolded (black) Phojet distribution using Pythia minimum bias response map, with their ratio underneath.

The flat multiplicity response map was made only with Pythia, so this map was tested in unfolding a Pythia and Phojet measurement, as shown in Figure 3.25. This time, the iterations stop due to the change in  $\chi_{\text{folded}}^2$ , converging to values above the desired value. The ratios between the solution with the true vector and the folded solution with the measured vector still show good agreement in the range shown, and the fact that the unfolding iterations stopped at all means that the  $\chi_{\text{folded}}^2$  was converging. The reason why it is higher than required is that the calculation of  $\chi_{\text{folded}}^2$  includes all the non zero bins, and with the flat response map, the very tail of the measured distribution is unfolded to be compared with the sparsely populated tails of the simulated distributions. Using the uniformly filled response to unfold the measured data distributions with different pseudorapidity ranges, collision energies and transverse momentum cuts, the unfolding always converges to a satisfactory  $\chi_{\text{folded}}^2$ .

### 3.6 Mean $p_T$ as a Function of Multiplicity

The mean transverse momentum distribution as a function of multiplicity shows the average outward momentum of particles produced in inelastic proton-proton collisions, indicating the energy produced in the collision which is shared between its products, and showing the correlation of this to the number of particles produced in the collision.

### 3.6. MEAN $P_T$ AS A FUNCTION OF MULTIPLICITY

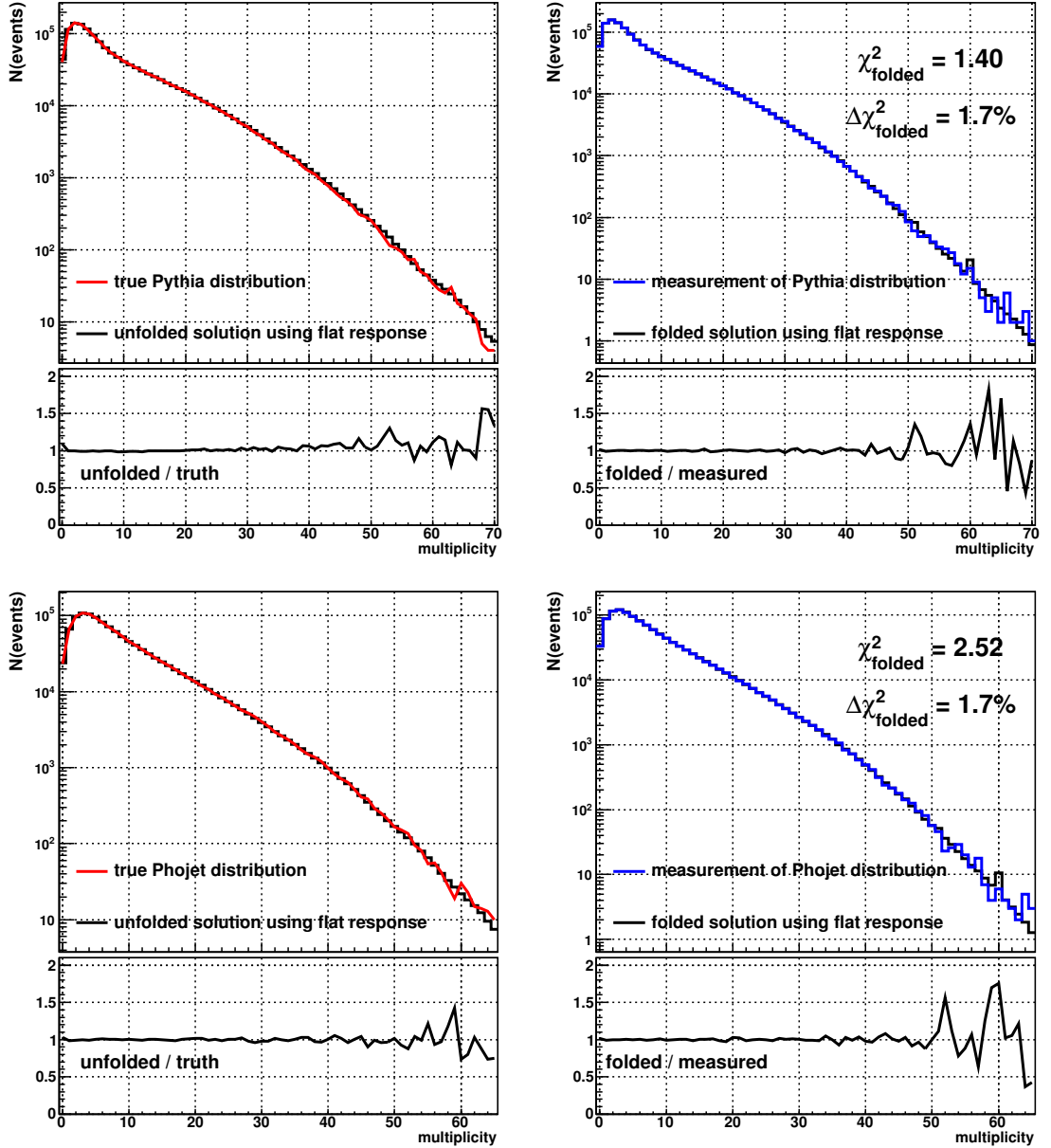


Figure 3.25: Results of unfolding Pythia and Phojet data with a Pythia flat multiplicity response matrix. (Top left) Unfolded (black) and true (red) Pythia distribution using flat response map, with their ratio underneath. (Top right) Measured (blue) and convolved version of unfolded (black) Pythia distribution using flat response map, with their ratio underneath. (Bottom left) Unfolded (black) and true (red) Phojet distribution using Pythia flat response map, with their ratio underneath. (Bottom right) Measured (blue) and convolved version of unfolded (black) Phojet distribution using Pythia flat response map, with their ratio underneath.

This analysis uses the same event and vertex selections as the multiplicity analysis above, as well as the primary track criteria. Tracks from the SPD are not used, as it does not provide momentum information. This leaves tracks from the TPC and ITS, known as “global” tracks. Global tracks are constructed with both the ITS and TPC if possible, “ITSTPC” tracks. Otherwise, if a track is not detected by the TPC (generally the case for low momentum particles), just the ITS is used, providing “ITS complimentary” tracks.

To compare the  $p_T$  resolution of the two types of tracks, the relative resolution is plotted as a function of the  $p_T$  for ITSTPC tracks and ITS complimentary tracks.

The relative  $p_T$  resolution is given by

$$\frac{\sigma(p_T)}{p_T}, \quad (3.24)$$

where  $\sigma(p_T)$  is the uncertainty in  $p_T$  of the measured track. Figure 3.26 shows the relative  $p_T$  resolution for ITSTPC tracks, and the fraction of tracks with better resolution than a given value along the x-axis. There is a spread of values at lower momenta, less than 500 MeV/c, but the majority of values lie along a narrow ridge showing a relative resolution of 1-2%. Almost 77% of ITSTPC tracks have a better resolution than 2%, and 99% better than a 5% resolution. This shows that tracks found by the TPC are reconstructed well for measuring  $p_T$ .

The same information is shown for ITS complimentary tracks in Figure 3.27, showing a larger spread in resolution for all momenta, and less than 1% of tracks with a

### 3.6. MEAN $P_T$ AS A FUNCTION OF MULTIPLICITY

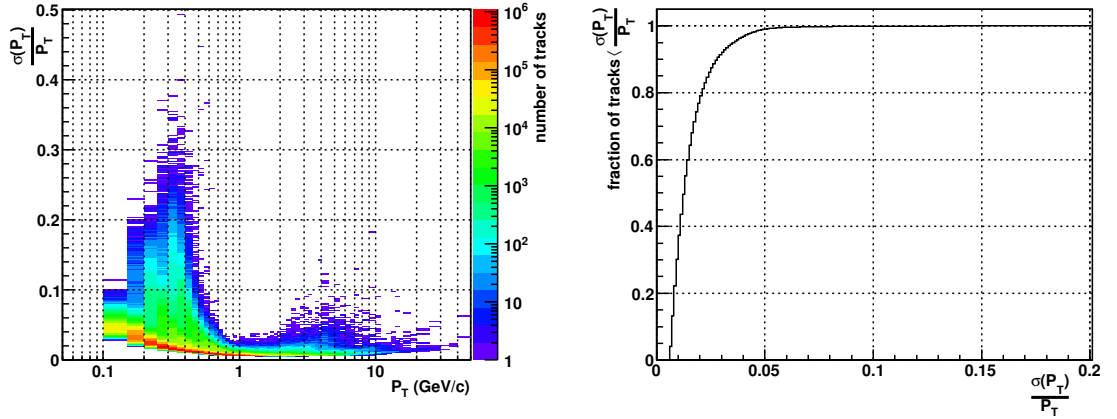


Figure 3.26: (Left) Relative transverse momentum resolution of ITSTPC tracks as a function of  $p_T$ . (Right) The fraction of ITSTPC tracks with better  $p_T$  resolution than a given value, as a function of relative  $p_T$  resolution. Data is MC generated.

resolution better than 5%, and  $\sim 64\%$  of tracks with a resolution better than 10%. These make up the minority of the track population ( $\sim 12\%$  according to the MC simulations used to produce these figures) which were not reconstructed by the TPC mainly because of not leaving many hits or clusters in the detectors. Whether this is due to decay, detector interaction, or detector inefficiencies and acceptance, these tracks are harder to reconstruct than those found by the TPC, and only the ITS can reconstruct these on its own. As such, the  $p_T$  resolution will be lower, although the ITS is capable of achieving good resolution on its own (when used in conjunction with the TPC, if possible, the combined reconstruction provides a better  $p_T$  resolution than individual detectors.) For this reason, tracks not seen by the TPC are ignored in the mean  $p_T$  measurement.

The structure seen in the left hand plot of Figure 3.27 is most likely a feature of the combination of hits used in the ITS to reconstruct the track. For example, some

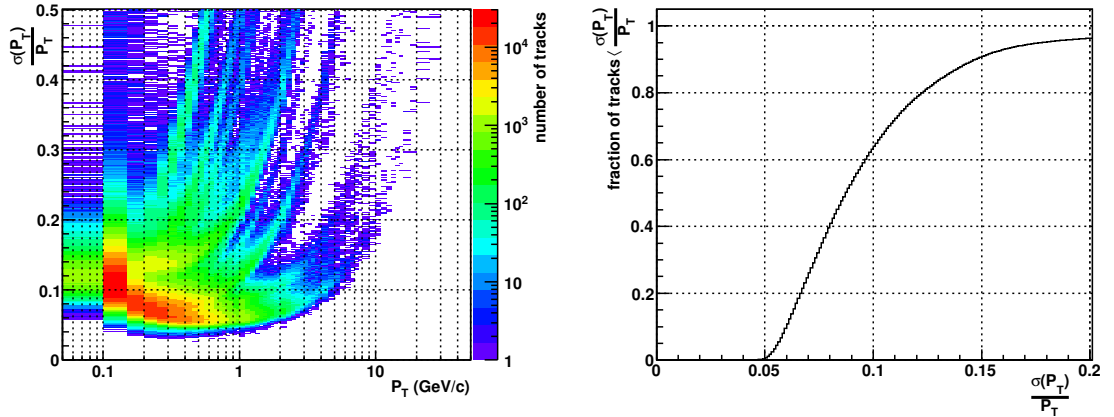


Figure 3.27: (Left) Relative transverse momentum resolution of ITS complimentary tracks, as a function of  $p_T$ . (Right) The fraction of ITS complimentary tracks with better  $p_T$  resolution than a given value, as a function of relative  $p_T$  resolution. Data is MC generated.

tracks may only have hits in the outer 4 layers, not the innermost 2, and the  $p_T$  resolution as a function of  $p_T$  for these tracks will follow some curve. The different combinations of hits in the six ITS layers leads to the different curves present in the relative resolution plot. A similar structure is also seen for the ITSTPC tracks in Figure 3.26, though it is not as prominent, as the TPC can reconstruct up to 159 points per track.

With the ITSTPC tracks selected, the efficiency of reconstructing these tracks, as a function of  $p_T$ , is required to correct for undetected tracks that are part of the selected event. These were determined from simulation using both Phojet and Pythia for all three energies used in this analysis, shown in Figure 3.28. The tracking efficiencies should not change as a function of collision energy, but the detector set-up changed over time, so the different efficiencies account for this. There is an almost negligible difference between the Pythia and Phojet models for the tracking

efficiency, so the Pythia efficiencies were used with the measured data.

With the efficiencies measured, the calculation of the mean  $p_T$  can be calculated per event, and then averaged over the total number of events:

$$\overline{p_T} = \frac{1}{N_e} \sum_{N_e} \overline{p_T} |_{\text{event}}, \quad (3.25)$$

where  $N_e$  is the total number of events in the data sample, and  $\overline{p_T} |_{\text{event}}$  is the mean  $p_T$  for a single event. For each event, each ITSTPC track found will contribute its  $p_T$  value to the mean, but this must be corrected for the efficiency of detecting tracks with that  $p_T$ . The  $p_T$  sum of all the tracks is increased, as each track contributes its own  $p_T$ , and the upwards correction accounts for the  $p_T$  from tracks that were missed. This upwards correction also applies to the number of ITSTPC tracks found in one event, represented from here onwards as  $N_T$ . Thus, the corrected number of tracks for an event ( $\hat{N}_T$ ) becomes the sum of the inverse efficiencies for each track found;

$$\hat{N}_T = \sum_{i=1}^{N_T} \frac{1}{\varepsilon(p_T(i))}, \quad (3.26)$$

where  $\varepsilon(p_T(i))$  is the detection efficiency for particles with a given  $p_T$ . Then the mean  $p_T$  per event is given by:

### 3.6. MEAN $P_T$ AS A FUNCTION OF MULTIPLICITY

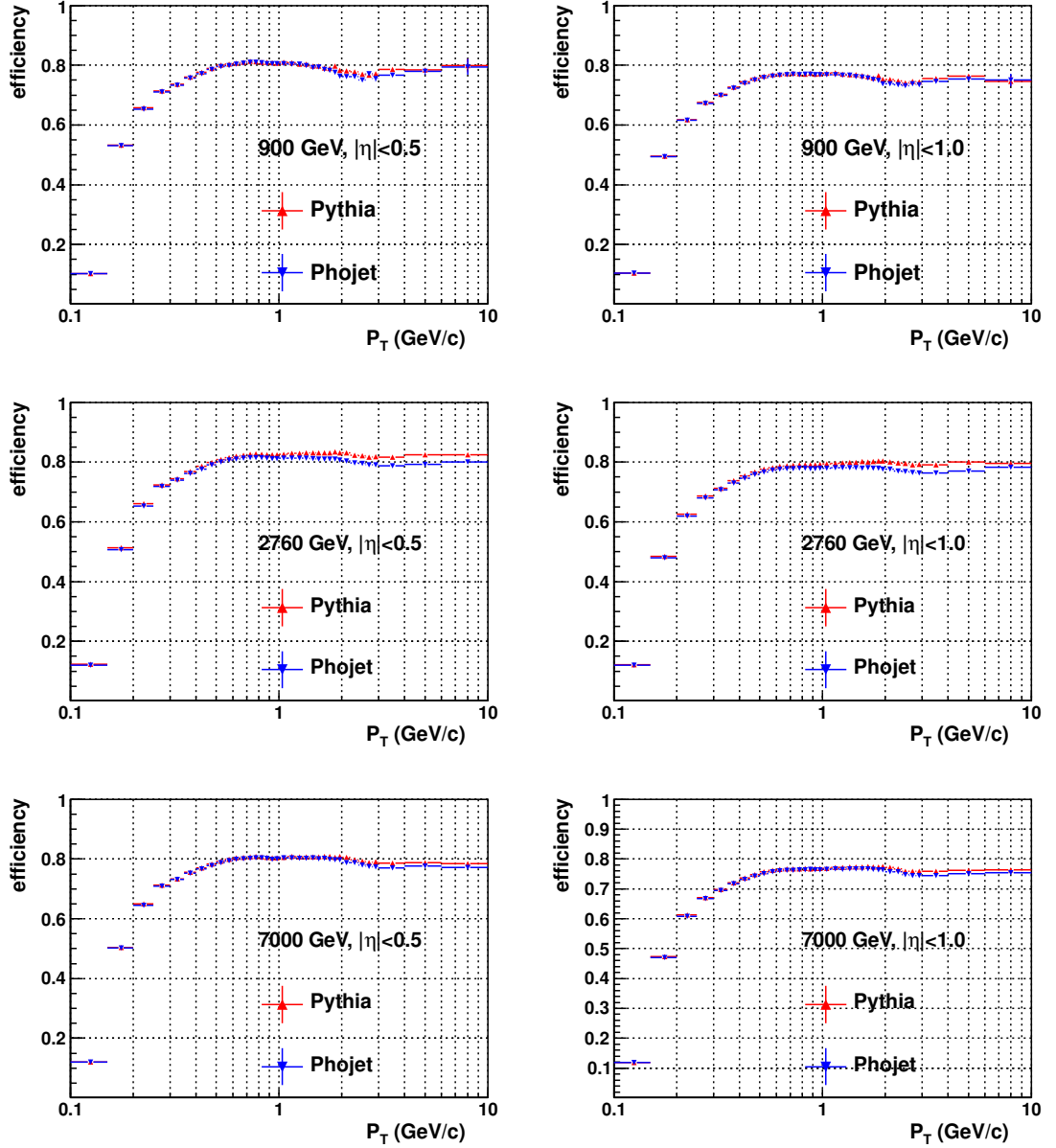


Figure 3.28: The efficiency of detecting ITSTPC tracks as a function of  $p_T$  for different collision energies and pseudorapidity ranges, indicated in the legends.

$$\begin{aligned} \overline{p_T}|_{\text{event}} &= \frac{\sum_{i=1}^{N_T} p_T(i) \varepsilon(p_T(i))^{-1}}{\sum_{i=1}^{N_T} \varepsilon(p_T(i))^{-1}} \\ &= \frac{1}{\hat{N}_T} \sum_{i=1}^{N_T} \frac{p_T(i)}{\varepsilon(p_T(i))} . \end{aligned} \quad (3.27)$$

These data are stored along with the measured multiplicity for each event. The multiplicity measure is the same used in the multiplicity analysis, ITSTPC global tracks and ITS complimentary tracks, to give the closest possible estimate to the true multiplicity of the event. For each bin of multiplicity  $N_m$ , the average mean  $p_T$  can then be computed:

$$\overline{p_T}(N_m) = \frac{1}{N_e(N_m)} \sum_{i=1}^{N_e(N_m)} \overline{p_T}|_i , \quad (3.28)$$

where  $N_e(N_m)$  is the number of events with a given measured multiplicity  $N_m$ .

This method was tested on simulated data to compare its result with the true mean  $p_T$  distribution as a function of the true multiplicity, generated by the model. Figure 3.29 shows this comparison for Pythia generated  $\sqrt{s} = 900$  GeV data, for two minimum  $p_T$  thresholds (150 MeV/c and 500 MeV/c) and two pseudorapidity ranges ( $|\eta| < 0.5$  and  $|\eta| < 1.0$ ). The same is shown for Phojet generated  $\sqrt{s} = 2760$  GeV data and Pythia generated  $\sqrt{s} = 7000$  GeV data in Figures 3.30 and 3.31 respectively.

For each of the Figures 3.29, 3.30 and 3.31, the measured mean  $p_T$  is calculated using

### 3.6. MEAN $P_T$ AS A FUNCTION OF MULTIPLICITY

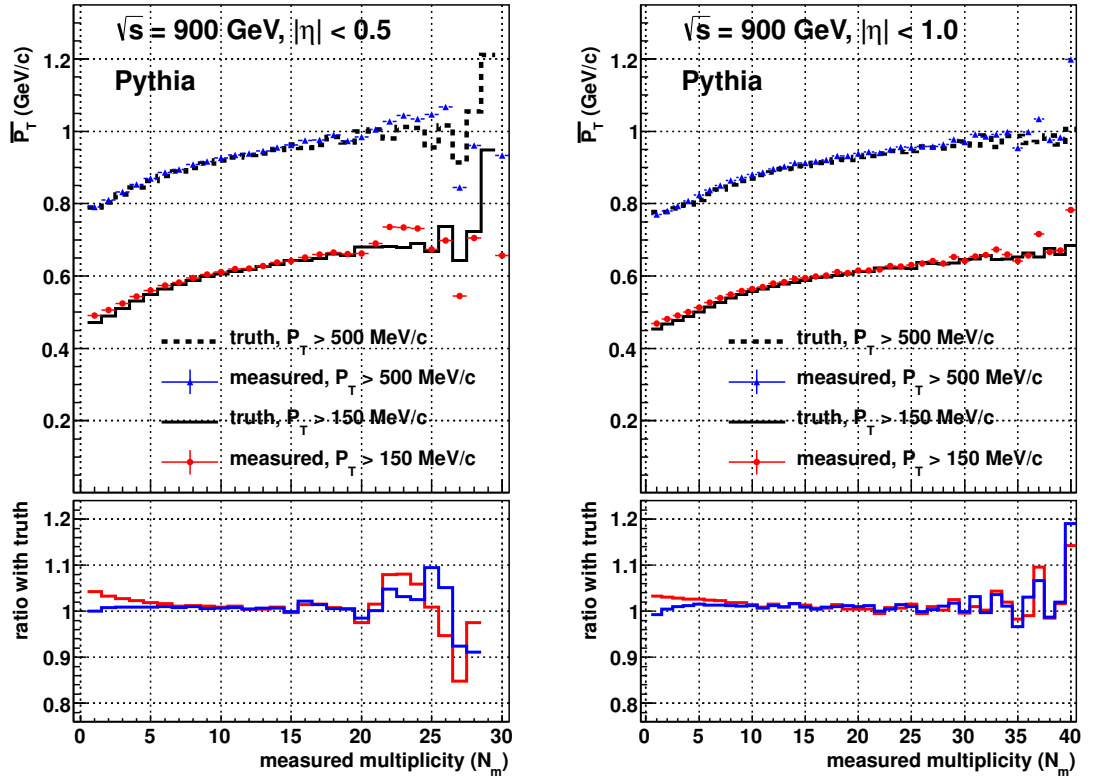


Figure 3.29: Mean  $p_T$  versus measured multiplicity for Pythia generated data at  $\sqrt{s} = 900$  GeV, with two momentum thresholds and the corresponding true distributions shown together, and the ratio of the measured to true distribution inset underneath. The left side shows the measurement with a pseudorapidity range of  $|\eta| < 0.5$ , the right with  $|\eta| < 1.0$ .

### 3.6. MEAN $P_T$ AS A FUNCTION OF MULTIPLICITY

the efficiencies taken from the generated data *not* used to generate the true distribution. That is, if the measurement is made on Pythia data, then the efficiencies from Phojet are used to correct them. Though the tracking efficiencies from Pythia and Phojet are shown to be very similar, these comparisons are more independent than using Phojet efficiencies to correct Phojet generated data. If there was a large discrepancy between the measurement and the truth, comparing in this way would show it better; but the measured mean  $p_T$  using either Phojet or Pythia efficiency corrections are negligibly different (less than 0.1%).

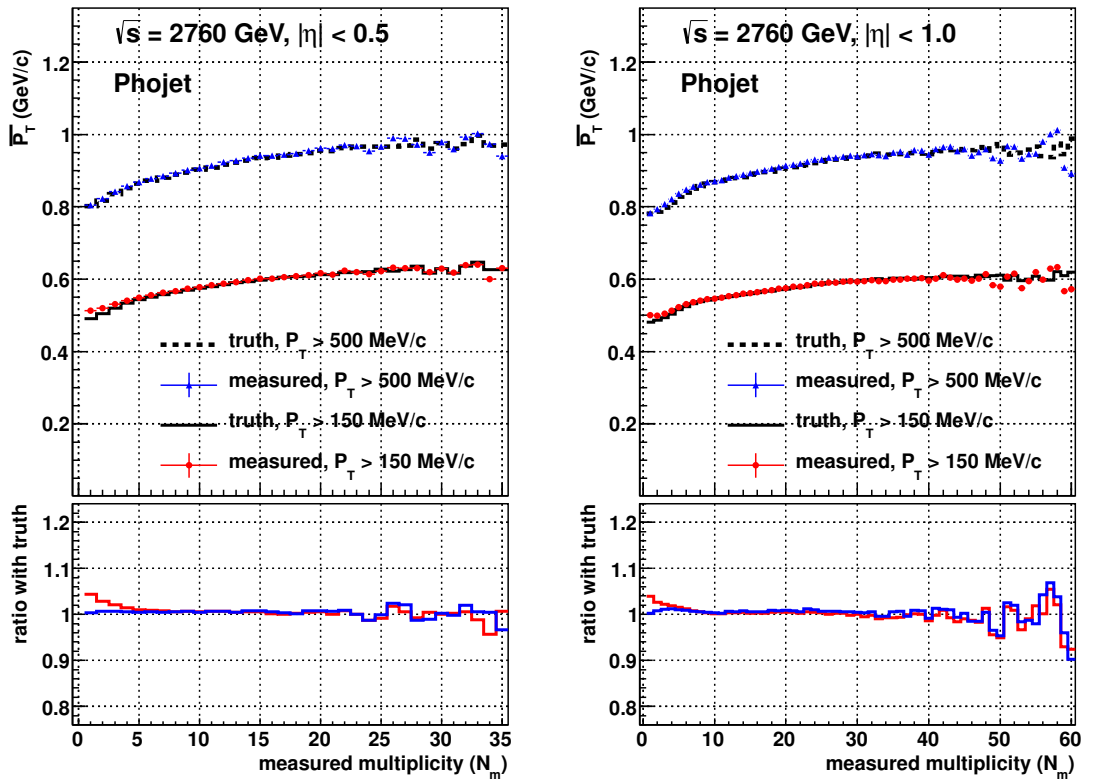


Figure 3.30: Mean  $p_T$  versus measured multiplicity for Phojet generated data at  $\sqrt{s} = 2760$  GeV, with two momentum thresholds and the corresponding true distributions shown together, and the ratio of the measured to true distribution inset underneath. The left side shows the measurement with a pseudorapidity range of  $|\eta| < 0.5$ , the right with  $|\eta| < 1.0$ .

The highest multiplicity bins in the plots show fluctuations due to the low event

### 3.6. MEAN $P_T$ AS A FUNCTION OF MULTIPLICITY

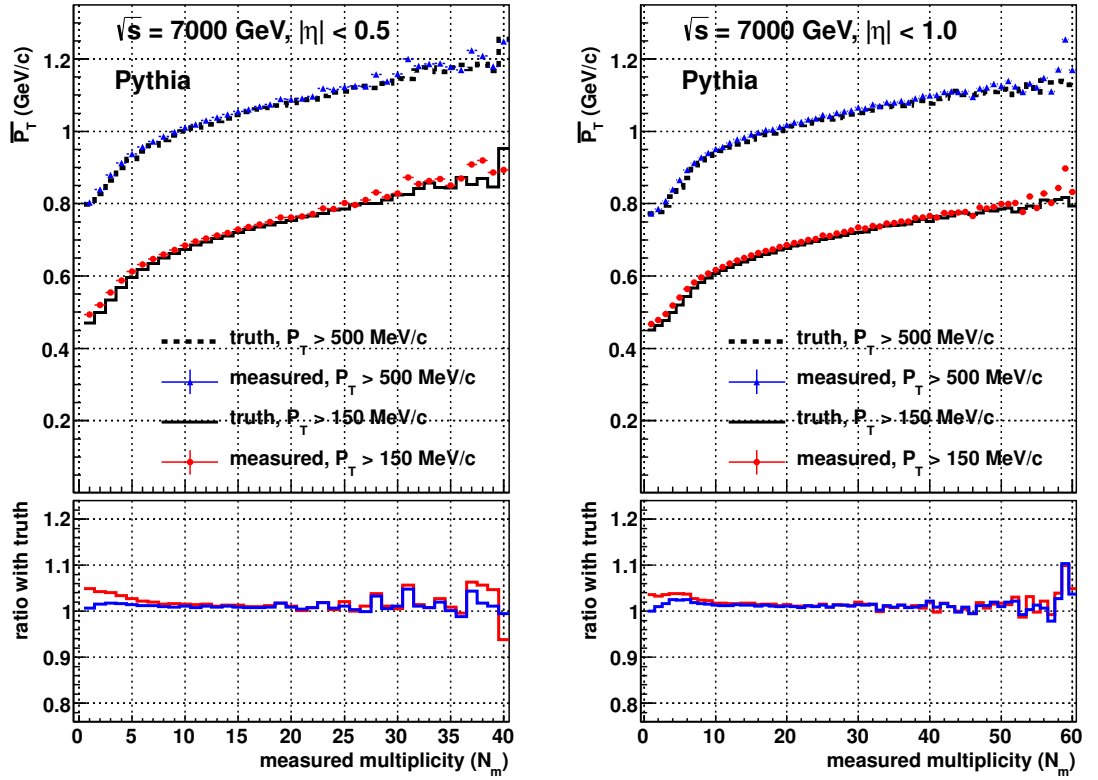


Figure 3.31: Mean  $p_T$  versus measured multiplicity for Pythia generated data at  $\sqrt{s} = 7000 \text{ GeV}$ , with two momentum thresholds and the corresponding true distributions shown together, and the ratio of the measured to true distribution inset underneath. The left side shows the measurement with a pseudorapidity range of  $|\eta| < 0.5$ , the right with  $|\eta| < 1.0$ .

population of those bins, and so for the real data the last few multiplicity bins will be grouped together. For the lower momentum threshold selection, the ratio between the true and measured distribution is systematically higher throughout the lowest multiplicity bins. This is due to the multiplicity measure (ITSTPC tracks along with ITS complimentary tracks, with  $p_T$  above 150 MeV/c) having a correlation with the true multiplicity that is almost, but not quite, exactly proportional, as shown in Figure 3.13. Thus, for the first 5-10 bins of multiplicity where the gradient of the of the mean  $p_T$  distribution is largest, the migration of events into lower multiplicity bins gives a higher than expected mean  $p_T$  for that multiplicity, with respect to the true distribution. This effect is minimal when the minimum track  $p_T$  is 500 MeV/c, as the reconstruction efficiency for these tracks is almost uniform in  $p_T$ , and higher than for tracks with lower  $p_T$ . This is shown in Figure 3.32 for ITSTPC and ITS complimentary tracks, where the addition of ITS complimentary tracks increases reconstruction efficiency when compared to without them in Figure 3.28. The additional tracks have poorer  $p_T$  resolution as shown in Figure 3.27, which is why they are not used in the mean  $p_T$  calculation.

Apart from the final bins of multiplicity, which will be grouped together for the data, the agreement between the measured and generated mean  $p_T$  distribution is better than 5% for the rest of the distribution, and the mid multiplicity region has agreement better than 2%. The initial overestimation of the measurement with regard to the generated distribution for tracks with  $p_T > 150$  MeV/c, as well as the overall difference between the measured and true distributions, will be used as

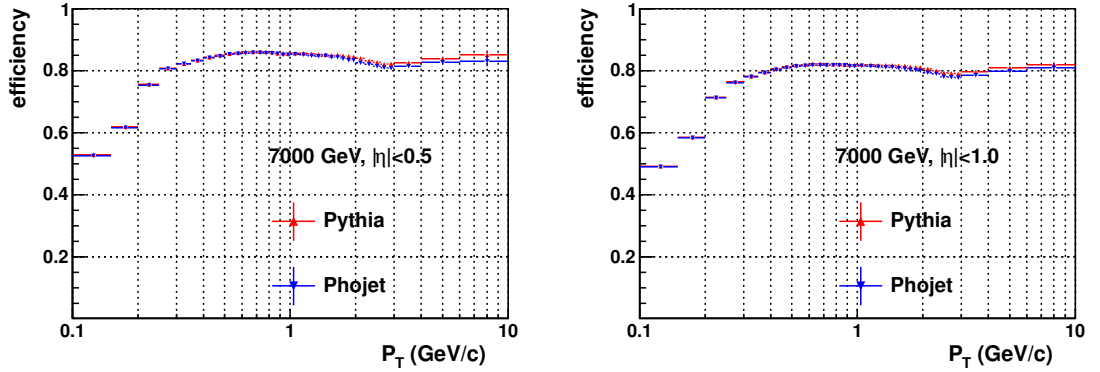


Figure 3.32: The efficiency of detecting ITSTPC tracks and ITS complimentary tracks as a function of  $p_T$  for Pythia and Phojet generated  $\sqrt{s} = 7$  TeV data, for  $|\eta| < 0.5$  and  $|\eta| < 1.0$ .

systematic errors for the measured data.

## 3.7 Systematic Uncertainties

This section outlines the different contributions to the systematic uncertainty of the charged particle multiplicity and mean  $p_T$  measurements. Conservative estimates are given based on studies in this work, and where appropriate are quoted from published ALICE results.

### 3.7.1 Charged Particle Multiplicity

The track selection criteria have been studied previously in terms of the systematic uncertainty of the multiplicity distribution [23, 53], and found to give a negligible contribution to the systematic uncertainty. This is reasonable, as the unfolding procedure depends on a response matrix built with simulated events defined by the

true multiplicity and measured multiplicity, using the same track selections as for real data.

The unfolding procedure itself has an uncertainty based on the statistical uncertainty of the response matrix. The statistical uncertainty of the measured data is negligible with respect to that of the response matrix. This is estimated using a toy Monte Carlo with 1000 pseudo-experiments, where it is found that this systematic uncertainty increases for every iteration, and can reach up to 10% at the highest multiplicity. This uncertainty is calculated for each unfolded multiplicity distribution.

The correction to the number of NSD or inelastic events has the largest significance for the first few multiplicity bins, and is estimated using the difference between the efficiencies of selecting these events given by Pythia and Phojet, shown in Table 3.1. This is as much as 5%, but above multiplicities of 10, it has a negligible effect.

The effect of generator dependence was studied with Pythia and Phojet, unfolding a measured distribution from generator with the response matrix generated from the other, and there was found to be negligible dependence.

The effect of the material budget on tracking was studied in [99], and found to have a 0.6% systematic uncertainty for tracks with  $p_T > 150$  MeV/c whereas previous ALICE multiplicity papers found it was negligible. Taking a conservative approach to the systematic uncertainty, the uncertainties given in the former study will be taken for all tracks.

The effect of pileup on the multiplicity distribution is studied in section 3.3.3, giving a conservative estimate of the remaining pileup after the removal of discoverable pileup, using data taken when the average number of collisions per bunch crossing  $\mu = 0.061$ . The  $\mu$  used in the pileup study is the average  $\mu$  for the  $\sqrt{s} = 7$  TeV data, at  $\sqrt{s} = 2.76$  TeV the average interaction probability is  $\mu = 0.046$  and at  $\sqrt{s} = 0.9$  TeV it is 0.023. Thus, the systematic uncertainty estimated for pileup will cover all three collision energies studied.

Given that the mean multiplicity of the distribution used for the pileup study is  $\overline{N_{CH}} = 9.570 \pm 0.005$ , it is seen from Figure 3.11 that up to a multiplicity of  $4 \times \overline{N_{CH}}$  the fraction of pileup events is  $< 2\%$ , at  $6 \times$  the pileup is  $< 4\%$ , and  $8 \times$  it is  $< 10\%$ , increasing to 25% pileup in the bin with  $10 \times$  the average multiplicity. The uncertainty of these fractions is taken from Figure 3.12, where the predicted change from pileup removal per bin is compared to the measured data. There is good agreement up to  $5 \times \overline{N_{CH}}$ , after which the discrepancy increases to approximately 5 – 10%, fluctuations in the measured data requiring a trend to be estimated rather than a direct bin to bin comparison. Thus, from Figure 3.12; for multiplicities higher than  $8 \times \overline{N_{CH}}$ , the uncertainty of the systematic error itself from pileup is conservatively estimated to be 100%, thus making the systematic error from pileup at this multiplicity to be  $\pm 20\%$ .

Studies of the systematic effect of background events [53], such as beam-gas events, have found them to be negligible.

The particle composition of events, or the amount of different types of particles produced, can change the detector response due to the different interacting behaviour of particle types in the detector. This has been studied in [99], and a conservative uncertainty of 1% is applied to the distribution due to this effect.

### 3.7.2 Mean $p_T$ as a function of Charged Particle Multiplicity

The track selection criteria should have minimal effect on the mean  $p_T$ , as the reconstruction efficiency as a function of  $p_T$  should account for this. It was found in [63] to have at most a 0.3% effect for tracks with  $p_T > 150$  MeV/c, thus this is applied to all the mean  $p_T$  measurements as a conservative estimate of the systematic uncertainty from the track selections.

The triggering efficiency is found to have a negligible systematic effect on the mean  $p_T$ , and there is no event-level correction applied making the event class normalisation uncertainty non-applicable; the event class for this measurement is simply all triggered inelastic events. Inelastic events not triggered will generally have low multiplicity, with an average  $p_T$  the same as the triggered low multiplicity events. This is corroborated by the mean  $p_T$  analysis at  $\sqrt{s} = 0.9$  TeV by ALICE [63]. This study also shows a negligible systematic uncertainty from background events such as beam-gas interactions, generator bias and material budget. Pileup at high multiplicities is found to be negligible due to the averaging over multiple multiplicity bins, as pileup would likely shift an event into a higher multiplicity by no more than

a few bins.

The detector efficiency of the TPC and ITS combined are reported to give a systematic uncertainty of 0.6% [63].

The uncertainty in the particle composition was found to have give a 0.1% systematic uncertainty on the mean  $p_T$  measurement, as reported in [63].

The method of extracting a mean  $p_T$  measurement per multiplicity bin from the event-by-event estimates of the mean  $p_T$  is seen to have a 5% systematic uncertainty for low multiplicity bins, and up to 2% for the rest of the mean  $p_T$  versus charged multiplicity distribution.

### 3.7.3 Summary

The systematic uncertainties given in this section are conservative estimates from either studies performed in this analysis or quoted from published ALICE reports where appropriate, and are summarised in Table 3.5.

For the multiplicity measurement, it is found that the unfolding method gives the highest systematic uncertainty overall, with pileup giving the highest uncertainty for high multiplicity bins.

The largest systematic uncertainty in the mean  $p_T$  measurement is from the averaging method used to calculate the mean  $p_T$  using the event-level mean  $p_T$  measure-

### 3.7. SYSTEMATIC UNCERTAINTIES

*Table 3.5: Contributions to the systematic uncertainties for the two analyses. Numbers in brackets indicate high multiplicites, typically above  $6\times$  the average multiplicity.*

	$N_{CH}$ (High $N_{CH}$ )	Mean $p_T$ versus $N_{CH}$
Track selections	accounted for in unfolding	0.3%
Analysis method	5% (< 10%)	5 – 2%
Event class normalisation	5% (negligible)	negligible
Material budget	0.6%	0.6%
Pileup	< 5% (< 20%)	negligible
Background	negligible	negligible
Particle composition	1%	1%
Total	9% (22%)	5% – 2%

ments.

These systematic uncertainties are combined in quadrature for each distribution. The systematics for multiplicity are applied to the measured distribution before unfolding with the exception of the event level correction, as this is estimated from simulated data as a function of the true multiplicity.

---

---

# CHAPTER 4

---

## RESULTS

This chapter presents the results of the work outlined in this thesis. It contains four sections; the charged particle multiplicity, the approximation to the pseudorapidity density, KNO scaling of the multiplicity distributions and the mean  $p_T$  as a function of charged multiplicity. Comparisons are made with previous results where possible, and with the Phojet and Pythia event generators. The Pythia tune used was Perugia-0 [\[25\]](#).

## 4.1 Charged Particle Multiplicity

The multiplicity distributions, created using the iterative unfolding method in section 3.5, all required no more than 10 iterations to converge to a satisfactory result. An example of the details of one the unfolding results, on ALICE data, is shown in Figure 4.1, displaying a smooth unfolded result. The result, when multiplied by the original response matrix to simulate it being measured by the detector, gives a good agreement with the measured distribution; this cross-check shows that the unfolded result would be detected as the observed distribution if it were the true multiplicity distribution.

The multiplicity distributions for proton-proton collisions at  $\sqrt{s}$  of 900 GeV, 2760 GeV and 7000 GeV are shown in Figures 4.2, 4.3, 4.4 and 4.5 for two pseudorapidity intervals and two event classes. They show good agreement with other comparable experimental results, and excellent agreement with the ALICE published results for the overlapping range. These distributions significantly extend the multiplicity distributions measured by the ALICE experiment, and go farther in multiplicity than the high luminosity CMS experiment.

Detailed comparisons between the unfolded multiplicity distributions and results from other experiments and simulators are given for the three studied energies in Figures 4.6, 4.7, 4.8 and 4.9. The NSD multiplicity distribution at 900 GeV in  $|\eta| < 0.5$  shows excellent agreement over the whole range with previous results from UA5, CMS and ALICE published data. The UA5 distribution has two data points

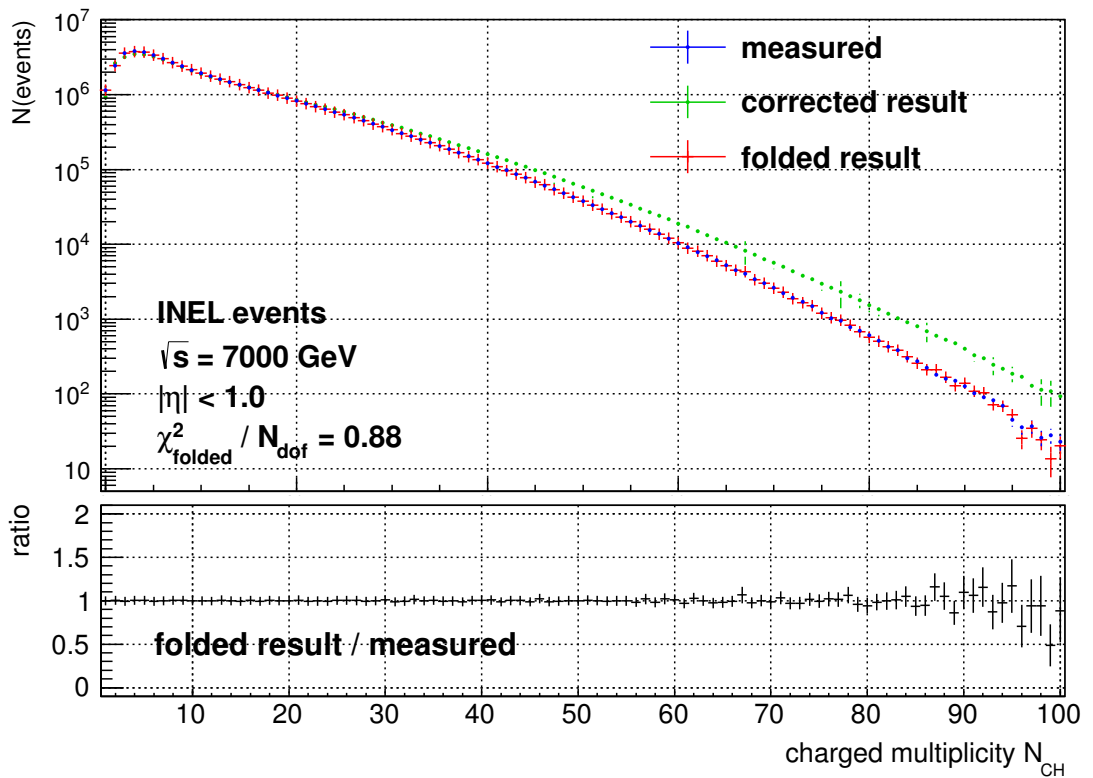


Figure 4.1: The multiplicity distributions (top panel) of the measured events (blue points), the unfolded distribution (green points) and the folded result of the unfolding (red points). The ratio of the folded result and the measured multiplicity is shown in the bottom panel. The unfolding took 6 iterations to achieve a  $\chi^2$  per degree of freedom of 0.88 between the measured distribution and the folded result.

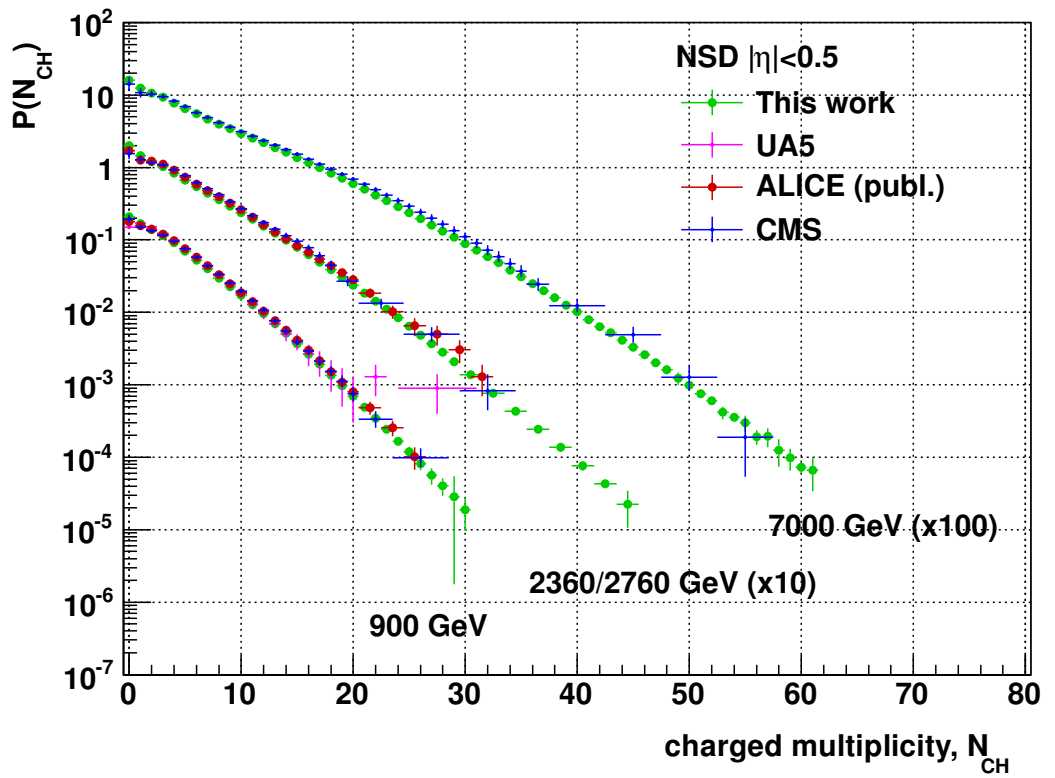


Figure 4.2: Multiplicity distributions of NSD events in the pseudorapidity interval  $|\eta| < 0.5$ , compared with data from UA5 [50], CMS [54] and previously published ALICE [53] results.

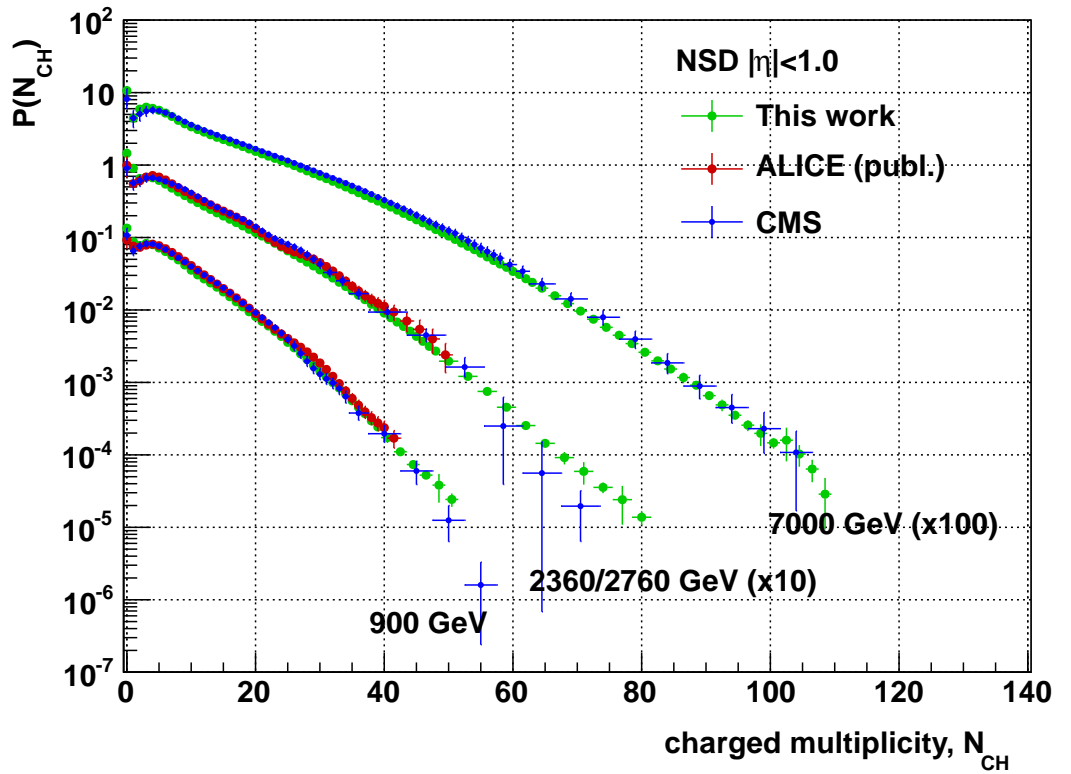


Figure 4.3: Multiplicity distributions of NSD events in the pseudorapidity interval  $|\eta| < 1.0$ , compared with data from CMS [54] and previously published ALICE [53] results. For the middle energy, this work has  $\sqrt{s} = 2760$  GeV, the other results have  $\sqrt{s} = 2360$  GeV.

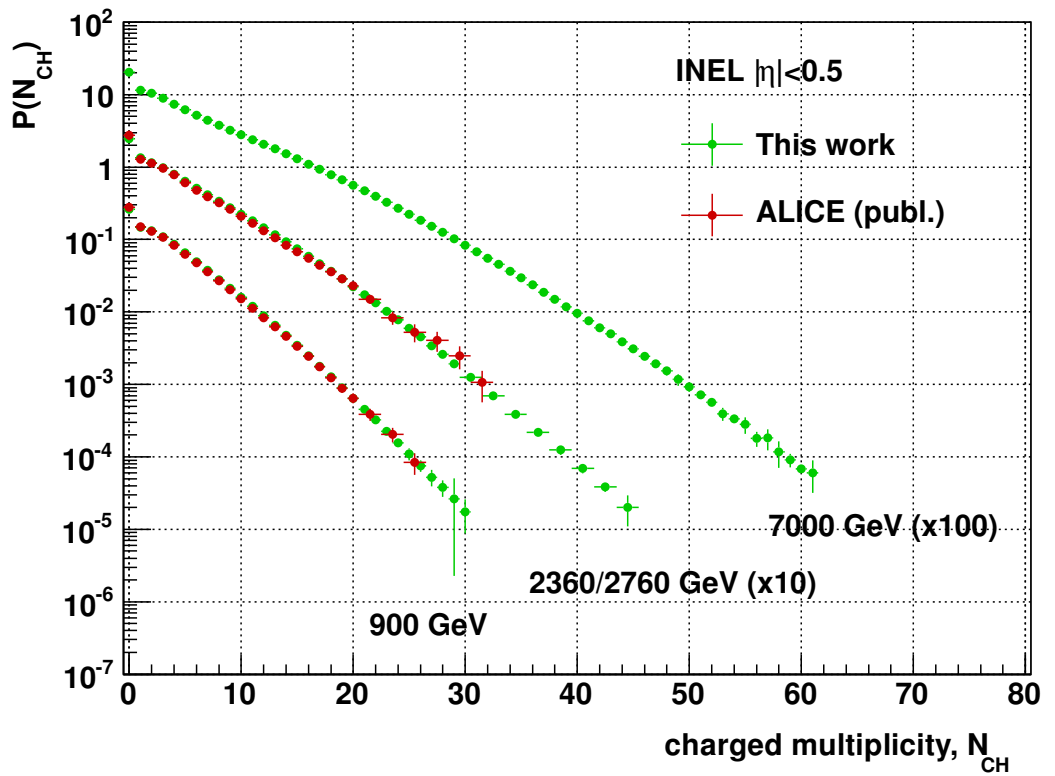


Figure 4.4: Multiplicity distributions of inelastic events in the pseudorapidity interval  $|\eta| < 0.5$ , compared with data from previously published ALICE [53] results. For the middle energy, this work has  $\sqrt{s} = 2760$  GeV, the ALICE published results have  $\sqrt{s} = 2360$  GeV.

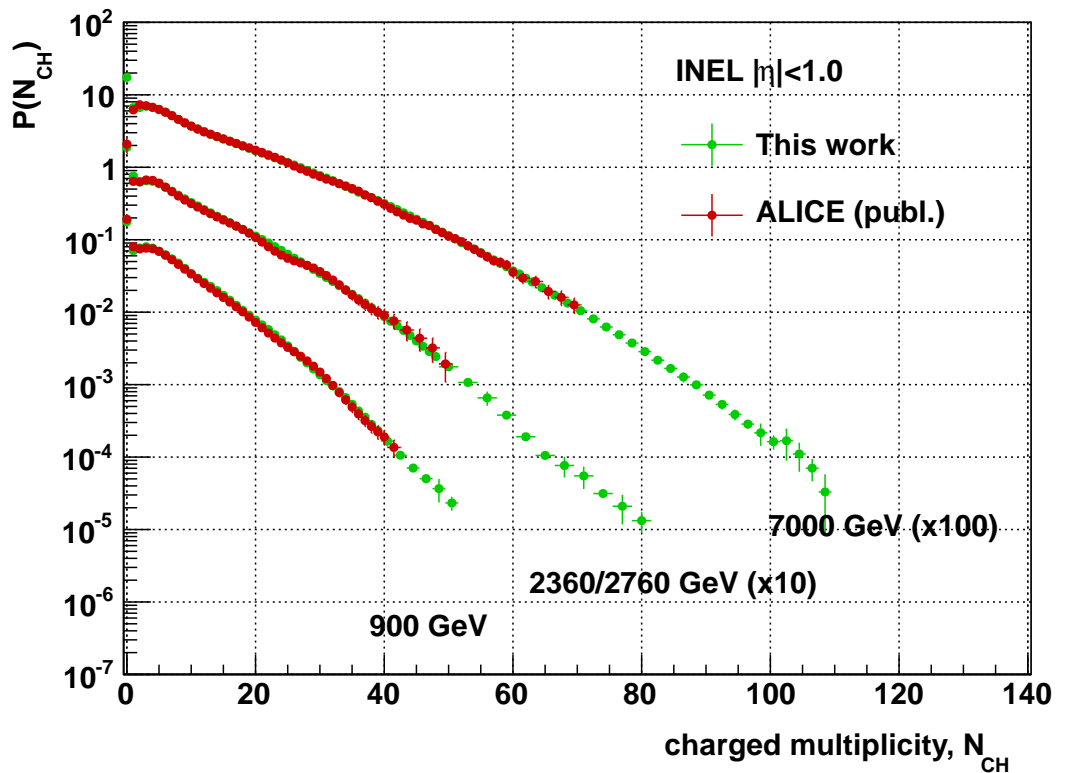


Figure 4.5: Multiplicity distributions of inelastic events in the pseudorapidity interval  $|\eta| < 1.0$ , compared with data from previously published ALICE [23] results. For the middle energy, this work uses  $\sqrt{s} = 2760$  GeV, the ALICE published results use  $\sqrt{s} = 2360$  GeV. The  $\sqrt{s} = 7000$  GeV distribution is normalised to the INEL  $> 0$  event class by ignoring zero bin.

in the tail with relatively large errors that do not follow the usual trend, and the rest matches with the other distributions. The Phojet distribution lies in excellent agreement with the new and past data, whereas the Pythia shows some skewing with regard to the data, indicating a different mean multiplicity.

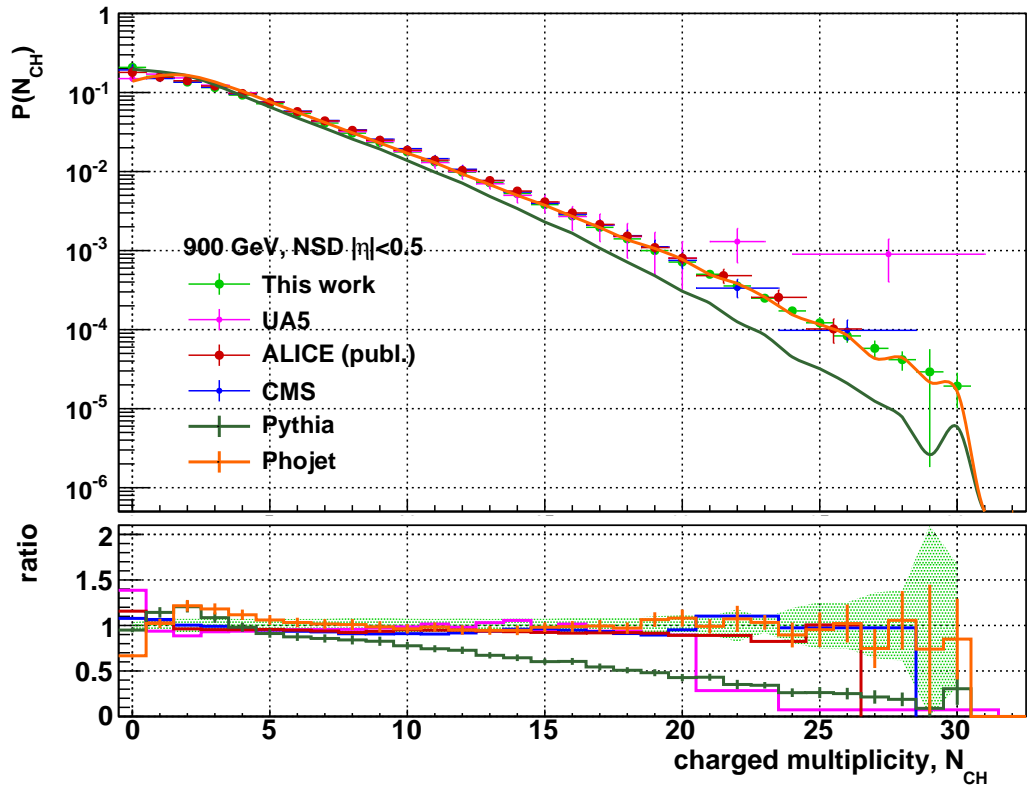


Figure 4.6: Multiplicity distribution of NSD events at  $\sqrt{s} = 900$  GeV/c in the pseudorapidity interval  $|\eta| < 0.5$ , compared to data from UA5 [50], CMS [54], previously published ALICE results [53] and the Pythia and Phojet generators.

The 2760 GeV multiplicity distribution in  $|\eta| < 1.0$  of NSD events shown in Figure 4.7 is reproduced less well by both generators. The Phojet distribution shows some departure throughout the whole range, especially at low multiplicity, while the overall trend is somewhat similar. The choppy structure of the ratio between the generated and measured distributions above the multiplicity of 50 is due to the

grouped binning of the measured distribution.

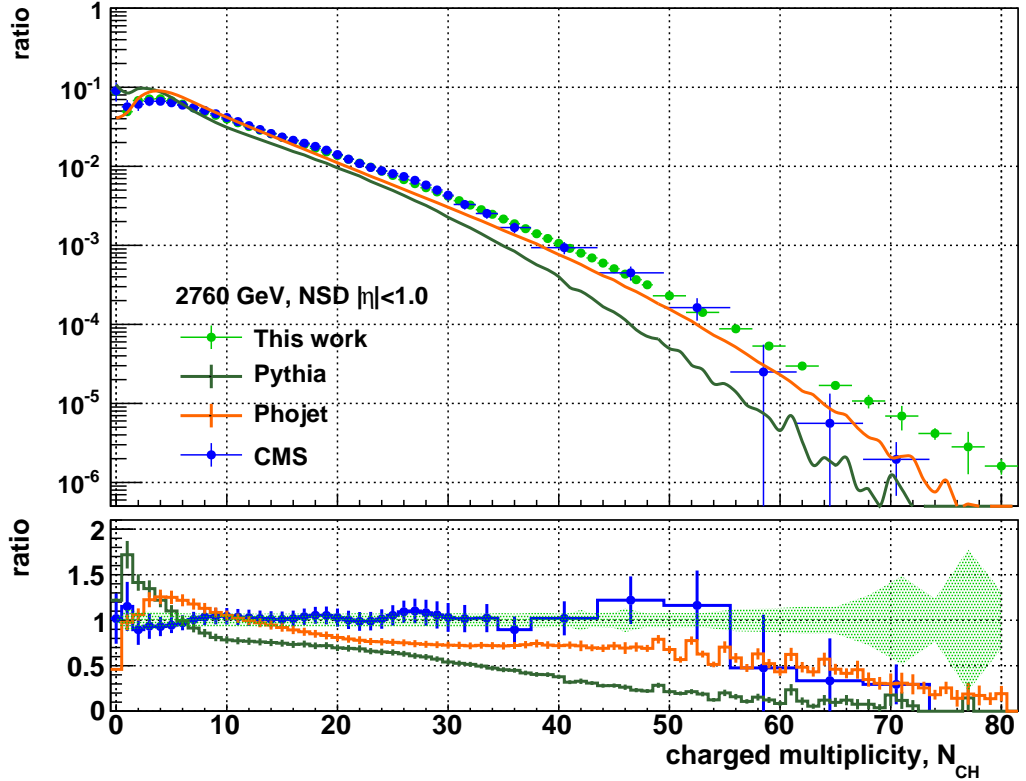


Figure 4.7: Multiplicity distribution of NSD events at  $\sqrt{s} = 2760$  GeV in the pseudorapidity interval  $|\eta| < 1.0$ , compared to data from CMS [54] and to the Pythia and Phojet distributions.

The 7000 GeV multiplicity distribution of inelastic events shown in Figure 4.8 with at least one particle detected in the larger pseudorapidity interval of  $|\eta| < 1.0$  shows an excellent agreement with the published ALICE data. The zero multiplicity bin is ignored in this comparison, as it is not included from the normalisation by the published data, and by definition of the INEL > 0 trigger should be empty. The two simulators do not reproduce the data here, underestimating the average multiplicity and falling short in the tail of the overall distribution.

The same underestimation of the generators is seen in Figure 4.9 for NSD collisions

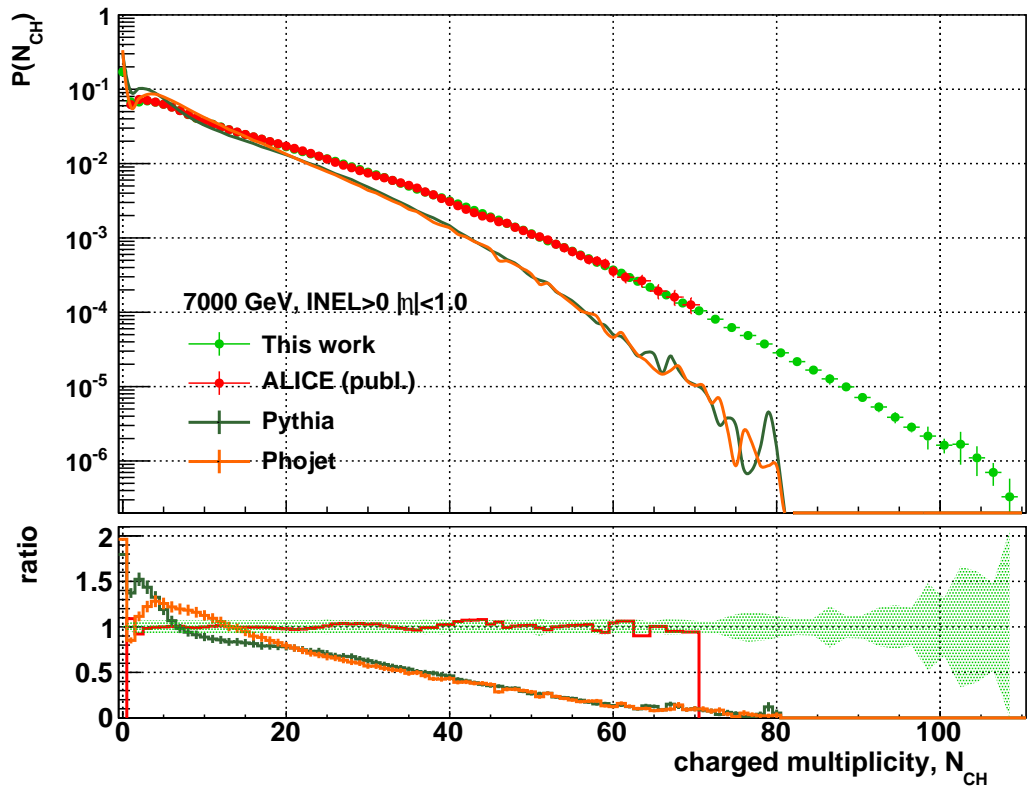


Figure 4.8: Multiplicity distribution of inelastic events at  $\sqrt{s} = 7000$  GeV with at least 1 charged particle found in the pseudorapidity interval  $|\eta| < 1.0$ , compared to published ALICE results [23] and to the Pythia and Phojet distributions.

at  $\sqrt{s} = 7000$  GeV. The overall comparison with CMS shows good agreement with the measured multiplicity of this work.

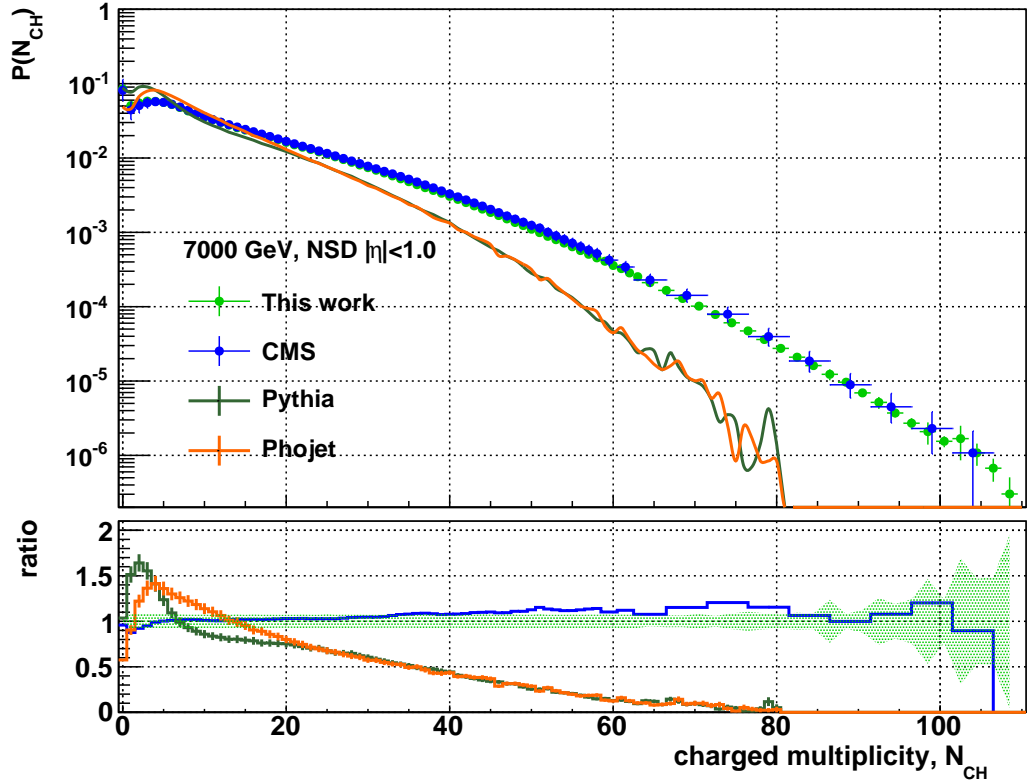


Figure 4.9: Multiplicity distribution of NSD events at  $\sqrt{s} = 7000$  GeV in the pseudorapidity interval  $|\eta| < 1.0$ , compared to data from CMS [54] and to the Pythia and Phojet distributions.

The multiplicity distributions taken with a minimum  $p_T$  threshold of 150 MeV/c and 500 MeV/c are shown in Figures 4.10 and 4.11, for a pseudorapidity interval of  $|\eta| < 0.5$  and  $|\eta| < 1.0$  respectively.

In both the pseudorapidity intervals, it is clear that the generators describe the data less well with increasing energy. Pythia gives a broader multiplicity distribution than Phojet, and is closer to the measured data. The distributions with larger minimum  $p_T$  threshold have a better agreement with data than the lower threshold, suggesting

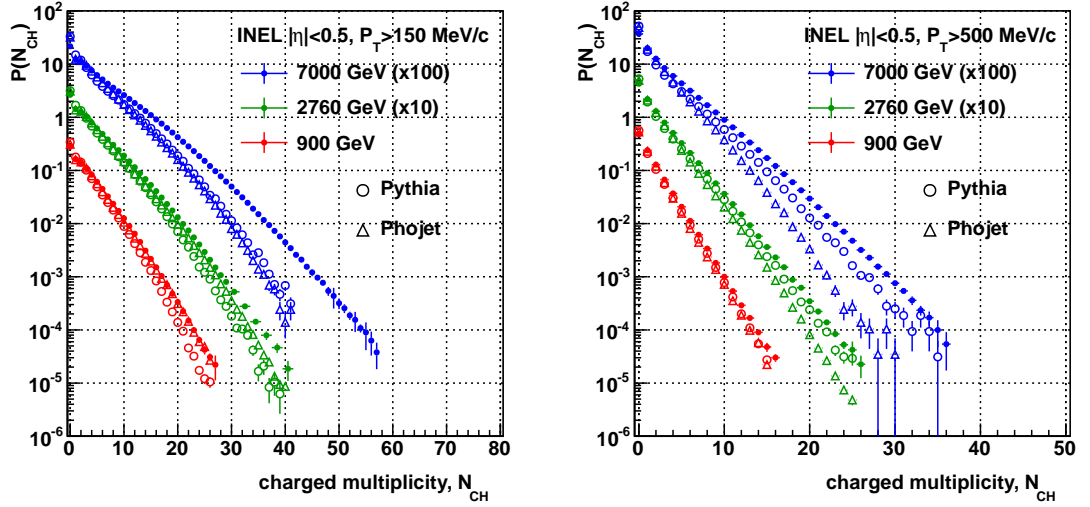


Figure 4.10: Multiplicity distributions of inelastic events for tracks with  $p_T$  more than 150 MeV/c (left) and 500 MeV/c (right) for three collision energies in the pseudorapidity interval  $|\eta| < 0.5$ . Filled data points are measurements from this work, open data points are distributions from Pythia and Phojet.

a disparity at lower  $p_T$  between the models and the data.

## 4.2 Pseudorapidity Density Approximation

Using the multiplicity distributions taken in the pseudorapidity interval of  $|\eta| < 0.5$ , an approximation to the charged particle density with respect to pseudorapidity can be estimated using the mean of that multiplicity distribution. This is carried out for all three energies, for NSD and inelastic events, and INEL  $> 0$  events in which there is always a particle found within the measured pseudorapidity interval. The results of these estimates are shown in Table 4.1 with errors. They are compared with other proton-proton measurements taken in a similar pseudorapidity interval. In the case of the middle energy of 2760 GeV which was used in this work, it is

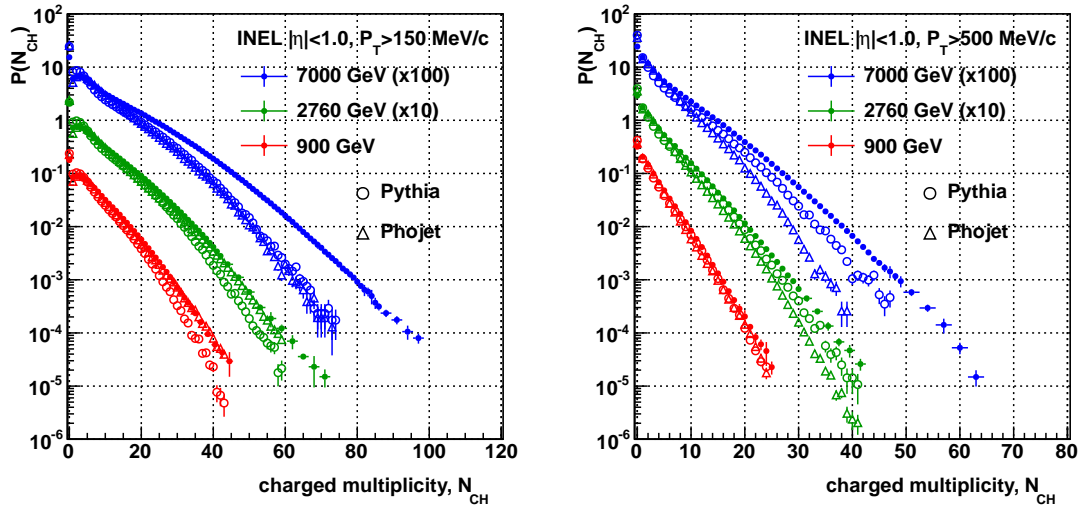


Figure 4.11: Multiplicity distributions of inelastic events for tracks with  $p_T$  more than 150 MeV/c (left) and 500 MeV/c (right) for three collision energies in the pseudorapidity interval  $|\eta| < 1.0$ . Filled data points are measurements from this work, open data points are distributions from Pythia and Phojet.

compared to results from other experiments taken at the lower collision energy of 2360 GeV.

Overall, the estimates of the charged particle density agree with measurements by other experiments, within the uncertainties. This result provides confidence in the success of the multiplicity analysis, as this comparison, to an observable derived from a distribution, implies the correction procedure worked well on the multiplicity distributions.

These charged particle densities also supplement the ALICE results for densities of NSD and inelastic events at  $\sqrt{s} = 7000$  GeV.

## 4.2. PSEUDORAPIDITY DENSITY APPROXIMATION

---

*Table 4.1: The pseudorapidity density of charged particles within  $|\eta| < 0.5$  estimated by the mean of the multiplicity distributions, compared results from UA5 [55], CMS [54] and published ALICE results [23, 53]. Errors on the values from this work are the combined statistical and systematic uncertainties.*

	Event class	900 GeV	2360/2760 GeV	7000 GeV
This work	NSD	$3.67 \pm 0.08$	$4.51 \pm 0.06$	$5.91 \pm 0.08$
	INEL	$3.14 \pm 0.05$	$3.90 \pm 0.05$	$5.23 \pm 0.07$
	INEL > 0	$3.83 \pm 0.06$	$4.70 \pm 0.07$	$6.10 \pm 0.08$
ALICE	NSD	$3.58 \pm 0.01^{+0.12}_{-0.12}$	$4.43 \pm 0.01^{+0.17}_{-0.12}$	
	INEL	$3.02 \pm 0.01^{+0.08}_{-0.05}$	$3.77 \pm 0.01^{+0.25}_{-0.12}$	
	INEL > 0	$3.81 \pm 0.01^{+0.07}_{-0.07}$	$4.70 \pm 0.01^{+0.11}_{-0.08}$	$6.01 \pm 0.01^{+0.20}_{-0.12}$
UA5	NSD	$3.43 \pm 0.05$		
	INEL	$3.09 \pm 0.05$		
CMS	NSD	$3.48 \pm 0.02 \pm 0.13$	$4.47 \pm 0.01 \pm 0.16$	$5.78 \pm 0.01 \pm 0.02$

### 4.3 KNO scaling

The NSD multiplicity distributions for the two pseudorapidity intervals presented are plotted in KNO variables in Figure 4.12.

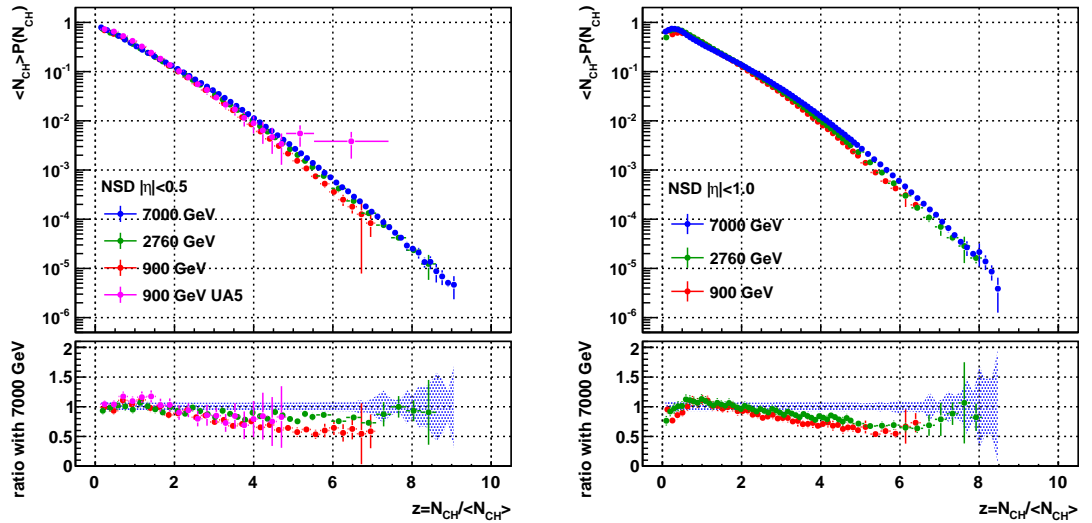


Figure 4.12: Multiplicity distributions of NSD events plotted in KNO variables, for  $|\eta| < 0.5$  (left) and  $|\eta| < 1.0$  (right). The  $\sqrt{s} = 7000$  GeV is compared to lower energy distributions as ratios, including data from UA5 [50].

It can be seen, by eye, that the distributions of  $z = \frac{N_{CH}}{\langle N_{CH} \rangle}$  for  $|\eta| < 0.5$  and  $|\eta| < 1.0$  lie on similar trajectories. Taking the ratio of each distribution to that of the  $\sqrt{s} = 7000$  GeV distribution shows a difference between the 900 GeV and 7000 GeV data that is more prominent in the larger pseudorapidity range, the smaller pseudorapidity range seems to show a difference but the uncertainty of the distribution makes this difficult to conclude for sure. There is little difference seen between the 2360 GeV and 7000 GeV distributions.

The  $C_q$  moments from equation 1.22 are calculated for the multiplicity distributions

to test the validity of KNO scaling. The moments must be collision energy invariant for KNO scaling to hold, and the calculated values for  $C_2$  to  $C_5$  are shown in Figure 4.13 with their associated uncertainties.

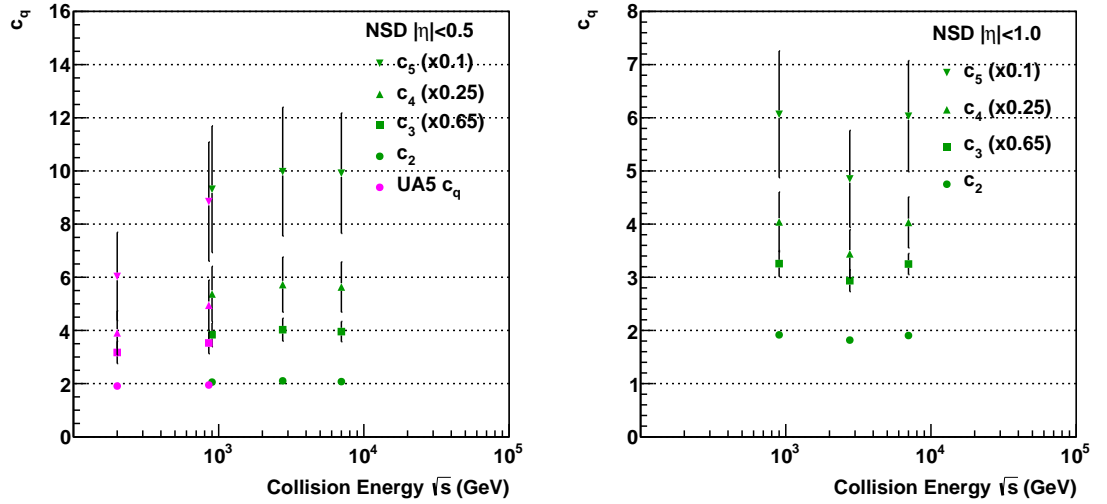


Figure 4.13: The moments  $C_2$  to  $C_5$  for the NSD multiplicity distributions as a function of collision energy for  $|\eta| < 0.5$  (left) and  $|\eta| < 1.0$  (right), including moments calculated from the UA5 data [50].

By eye, the moments from this work for  $|\eta| < 0.5$  do not change with energy within errors, but there is some disagreement with the UA5 data, especially the 200 GeV moments, which are lower. Table 4.2 shows that all the  $C_2$  moments agree, but the higher moments, constant for this work, do not agree with the UA5 data.

For  $|\eta| < 1.0$ , the moments for 900 and 7000 GeV are constant with respect to collision energy, within errors, but the middle energy moments are consistently lower, implying a violation of KNO scaling.

Within the data of this work, the  $C_q$  moments for  $|\eta| < 0.5$  are constant and demonstrate KNO scaling, but these moments disagree with previous results. The moments

Table 4.2:  $C_q$  moments of NSD multiplicity distributions for  $|\eta| < 0.5$ , including data from UA5 [50]

$ \eta  < 0.5$	UA5		This work		
	200	900	900	2760	7000
$C_2$	$1.91 \pm 0.09$	$1.95 \pm 0.07$	$2.06 \pm 0.08$	$2.10 \pm 0.07$	$2.07 \pm 0.06$
$C_3$	$4.87 \pm 0.64$	$5.43 \pm 0.62$	$5.91 \pm 0.69$	$6.20 \pm 0.66$	$6.09 \pm 0.59$
$C_4$	$15.6 \pm 3.3$	$19.8 \pm 3.79$	$21.5 \pm 4.16$	$22.9 \pm 4.16$	$22.59 \pm 3.79$
$C_5$	$60.3 \pm 16.6$	$88.5 \pm 22.4$	$93.1 \pm 23.8$	$99.7 \pm 24.2$	$99.2 \pm 22.7$

Table 4.3:  $C_q$  moments of NSD multiplicity distributions for  $|\eta| < 1.0$ .

$ \eta  < 1.0$	This work		
	900	2760	7000
$C_2$	$1.92 \pm 0.04$	$1.82 \pm 0.03$	$1.90 \pm 0.03$
$C_3$	$5.01 \pm 0.38$	$4.5 \pm 0.32$	$5.00 \pm 0.31$
$C_4$	$16.2 \pm 2.3$	$13.8 \pm 1.8$	$16.1 \pm 1.9$
$C_5$	$61 \pm 12$	$48.5 \pm 9.1$	$60 \pm 11$

for  $|\eta| < 1.0$  cannot be said to be independent of energy, due to the 2760 GeV results, so this implies a violation of KNO scaling. Measurements of multiplicity made in increasing intervals of pseudorapidity would shed more light on how KNO scaling might be violated in terms of phase space.

## 4.4 Mean $p_T$ as a function of Charged Multiplicity

Measurements of the mean  $p_T$ , per event, as a function of charged multiplicity are made for inelastic collisions with tracks in  $|\eta| < 0.8$ , to compare with the published ALICE results for 900 GeV. The mean  $p_T$  of each multiplicity bin is shown for the three collision energies studied in Figure 4.14, for tracks with  $p_T > 150$  MeV/c and  $p_T > 500$  MeV/c. For tracks with  $p_T$  larger than 500 MeV/c, the increasing mean  $p_T$  at low multiplicities slows its increase at roughly  $N_{CH} \sim 10$ , where the slope of the distribution changes to a softer gradient for all three collision energies. The same trend is seen for tracks with  $p_T$  larger than 150 MeV/c, but there is an initial decrease at low multiplicity, this is an artifact of the averaging calculation used to produce the distribution, and is accounted for in the systematic uncertainty.

For the same multiplicity bins, the higher energy collisions are shown to have a higher mean  $p_T$  per event. This effect could be a scaling along the multiplicity of the distribution according to the mean multiplicity at that collision energy, or the effect of more ‘hard’ interactions during the collision per event with increasing

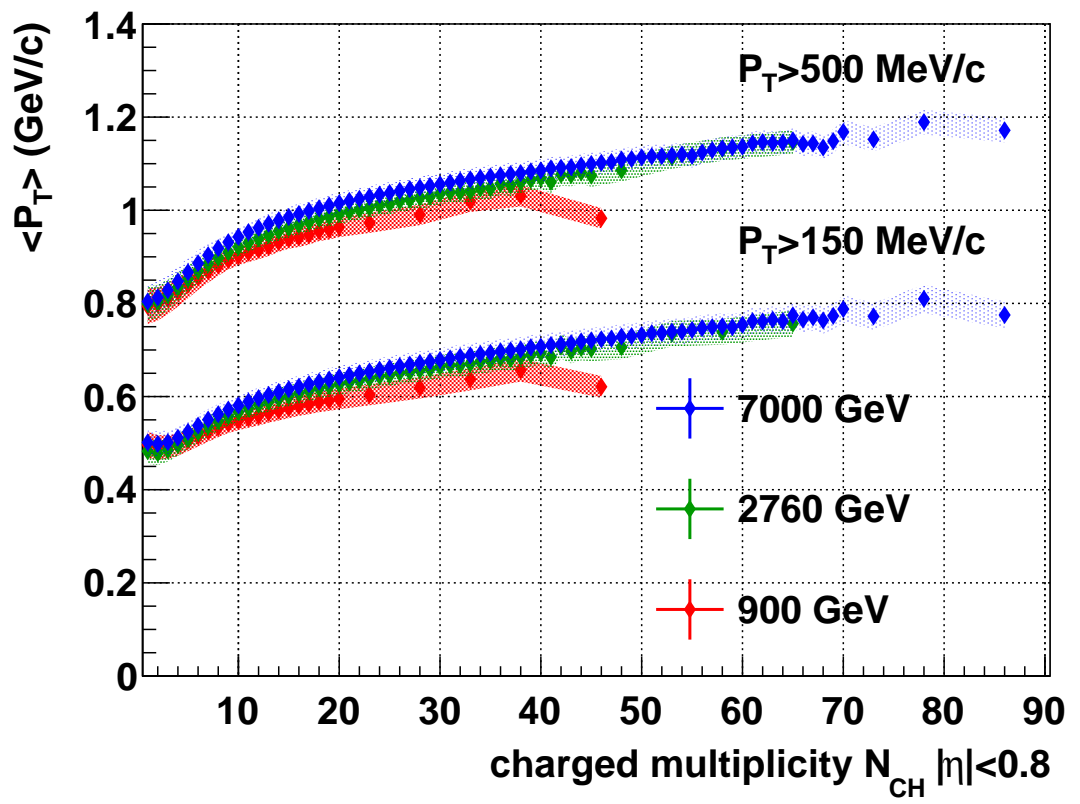


Figure 4.14: Average transverse momentum as a function of multiplicity in  $|\eta| < 0.8$  for inelastic events.

collision energy.

The change in slope of the distribution can be likened to the first part of a ‘rise-plateau-rise’ behaviour of a ledge structure, although the plateau is not a true constant in multiplicity, but has a smaller gradient than at low multiplicities. Evidence of a second rise, or increase in gradient, is not seen at the highest multiplicity bins measured in this work. Within the distribution uncertainties, the gradient after the initial rise remains the same throughout the rest of the distribution.

The distribution at  $\sqrt{s} = 900$  GeV is compared to the ALICE published results in Figure 4.15, as well as the two MC generators Pythia and Phojet. The measured distribution from this work matches very well to the ALICE published data. This agreement justifies the decision to use the multiplicity measurement of the event using the ITSTPC counting method as an estimate of the true multiplicity without correction, as this multiplicity estimator is seen in MC generated data to follow the true multiplicity very closely, as shown in Figure 3.13. The ALICE data points are binned to a corrected multiplicity using a response matrix.

For the mean  $p_T$  distribution with tracks of  $p_T > 150$  MeV/c neither Pythia nor Phojet exactly reproduce the data. Pythia shows a closer relation to the measurement than Phojet which has up to a 10% difference from the measurement, while Pythia stays within 5%. In the case of tracks with  $p_T > 500$  MeV/c, the Pythia generator reproduces the measured distribution very well, and Phojet underestimates again to the order of 10%.

#### 4.4. MEAN $P_T$ AS A FUNCTION OF CHARGED MULTIPLICITY

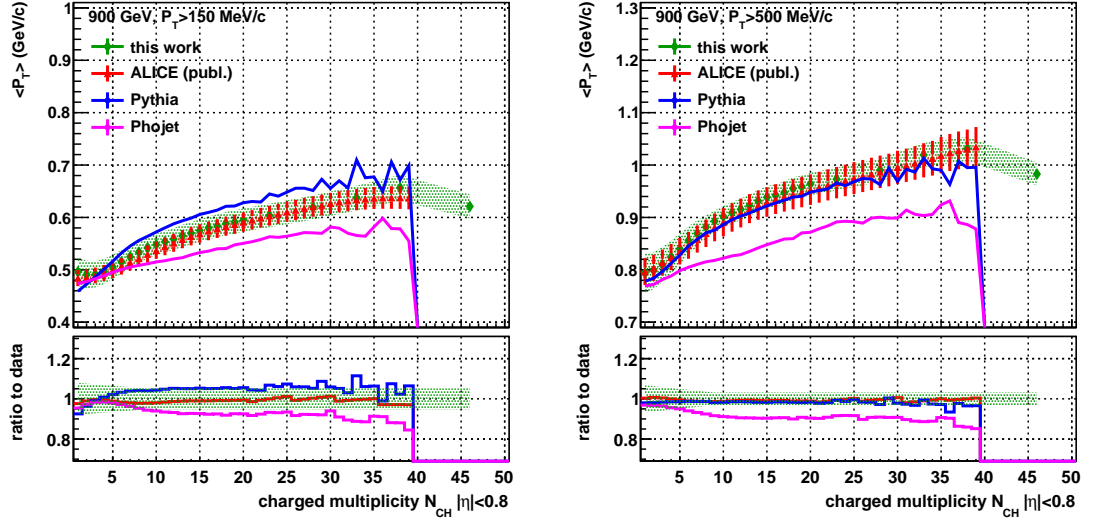


Figure 4.15: Average transverse momentum as a function of multiplicity for inelastic events at  $\sqrt{s} = 900$  GeV/c in  $|\eta| < 0.8$  for tracks with  $p_T > 150$  MeV/c (left) and  $p_T > 500$  MeV/c (right). This result is compared to published ALICE results [63], and to Pythia and Phojet distributions.

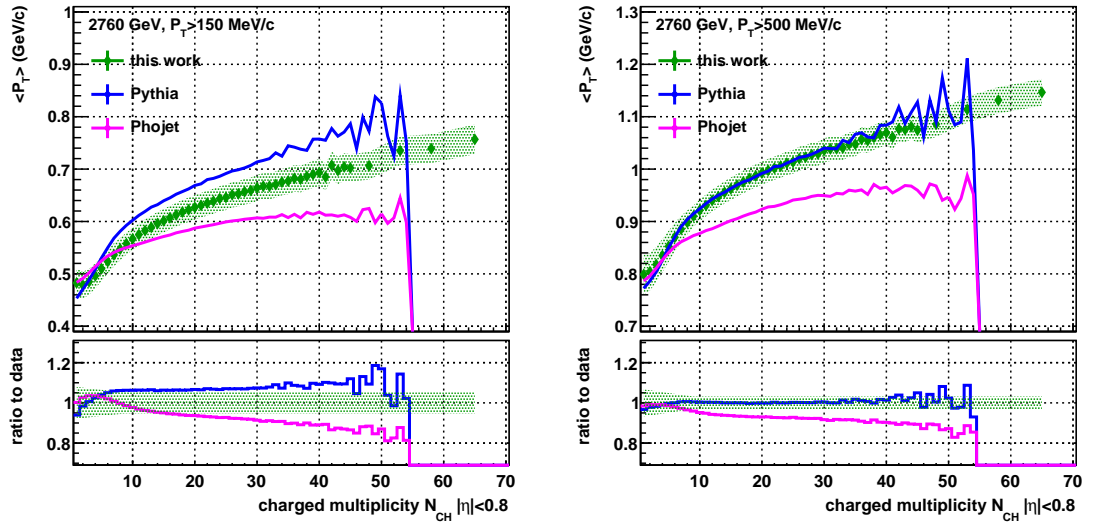


Figure 4.16: Average transverse momentum as a function of multiplicity for inelastic events at  $\sqrt{s} = 2760$  GeV/c in  $|\eta| < 0.8$  for tracks with  $p_T > 150$  MeV/c (left) and  $p_T > 500$  MeV/c (right). This result is compared to Pythia and Phojet distributions.

#### 4.4. MEAN $P_T$ AS A FUNCTION OF CHARGED MULTIPLICITY

For the 2760 GeV data shown in Figure 4.16, the generators Pythia and Phojet over- and underestimate, respectively, by about 10% the measured data for tracks with  $p_T > 150$  MeV/c for the soft slope region after the rise, whereas the rise is well reproduced by both. The  $p_T > 500$  MeV/c mean  $p_T$  distribution is reproduced very well by the Pythia generator for the entire multiplicity range, whereas Phojet matches the initial rise but underestimates the softer slope above the rise.

The same level of reproduction by the generators as seen for the 2760 GeV distributions is evident in the 7000 GeV distributions shown in Figure 4.17, where the low multiplicity rise of mean  $p_T$  is well reproduced for both track samples by both generators which deviate from the measurement above the slope. Again, Pythia reproduces very well, to within a few percent, the mean  $p_T$  distribution for tracks with  $p_T > 500$  MeV/c.

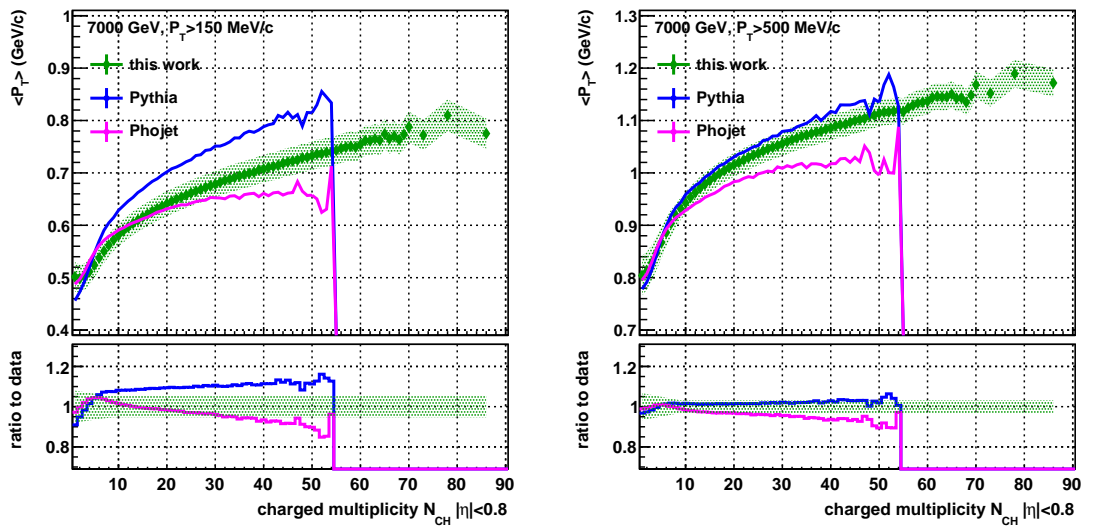


Figure 4.17: Average transverse momentum as a function of multiplicity for inelastic events at  $\sqrt{s} = 7000$  GeV/c in  $|\eta| < 0.8$  for tracks with  $p_T > 150$  MeV/c (left) and  $p_T > 500$  MeV/c (right). This result is compared to Pythia and Phojet distributions.

## 4.5 Summary

In this chapter, results are shown for the charged particle multiplicity of inelastic and NSD events, and the mean transverse momentum per event as a function of charged multiplicity for inelastic events.

The multiplicity distributions agree well with other experimental results, and extend the tail of the measured distribution further than ALICE or CMS have currently published. The Pythia and Phojet generators underestimate the multiplicity above  $\sqrt{s} = 900$  GeV. Evidence of KNO scaling is seen for the data in this work in  $|\eta| < 0.5$ , but the moments for the  $|\eta| < 1.0$  imply that KNO scaling does not hold in this pseudorapidity interval.

The mean transverse momentum correlation with multiplicity is extended past the ALICE published results, and agrees well with the previous data. The distribution has an initial rise followed by a gentler slope, and there is no indication of a second steep rise indicative of a ledge structure. The Pythia generator reproduces well the distribution for tracks with  $p_T$  above 500 MeV/c, and slightly overestimates it when the lower  $p_T$  tracks are included in the distribution. Phojet consistently underestimates the mean  $p_T$  distribution.

---

---

# CHAPTER 5

---

## CONCLUSION

This work presents the analysis of proton-proton collisions at  $\sqrt{s} = 900, 2760$  and  $7000$  GeV, and the measurement of the charged particle multiplicity in two pseudorapidity intervals of  $|\eta| < 0.5$  and  $|\eta| < 1.0$ . The mean transverse momentum, per event, as a function of charged multiplicity in  $|\eta| < 0.8$  (in order to compare to published ALICE results) for tracks with  $p_T$  above  $150$  MeV/c and  $500$  MeV/c has also been measured.

Two deconvolution methods were studied in order to correct the measured multiplicity distribution for detector effects; Single Value Decomposition (SVD) and an

---

iterative method based on Bayes' Theorem. The SVD method proved to be unsuccessful when a response matrix produced with a flat, non-physical multiplicity distribution is used to simulate the detector response. The iterative method proved successful in deconvolving the measured multiplicity distribution, and was used to correct the distributions presented in this work.

The effect of pileup for low interaction probability events was shown to contribute increasingly as a function of multiplicity, contributing up to 25% of measured events for the highest multiplicities above 10 times the average multiplicity, after detected pileup events are removed.

The corrected multiplicity distributions extend the published ALICE measurements by up to 60% for proton-proton collisions at  $\sqrt{s} = 7000$  GeV and  $\sqrt{s} = 2760$  GeV, and up to 25% at  $\sqrt{s} = 900$  GeV. The mean transverse momentum correlation with charged multiplicity is similarly extended in multiplicity with respect to the ALICE published results at  $\sqrt{s} = 900$  GeV.

The charged multiplicity results are compared to results from UA5, CMS and ALICE published results, and agree well. The Phojet MC generator reproduces the  $\sqrt{s} = 900$  GeV well, but both Pythia and Phojet fall too steeply in multiplicity, failing to reproduce the high multiplicity tail of the measurements.

The mean transverse momentum at  $\sqrt{s} = 900$  GeV agrees well with the published ALICE results. Pythia agrees well with the results for tracks above 500 MeV/c for all collision energies, and with the  $p_T > 150$  MeV/c result at 900 GeV, over-

---

estimating the distribution by about 10% at higher energies using this  $p_T$  threshold. This particular tune of Pythia, Perugia-0, allows the interaction between QCD strings during the simulation of the proton-proton collision that drives the correlation between mean transverse momentum and multiplicity. Phojet consistently underestimates the mean  $p_T$  distributions above the initial rise by 10 – 15%.

Using the  $C_q$  moments of the NSD multiplicity distributions, it is seen that KNO scaling seems to hold in the pseudorapidity interval  $|\eta| < 0.5$ , but the data in  $|\eta| < 1.0$  implies a violation of KNO scaling.

---

## REFERENCES

- [1] D. Griffiths, *Introduction to Elementary Particles* (Wiley-VCH, 2008).
- [2] D. H. Perkins, *Introduction to High Energy Physics (3rd Edition)* (Addison-Wesley, 1987).
- [3] P. W. Higgs, Phys. Rev. Lett. **13**, 508 (1964).
- [4] F. Englert and R. Brout, Phys. Rev. Lett. **13**, 321 (1964).
- [5] G. S. Guralnik, C. R. Hagen, and T. W. B. Kibble, Phys. Rev. Lett. **13**, 585 (1964).
- [6] ATLAS Collaboration, G. Aad *et al.*, Phys.Lett. **B716**, 1 (2012), 1207.7214.
- [7] CMS Collaboration, S. Chatrchyan *et al.*, Phys.Lett. **B716**, 30 (2012), 1207.7235.
- [8] M. Gellmann, Physics Letters **8**, 214 (1964).
- [9] G. Zweig, CERN-TH-401, 1964.
- [10] O. W. Greenberg, Phys. Rev. Lett. **13**, 598 (1964).
- [11] N. Cabibbo and G. Parisi, Phys.Lett. **B59**, 67 (1975).
- [12] F. Karsch, Lect.Notes Phys. **583**, 209 (2002), hep-lat/0106019.
- [13] U. W. Heinz, p. 165 (2004), hep-ph/0407360.
- [14] F. E. Close, *An Introduction to Quarks and Partons* (Academic Pr, 1979).
- [15] H1 Collaboration, ZEUS Collaboration, L. Lindemann, Nucl.Phys.Proc.Suppl. **64**, 179 (1998).

- 
- [16] STAR Collaboration, J. Adams *et al.*, Nucl.Phys. **A757**, 102 (2005), nucl-ex/0501009.
- [17] M. Abreu *et al.*, Physics Letters B **477**, 28 (2000).
- [18] J. Bjorken, FERMILAB-PUB-82-059-THY, FERMILAB-PUB-82-059-T (1982).
- [19] J. D. Bjorken, Phys. Rev. D **27**, 140 (1983).
- [20] J. Harris, eConf **C030614**, 030 (2003).
- [21] A. Toia, J.Phys. **G38**, 124007 (2011), 1107.1973.
- [22] ALICE Collaboration, K. Aamodt *et al.*, Phys. Rev. Lett. **105**, 252301 (2010).
- [23] ALICE Collaboration, K. Aamodt *et al.*, Eur.Phys.J. **C68**, 345 (2010), 1004.3514.
- [24] R. K. Ellis, W. J. Stirling, and B. R. Webber, *QCD and Collider Physics (Cambridge Monographs on Particle Physics, Nuclear Physics and Cosmology)* (Cambridge University Press, 1996).
- [25] P. Z. Skands, Phys.Rev. **D82**, 074018 (2010), 1005.3457.
- [26] ALICE Collaboration, B. Abelev *et al.*, Eur.Phys.J. C (2012), 1208.4968.
- [27] P. Collins, *An Introduction to Regge Theory & High Energy Physics*, Cambridge monographs on mathematical physics (University Press, 1977).
- [28] A. Kaidalov, (2001), hep-ph/0103011.
- [29] CDF Collaboration, D. Acosta *et al.*, Phys. Rev. Lett. **91**, 011802 (2003).
- [30] T. Sjostrand, S. Mrenna, and P. Z. Skands, JHEP **0605**, 026 (2006), hep-ph/0603175.
- [31] R. Engel and J. Ranft, Phys. Rev. D **54**, 4244 (1996).
- [32] I. Sarcevic, Acta Phys.Polon. **B19**, 361 (1988).
- [33] A. Kaidalov and M. Poghosyan, Eur.Phys.J. **C67**, 397 (2010), 0910.2050.
- [34] ATLAS Collaboration, G. Aad *et al.*, New J.Phys. **13**, 053033 (2011), 1012.5104.
- [35] R. P. Feynman, Phys. Rev. Lett. **23**, 1415 (1969).
- [36] J. F. Grosse-Oetringhaus, CERN-THESIS-2009-033 (2009).
- [37] Z. Koba, H. B. Nielsen, and P. Olesen, Nucl.Phys. **B40**, 317 (1972).

- 
- [38] M. G. Bowler and P. N. Burrows, *Zeitschrift fr Physik C Particles and Fields* **31**, 327 (1986).
- [39] J. F. Grosse-Oetringhaus and K. Reygers, *J.Phys.* **G37**, 083001 (2010), 0912.0023.
- [40] G. Alner *et al.*, *Physics Letters B* **160**, 193 (1985).
- [41] A. Giovannini and R. Ugoccioni, *Int.J.Mod.Phys.* **A20**, 3897 (2005), hep-ph/0405251.
- [42] A. Giovannini and L. Hove, *Zeitschrift fr Physik C Particles and Fields* **30**, 391 (1986).
- [43] A. Giovannini and R. Ugoccioni, *Nucl.Phys.Proc.Suppl.* **71**, 201 (1999), hep-ph/9710361.
- [44] CDF Collaboration, D. Acosta *et al.*, *Phys.Rev.* **D65**, 072005 (2002).
- [45] T. Alexopoulos *et al.*, *Physics Letters B* **435**, 453 (1998).
- [46] S. G. Matinyan and W. Walker, *Phys.Rev.* **D59**, 034022 (1999), hep-ph/9801219.
- [47] A. Giovannini and R. Ugoccioni, *Phys.Rev.* **D59**, 094020 (1999), hep-ph/9810446.
- [48] (Ames Bologna CERN Dortmund Heidelberg Warsaw Collaboration), A. Breakstone *et al.*, *Phys. Rev. D* **30**, 528 (1984).
- [49] UA5 Collaboration, G. Alner *et al.*, *Phys.Lett.* **B160**, 193 (1985).
- [50] UA5 Collaboration, R. Ansorge *et al.*, *Z.Phys.* **C43**, 357 (1989).
- [51] ALICE Collaboration, K. Aamodt *et al.*, *JINST* **3**, S08002 (2008).
- [52] CMS Collaboration, S. Chatrchyan *et al.*, *JINST* **3**, S08004 (2008).
- [53] ALICE Collaboration, K. Aamodt *et al.*, *Eur.Phys.J.* **C68**, 89 (2010), 1004.3034.
- [54] CMS Collaboration, V. Khachatryan *et al.*, *JHEP* **1101**, 079 (2011), 1011.5531.
- [55] UA5 Collaboration, G. Alner *et al.*, *Z.Phys.* **C33**, 1 (1986).
- [56] Aachen-CERN-Heidelberg-Munich Collaboration, W. Thome *et al.*, *Nucl.Phys.* **B129**, 365 (1977).
- [57] UA5 Collaboration, K. Alpgard *et al.*, *Phys.Lett.* **B112**, 183 (1982).

- 
- [58] PHOBOS Collaboration, R. Nouicer *et al.*, J.Phys. **G30**, S1133 (2004), nucl-ex/0403033.
- [59] STAR Collaboration, B. Abelev *et al.*, Phys.Rev. **C79**, 034909 (2009), 0808.2041.
- [60] UA5 Collaboration, G. Alner *et al.*, Phys.Rept. **154**, 247 (1987).
- [61] UA1 Collaboration, C. Albajar *et al.*, Nucl.Phys. **B335**, 261 (1990).
- [62] X.-n. Wang and R. C. Hwa, Phys.Rev. **D39**, 187 (1989).
- [63] ALICE Collaboration, K. Aamodt *et al.*, Phys.Lett. **B693**, 53 (2010), 1007.0719.
- [64] ALICE Collaboration, B. Abelev *et al.*, Eur.Phys.J. **C72**, 2124 (2012), 1205.3963.
- [65] CMS Collaboration, V. Khachatryan *et al.*, Phys.Rev.Lett. **105**, 022002 (2010), 1005.3299.
- [66] CMS Collaboration, V. Khachatryan *et al.*, JHEP **1002**, 041 (2010), 1002.0621.
- [67] A. Rossi *et al.*, Nucl.Phys. **B84**, 269 (1975).
- [68] T. Alexopoulos *et al.*, Phys.Rev.Lett. **60**, 1622 (1988).
- [69] CDF Collaboration, F. Abe *et al.*, Phys.Rev.Lett. **61**, 1819 (1988).
- [70] e. Evans, Lyndon and e. Bryant, Philip, JINST **3**, S08001 (2008).
- [71] ATLAS Collaboration, G. Aad *et al.*, JINST **3**, S08003 (2008).
- [72] LHCb Collaboration, J. Alves, A. Augusto *et al.*, JINST **3**, S08005 (2008).
- [73] TOTEM Collaboration, G. Anelli *et al.*, JINST **3**, S08007 (2008).
- [74] LHCf Collaboration, O. Adriani *et al.*, JINST **3**, S08006 (2008).
- [75] J. Pinfold *et al.*, CERN Report No. CERN-LHCC-2009-006. MoEDAL-TDR-001, 2009 (unpublished).
- [76] Project to prepare the PS Complex to be a Pre-injector for the LHC, URL: <http://ps-div.web.cern.ch/ps-div/LHC-PS/LHC-PS.html>, 1998.
- [77] ATLAS Collaboration, G. Aad *et al.*, Nature Commun. **2**, 463 (2011), 1104.0326.
- [78] ATLAS, J. Boyd and G. Unal, Luminositypublicresults, <https://twiki.cern.ch/twiki/bin/view/AtlasPublic/LuminosityPublicResults>, 2012.

- 
- [79] ALICE Collaboration, B. Abelev *et al.*, Phys.Rev.Lett. **105**, 252301 (2010), 1011.3916.
- [80] ALICE Collaboration, 3D ALICE Schematic - with Description — ALICE Figure Repository, <https://aliceinfo.cern.ch/Figure/>, 2013.
- [81] ALICE Collaboration, Technical Design Report of the Inner-Tracking System, CERN/LHCC 99-12, 1999.
- [82] ALICE Collaboration, E. Carminati, F *et al.*, J.Phys.G **G30**, 1517 (2004).
- [83] ALICE Collaboration, Technical Design Report of the Time Projection Chamber, CERN/LHCC 2000-001, 2000.
- [84] ALICE Collaboration, A. Alici, arXiv (2012), 1203.5976.
- [85] ALICE Collaboration, ALICE: Addendum to the technical design report of the Photon Multiplicity Detector (PMD), CERN-LHCC-2003-038, 2003.
- [86] M. Bombara, AliceTriggerIntroduction < ALICE < TWiki, <http://www.ep.ph.bham.ac.uk/twiki/bin/view/ALICE/AliceTriggerIntroduction>, 2008, online TWiki page.
- [87] UA5 Collaboration, G. Alner *et al.*, Z.Phys. **C32**, 153 (1986).
- [88] ALICE Collaboration, B. Abelev *et al.*, Eur.Phys.J. **C73**, 2456 (2013), 1208.4968.
- [89] R. J. Barlow, *Statistics: A Guide to the Use of Statistical Methods in the Physical Sciences (Manchester Physics Series)*, Reprint ed. (WileyBlackwell, 1989).
- [90] University of Birmingham, P. Petrov, The mu values in Monalisa, 2011, A presentation given in an ALICE internal meeting.
- [91] Università degli Studi di Torino - INFN Torino, G. M. Innocenti *et al.*, Pileup tagging Performance in high multiplicity events, 2010, A presentation given in an ALICE internal meeting.
- [92] A. Hocker and V. Kartvelishvili, Nucl.Instrum.Meth. **A372**, 469 (1996), hep-ph/9509307.
- [93] I. Antcheva *et al.*, Comput.Phys.Commun. **182**, 1384 (2011).
- [94] R. Barlow, Maximum Entropy and Related Methods, URL: [http://www-group.slac.stanford.edu/sluc/lectures/Stat\\_Lectures.html](http://www-group.slac.stanford.edu/sluc/lectures/Stat_Lectures.html), 2010.
- [95] G. Cowan, Conf.Proc. **C0203181**, 248 (2002).
- [96] G. D'Agostini, Nucl.Instrum.Meth. **A362**, 487 (1995).

- [97] T. Adye, arXiv (2011), 1105.1160.
- [98] WA97 Collaboration, F. Antinori *et al.*, Eur.Phys.J. **C14**, 633 (2000).
- [99] ALICE Collaboration, B. Abelev *et al.*, JHEP **1207**, 116 (2012), 1112.2082.